

# Scanning Tunneling Spectroscopy with Superconducting Junctions: From Single Channel Transport to Local Pair Breaking Potentials

THÈSE N° 8730 (2018)

PRÉSENTÉE LE 16 JUILLET 2018

À LA FACULTÉ DES SCIENCES DE BASE  
LABORATOIRE DE SCIENCE À L'ÉCHELLE NANOMÉTRIQUE  
PROGRAMME DOCTORAL EN PHYSIQUE

ÉCOLE POLYTECHNIQUE FÉDÉRALE DE LAUSANNE

POUR L'OBTENTION DU GRADE DE DOCTEUR ÈS SCIENCES

PAR

Jacob SENKPIEL

acceptée sur proposition du jury:

Prof. V. Savona, président du jury  
Prof. K. Kern, directeur de thèse  
Prof. E. Scheer, rapporteuse  
Prof. P. Liljeroth, rapporteur  
Prof. H. Brune, rapporteur



ÉCOLE POLYTECHNIQUE  
FÉDÉRALE DE LAUSANNE

Suisse  
2018



# Abstract

This thesis contains two major topics, the restriction of tunneling to only a few channels in the scanning tunneling microscope (STM) and the interaction of local magnetic impurities with superconductivity.

At a temperature of 15 mK, the quantum back-action of the electromagnetic environment in an STM junction becomes prominent. It influences the tunneling process, and by that inevitably also the spectroscopy of physical phenomena. We demonstrate that the macroscopic tip shape strongly defines this back-action. It can be reduced by increasing the tip wire diameter. This increases the capacitance of the junction, and thereby significantly enhances the spectroscopic energy resolution. Modeling this effect with  $P(E)$ -theory, we extrapolate that the electromagnetic environment of the junction influences measurements in the STM up to a temperature of about 1 K. This result helps establish a direct correspondence between the  $P(E)$ -model and the energy resolution function of the STM.

We further study the tunneling process by constructing a single channel junction made of an Al adatom on an Al(100) crystal and the single apex atom of an Al tip. We provide proof that the transport in this junction is strongly limited to a single channel by analyzing Andreev reflection spectra over a wide conductance range up to the quantum of conductance.

With this junction we show how the Josephson effect deviates from the many channel and low transmission model by Ambegaokar and Baratoff. We also present a new model, based on the full Andreev bound state relation for the few channel limit, which accounts for transmission dependencies and multiple Cooper pair tunneling processes. Modeling the Josephson effect in our junction this new model reproduces the experimental data in great detail. Regarding the determination of the Josephson coupling energy or critical current in STM-experiments, we expect at least 0.6 % and up to 2.6 % deviation from the linear model at a conductance of  $0.1 G_0$  and up to 17 % at  $0.5 G_0$ .

In the normal conducting state of this single channel junction the environmental back-action manifests as a transmission reduction around zero voltage, known as the dynamical Coulomb blockade (DCB). Here we test the predicted vanishing of the DCB for transmissions towards unity in a single channel system. Our data clearly support this expectation. These results suggest that the transport process becomes less sensitive to the environmental back-action with increasing channel transmission.

Concerning pair breaking potentials in a multi-band superconductor, we study Fe-doped  $\text{NbSe}_2$  with a V-tip. We demonstrate that Yu-Shiba-Rusinov (YSR) resonances emerge not only

---

in the energy-gap but also outside of it, at the position of coherence peaks, where they are significantly broadened. We demonstrate a direct correspondence of the YSR-state lifetime to the imaginary part of the superconducting order parameter ( $\Delta$ ). To demonstrate this correspondence we compare the experimental peak-width to peak-energy-position dependence with a T-matrix scattering model, taking into account the two-band superconductivity of NbSe<sub>2</sub>, with inter-band coupling and magnetic background scattering. Our results show that YSR-resonances can be used to probe the imaginary part of the superconducting order parameter. We suspect that many asymmetries observed in spectra of the superconducting gap are related to this effect. We collate some early results of the local Josephson critical current and the inferred amplitude of the superconducting order parameter in NbSe<sub>2</sub>. We find local variations around the embedded Fe impurities suggesting that the order parameter is reduced by about 20 %.

Key words:

Josephson scanning tunneling microscopy (JSTM)

Multi-band superconductivity

Pair-breaking potentials

Superconducting order parameter

Yu-Shiba-Rusinov states (YSR)

Andreev reflections

Single channel transmission

Quantum back-action

Dynamical Coulomb blockade (DCB)

# Zusammenfassung

Die vorliegende Arbeit behandelt zwei Hauptthemen, die Abhängigkeit des Tunnelprozess im Rastertunnelmikroskop (RTM) von den Transportkanälen und die Wechselwirkung lokaler magnetischer Störer mit Supraleitern.

Bei einer Temperatur von 15 mK erlangt die Quanten-Rückwirkung der elektromagnetischen Umgebung des Tunnelkontaktes eine erhebliche Bedeutung. Sie beeinflusst den Tunnelprozess und damit unumgänglich auch spektroskopische Messungen physikalischer Phänomene. Wir zeigen, dass insbesondere die makroskopischen Abmessungen der RTM-Spitze diese Rückwirkung bestimmen. Sie kann verringert werden, indem der Durchmesser der Spitze erhöht wird. Dies erhöht die Kapazität zwischen Spitze und Probe, was wiederum eine signifikante Verbesserung der Energieauflösung zur Folge hat. Dieser Effekt kann mit der sogenannten  $P(E)$ -Theorie beschrieben werden. Wir erwarten, dass er bis zu einer Temperatur von etwa 1 K Messungen beeinflusst. Diese Ergebnisse etablieren das  $P(E)$ -Modell weiter für Rastertunnelmikroskopie.

Des Weiteren untersuchen wir die Besonderheiten von Einkanal-tunneln zwischen zwei einzelnen Al Atomen. Anhand von Andreev-Reflektions Spekten über einen sehr großen Widerstandsbereich bis zum Quantum der Leitfähigkeit beweisen wir, dass in sehr guter Näherung nur ein einzelner Kanal für den Transport verantwortlich ist. Mit diesem Einkanalübergang studieren wir die Transmissionsabhängigkeit des Josephson Effekts und wie sie von dem Modell von Ambegaokar und Baratoff (AB) für viele Kanäle abweicht. Wir benutzen ein neues Modell, das auf der vollständigen Relation für gebundene Andreev-Zustände beruht. Es ist transmissionsabhängig und berücksichtigt simultanes Tunneln von mehreren Cooper Paaren. Wir finden eine hervorragende Übereinstimmung zwischen unseren Daten und den Ergebnissen des Modells. Im Bezug auf die Ermittlung der Josephson Kopplung mit dem RTM zeigt unsere Studie, dass mindestens 0.6 % und bis zu 2.6 % Abweichung von dem AB-Modell, bei einer Leitfähigkeit von  $0.1 G_0$  zu erwarten sind, bei  $0.5 G_0$  sogar bis zu 17 %.

Im normalleitenden Zustand des Tunnelübergangs wird die Rückwirkung der Umgebung direkt in Form der dynamischen Coulomb Blockade (DCB) sichtbar. Es wird erwartet, dass sie bei steigender Transmission  $\tau$  kleiner wird und bei  $\tau = 1$  verschwindet. Unsere experimentellen Daten sind in Übereinstimmung mit dieser Erwartung. Dieses Ergebnis suggeriert, dass der Transport mit steigender Transmission weniger empfänglich für die Rückwirkung der Umgebung wird.

Im Bezug auf paarbrechende Potentiale in Supraleitern haben wir Fe dotiertes NbSe<sub>2</sub> untersucht. Wir haben demonstriert, dass Yu-Shiba-Rusinov (YSR) Resonanzen nicht nur in

---

der Bandlücke von Supraleitern existieren können, sondern auch außerhalb. Wir finden sie auch in dem Energiebereich der Kohärenzmaxima, wo sie eine erheblich größere Breite aufweisen. Wir können eine direkte Abhängigkeit zwischen der Lebensdauer der YSR-Zustände und dem imaginären Teil des supraleitenden Ordnungsparameters zeigen. Um diesen zu beweisen vergleichen wir den experimentellen Zusammenhang von Resonanzposition und Breite mit einem theoretischen Model auf Basis von T-Matrix Streuung. In diesem werden Inter-Bandkopplung und Streuung an einem magnetischen Hintergrund berücksichtigt. Unsere Ergebnisse zeigen, dass YSR-Resonanzen dazu verwendet werden können den imaginären Teil des supraleitenden Ordnungsparameters zu erfassen. Oft beobachtete Asymmetrien in den Kohärenzmaxima von Supraleitern könnten von diesem Phänomen herrühren. Wir zeigen außerdem eine erste Analyse der Variationen des kritischen Josephson Stromes in NbSe<sub>2</sub>. Unsere Daten lassen eine lokale Änderung des supraleitenden Ordnungsparameters um 20 % in der Umgebung der Fe Defekte erwarten.

Stichwörter:

Josephson-Rastertunnelmikroskopie (JRTM)

Multiband-Supraleitung

Paarbrechende Potentiale

Supraleitender Ordnungsparameter

Yu-Shiba-Rusinov Zustände

Andreev-Reflektionen

Einkanaltransmission

Quanten-Rückwirkung

Dynamische Coulomb Blockade (DCB)

# Acknowledgements

Before starting the scientific part I want to express my gratitude to the people that were involved in achieving the presented work or participated in other ways that made this thesis possible.

First of all I want to thank Klaus Kern for accepting me as a PhD student in his group and providing an excellent working environment with lots of freedom. I have the deepest respect for him and the scientific achievements he realized here at the MPI in Stuttgart.

I am grateful to Christian Ast and Markus Etzkorn, who guided me through my work as a PhD student. Also their proofreading of this thesis was certainly important to reach its final stage. I really enjoyed working together with them. The many hours in the lab and also discussing physics were not only highly educational for me but also a lot of fun.

I want to express my gratitude to the members of my thesis committee; Vincenzo Savona, Harald Brune, Elke Scheer and Peter Liljeroth for taking the time to review my PhD studies.

I want to thank Carmen Rubio Verdú for the time we shared together working at Box 1 on science stuffs. It was a truly awesome time.

Berthold Jäck and Matthias Eltschka have my sincere thanks for introducing me to the ways of the machine and paving the way for my work. I want to especially acknowledge Bert for the fruitful work on our joint publications.

Joachim Ankerhold has my gratitude for the various enlightening meetings and the fruitful collaboration.

Inspiring discussions with Alexander Balatsky, Francesco Tafuri, Fabien Portier, Carlos Cuevas, Annica Black-Schaffer, Wolfgang Beltzig, Andreas Rost, Markus Ternes, Jochen Mannhart, Hans Boschker, Jurgen Smet helped a lot in developing my understanding of the different topics that emerged during my studies.

I thank the many people, who made the work possible: Wolfgang Stiepany, Peter Andler, Marco Memmler, our IT-department, the electronics-group, the low temperature service and more.

## Acknowledgements

---

The general conditions and friendly atmosphere at the institute, ranging from the staff helping with travel forms to the security guards were outstanding.

I am grateful to Christopher Leon for proofreading parts of this thesis.

A special thanks to my office and PL buddies, colleagues and friends: Shai Mangel, Rico Gutzler, Diana Hoetger, Robert Drost, Anna Roslawska, Tomasz Michnowicz, Haonan Huang, Andreas Topp, Christopher Leon, Bastian Kern, Abhishek Grewal, Piotr Kot, Sebastian Koslowski, Christian Dette, Sabine Abb, Verena Schendel and many more for a great time at the MPI.

I am grateful to Sabine Birtel for keeping control over all organizational problems.

Matthias Bode and Jens Kügel have my thanks, because I got part of my motivation to start a PhD on the mK-STM in the time I spend in Matthias' group during my master studies.

I thank my parents for supporting me on my way through life.

The most significant and personally important support came from my partner Katharina, who always had my back and enabled me to spend way too much time with this thesis. I am thankful to our daughter for cheering me up and helping me to forget, whatever imaginary problem was sitting on my mind and for our joint bike trips to and from work, which kept me in shape.

*Stuttgart, 01 May 2018*

Jacob Senkpiel



# Contents

<b>Abstract</b>	<b>i</b>
<b>Zusammenfassung</b>	<b>iii</b>
<b>Acknowledgements</b>	<b>v</b>
<b>List of figures</b>	<b>ix</b>
<b>1 Introduction</b>	<b>1</b>
<b>2 Tunneling between superconductors</b>	<b>3</b>
2.1 Tunneling and scanning tunneling microscopy . . . . .	3
2.1.1 The concept of tunneling particles . . . . .	3
2.1.2 Scanning tunneling microscopy . . . . .	6
2.2 Superconductivity . . . . .	8
2.2.1 Local pair breaking potentials – Yu-Shiba-Rusinov states . . . . .	11
2.2.2 The Josephson effect . . . . .	14
<b>3 Description of the experimental setup</b>	<b>17</b>
3.1 The milli-Kelvin scanning tunneling microscope . . . . .	17
3.1.1 Operation principle . . . . .	19
3.1.2 The Precision Laboratory . . . . .	20
3.1.3 Stability improvements . . . . .	22
3.1.4 Energy resolution enhancement . . . . .	22
3.2 The physical characteristics of mK-STM . . . . .	24
3.2.1 The Dynamical Coulomb Blockade . . . . .	24
3.2.2 Junction influence on the energy resolution . . . . .	32
3.2.3 The capacitance of the tunnel junction . . . . .	35
3.3 Conclusions . . . . .	36
<b>4 Transmission channels in atomic contacts</b>	<b>39</b>
4.1 Andreev reflections . . . . .	40
4.2 Modeling transport channels in atomic contacts . . . . .	41
4.3 Transport in a single channel Al-STM junction . . . . .	47
4.4 Conclusions . . . . .	54

## Contents

---

<b>5</b>	<b>Effects of single channel transport at high transmission</b>	<b>55</b>
5.1	Transmission dependence of the Josephson effect . . . . .	55
5.2	Transmission dependence of the dynamical Coulomb blockade . . . . .	61
5.3	Conclusions . . . . .	63
<b>6</b>	<b>Pair breaking potentials in a superconductor with two coupled bands</b>	<b>65</b>
6.1	NbSe <sub>2</sub> basics . . . . .	65
6.2	Modeling the quasi-particle spectrum of multi-band superconductors . . . . .	67
6.3	Fe-doped NbSe <sub>2</sub> probed with a V-tip . . . . .	69
6.3.1	Yu-Shiba-Rusinov resonances in a two-band superconductor with complex order parameter . . . . .	73
6.3.2	Josephson effect in multi-band superconductors . . . . .	82
6.4	Conclusions . . . . .	85
<b>7</b>	<b>Conclusions and Outlook</b>	<b>87</b>
	<b>Bibliography</b>	<b>110</b>
	<b>Photographic credits</b>	<b>111</b>
	<b>Curriculum Vitae</b>	<b>113</b>
	<b>Publications</b>	<b>115</b>

# List of Figures

2.1	Tunneling process in an energy diagram. . . . .	4
2.2	Influence of the tip orbitals on the imaging of a surface. . . . .	7
2.3	Cooper Pairs. . . . .	9
2.4	Comparison of a bare BCS gap and one altered by magnetic impurities, Maki theory. . . . .	10
2.5	Sketch of an impurity interaction with a superconducting host. . . . .	13
2.6	Sketch of the wave function overlap of two superconducting baths. . . . .	14
2.7	Measurement of the Josephson effect in voltage and current biased mode. . . . .	16
3.1	STM-head developed for the mK-STM. . . . .	18
3.2	The mK-STM in the Precision Laboratory . . . . .	21
3.3	Mechanical stability of the experimental setup. . . . .	22
3.4	Influence of optimizations in grounding and filtering on the energy resolution. . . . .	23
3.5	Model of the dynamical Coulomb blockade. . . . .	25
3.6	Sketch of the STM junction and equivalent circuit diagram. . . . .	25
3.7	Energy diagram for tunneling in the dynamical Coulomb blockade regime. . . . .	26
3.8	Calculated $P(E)$ -function for two tips with different diameter and different capacitance $C_j$ . . . . .	27
3.9	Modelling the Josephson effect, quasi-particle tunneling and the dynamical Coulomb blockade based on one characteristic $P(E)$ -function . . . . .	31
3.10	Influence of tip sample capacitance on the broadening of spectroscopic features. . . . .	33
3.11	Comparison of broadening intrinsic to a junction's capacitance with broadening due to temperature. . . . .	35
3.12	Simple analytical model to estimate the junction capacitance. . . . .	36
4.1	Illustration of quasiparticle tunneling and (multiple) Andreev reflections in an SIS junction. . . . .	40
4.2	Experimental observation of Andreev reflections at different junction conductances. . . . .	41
4.3	Schematic drawing of the single channel junction in the theoretical model. . . . .	44
4.4	Numerical result for zero temperature of $IV$ - and $dI/dV$ -curves for an SIS junction. . . . .	46
4.5	Typical surface of the Al(100) crystal and extraction of a single atom. . . . .	48

## List of Figures

---

4.6	Approach curve on an aluminum adatom on the surface of Al(100) and extracted excess current . . . . .	49
4.7	Andreev reflection spectra from very low to very high transmission. . . . .	50
4.8	Andreev fits to experimental $IV$ -curves on a single Al-adatom. . . . .	52
4.9	Spectroscopy on a single adatom on the surface of an Al(100) crystal. . . . .	53
5.1	Illustration of our Josephson junction made of one single Al-atom at the end of each electrode. . . . .	56
5.2	Single channel Josephson spectra from low to high conductance. . . . .	58
5.3	Limits of the modeling at very high transmission. . . . .	59
5.4	Theoretical comparison of the many channel and the few channel Josephson tunneling model. . . . .	61
5.5	Approach curve to a single adatom in the normal conducting phase. . . . .	62
5.6	Conductance dependence of the dynamical Coulomb blockade. . . . .	63
6.1	Topography of Fe doped NbSe <sub>2</sub> . . . . .	66
6.2	Quasi-particle spectrum for a multiband-superconductor with magnetic background scattering. . . . .	68
6.3	Order parameters of Fe-doped NbSe <sub>2</sub> . . . . .	69
6.4	$dI/dV$ -curve and topography of V(100). . . . .	71
6.5	Fit to the superconducting gap of Fe-doped NbSe <sub>2</sub> . . . . .	73
6.6	Typical NbSe <sub>2</sub> Fe-defect topography and spectroscopy. . . . .	74
6.7	Calculated YSR-states in NbSe <sub>2</sub> . . . . .	76
6.8	Theoretical analysis of the relation between YSR-peak width and energy position. . . . .	78
6.9	YSR-peak spectra from experimental data and from the theoretical model. . . . .	79
6.10	Comparison of experimental YSR-peak widths with theory. . . . .	80
6.11	Correlation of YSR quasi-particle and Josephson spectroscopy. . . . .	84
6.12	Plot of key maps of one Fe-defect grid spectroscopy. . . . .	85

# 1 Introduction

Scanning tunneling spectroscopy (STS) at ultra-low temperature received more and more interest in the past years with many specially custom-built dilution refrigeration based experiments [Song10, Misra13, Assig13, Haan14, Roychowdhury14, Allwörden18]. Also commercially available scanning tunneling microscopes (STM) reach well below 1 K now. <sup>1</sup> Due to these technical advances and the coinciding improvements in spectroscopic energy resolution interesting quantum phenomena become better accessible or observable at all in the STM. On the other hand temperatures in the milli-Kelvin range also let the quantum-back action of the STM junction's electromagnetic environment gain a significant influence on the tunneling process [Ingold92, Ast16].

To use the STM for a detailed and quantitative study of a sample, it is therefore important to gain an in depth understanding of this effect on the measurement of spectroscopic features. We will detail how to minimize the back-action and with this its limiting effect on the experiments spectral energy resolution.

A key aspect in this thesis is superconductivity. It is one of the most interesting physical phenomena and has been under investigation now for more than 100 years. In spite of the significant interest in basic research and also for industrial applications, due to the undeniable leaps it would bring for many technologies, there are still lots of unresolved questions and the goal of realizing superconductivity (SC) at room temperature is nowhere close to be reached. In topical research with scanning tunneling microscopy the atomic scale investigation of superconductivity and also its interaction with magnetism gathers more attention.

The study of Yu-Shiba-Rusinov-states, which result from the interaction of impurities with superconductivity [Yazdani97, Hudson01, Ji08, Franke11, Ruby16, Cornils17, Choi17, Choi, Heinrich18, Kezilebieke18] and their connection to the attempts to demonstrate Majorana bound states [Potter12, Das12, Nadj-Perge14, Feldman16, Ruby15b, Lv17, Jeon17] attracted a lot of attention in the last years. We contribute to this field by demonstrating the emergence of YSR-resonances outside of the superconducting gap, at the position of the coherence peaks,

---

<sup>1</sup>Unisoku USM1300.

## Chapter 1. Introduction

---

and connect their lifetime to the imaginary part of the underlying superconducting substrate. By this it is possible to determine to what amount states residing inside the gap are protected against relaxation [Heinrich13] and it may help to find the best suited environment to realize long-lived quantum states necessary for quantum sensing, computation and simulation [Suter16]. Including the possibility of YSR-resonances at the position of the coherence peaks may account for oftentimes observed asymmetries in superconducting gaps.

The recently discovered unconventional superconductivity in sheets of graphene rotated by an angle of about  $1.1^\circ$  [Cao18] is quite interesting because it consists of only one element, much unlike most other SC with unconventional pairing. To study this material and to find clues on the details of the pairing mechanism Josephson scanning tunneling microscopy (JSTM) [Šmakov01, Graham17] may be the ideal tool [Jäck15b, Jäck15a, Randeria16].

This thesis is structured in the following way. It begins with a short description of the relevant physical phenomena in chapter 2. After that the experiment and its important characteristics are explained in chapter 3. We then elaborate on our findings concerning the tunneling process in a single channel junction in chapters 4 and 5, where we study the Josephson effect and the dynamical Coulomb blockade. The last chapter (6) is concerned with the interaction of local magnetic moments with a superconductor with two coupled bands.

## 2 Tunneling between superconductors

In this first part the thesis we will introduce some physics important for the understanding of the experimental work to follow. All explanations will be on a basic level, possibly restricted to giving a phenomenological idea. In case there is interest for further reading there shall be some recommendations in the text. We will start with introducing the principle of tunneling measurements, leading to the scanning tunneling microscope. After that, the most relevant properties of superconductivity are noted down together with their experimental signatures. Then local perturbations of SC will be discussed, leading to Yu-Shiba-Rusinov-resonances and spatial variations of the pairing amplitude of the superconducting order parameter. After that the Josephson-effect, describing the transport of Cooper pairs between superconducting reservoirs, will be introduced. At the end of this chapter the Josephson-effect as a means to probe local changes of the superconducting order parameter in the STM, will be highlighted.

### 2.1 Tunneling and scanning tunneling microscopy

#### 2.1.1 The concept of tunneling particles

The concept of tunneling particles goes back to the work of Louis de Broglie<sup>1</sup> who in 1923 proposed the duality of particle and wave nature of matter [Broglie23]. Following this concept one can assign a wavelength  $\lambda$  to a particle with mass  $m$  and speed  $v$ :

$$\lambda = \frac{h}{mv}, \tag{2.1}$$

where  $h$  is Planck's constant.  $h$  as link of a photon's energy  $E$  and frequency  $\nu$  was proposed by Max Planck<sup>2</sup> in 1900 to satisfy  $E = h\nu$  [Planck00] and is contained in the explanation of the

---

<sup>1</sup>De Broglie was awarded the Nobel price in Physics 1929: "for his discovery of the wave nature of electrons" [Nobel Media AB18].

<sup>2</sup>Planck was awarded the Nobel price in Physics 1918: "in recognition of the services he rendered to the advancement of Physics by his discovery of energy quanta" [Nobel Media AB18].

## Chapter 2. Tunneling between superconductors

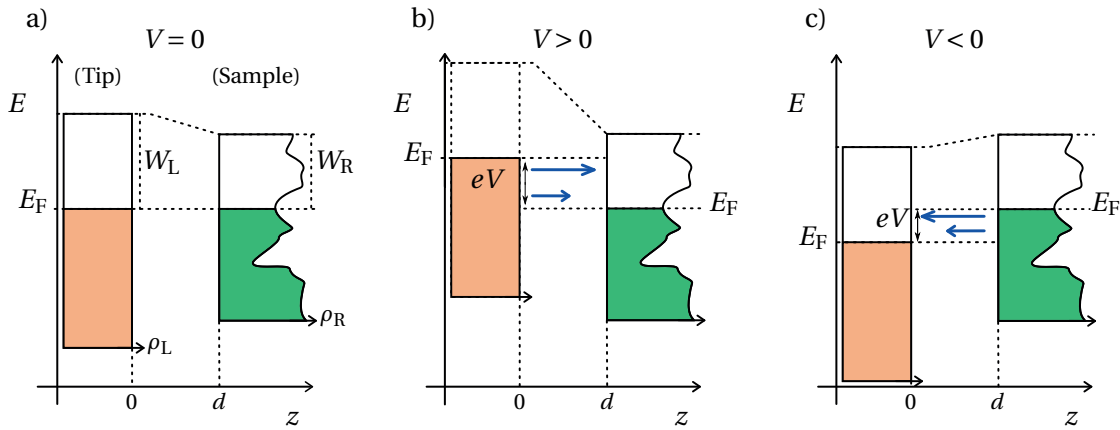


Figure 2.1 – **Tunneling process in an energy diagram.** In this figure some important parameters for tunneling are illustrated. In a) the stationary case is shown, where no external voltage  $V$  is applied. The densities of states of the two electrodes (tip and sample) are aligned at their Fermi energies. The work functions  $W_{L,R}$  give the barrier that is needed to excite electrons to vacuum. No net current  $I$  is flowing because the currents in both directions have the same size. b) represents the case where a positive voltage is applied on the tip-electrode. Electrons now tunnel from occupied states between  $E_F$  and  $E_F + eV$  to the unoccupied states above  $E_F$  in the sample. A negative  $V$  will reverse the current flow, c). With a flat DOS in the reference electrode (tip) one can therefore probe the unoccupied and occupied states of a sample.

photoelectric effect by Albert Einstein<sup>3</sup>, demonstrating the quantization and thereby, particle behavior of light waves [Einstein05]. Therefore, tunneling of electrons has its foundation in the very basics of quantum physics. Imagining electrons as wave-packets yields a picture, where their wave function in one conductor can have an overlap with another conductor, separated by some distance. This overlap gives the electrons a finite probability to exist in the nearby conductor, although separated by an energy barrier. Traversing this barrier, which is impossible to cross for an electron in the classical picture, is the process of quantum mechanical tunneling. A sketch relating the relevant properties is displayed in figure 2.1. Two electrodes, one on the left (L) and one on the right (R) are shown, both have a density of states (DOS)  $\rho_{L,R}$ .<sup>4</sup> For simplicity the DOS of the tip is assumed constant. The work functions  $W_{L,R}$  describe the energy needed to excite an electron to the vacuum level, resulting in a classical energy barrier. The distance  $d$  between the electrodes changes the overlap of the wave functions. Because no bias voltage  $V$  is applied between the electrodes, no net tunneling current  $I$  is flowing. If a positive bias  $V > 0$  is applied on the tip, electrons from its occupied states can tunnel into unoccupied states of the sample, b). In case of a negative bias  $V < 0$  the process is reversed, as shown in c). Because  $I$  is dependent on the DOS, it is possible to measure it for one electrode, if the DOS of the other electrode is known or constant.

<sup>3</sup>Einstein was awarded the Nobel price in Physics 1921: “for his services to Theoretical Physics, and especially for his discovery of the law of the photoelectric effect” [Nobel Media AB18].

<sup>4</sup>In the latter description of the scanning tunneling microscope the electrodes are tip and sample.



## 2.1. Tunneling and scanning tunneling microscopy

A possible basis for the theoretical analysis of the tunneling current is found in the work of Erwin Schrödinger<sup>5</sup> who developed the framework to describe the time evolution of a system's wave function [Schrödinger26]. This framework was used by John Bardeen<sup>6</sup> to derive an equation for the tunneling current  $I$  in the one-dimensional case [Bardeen61]. By simplifying the problem with several assumptions<sup>7</sup> the tunneling current  $I$  can be derived from the overlap of the electrodes wave functions [Chen07]:

$$I(V) = \frac{4\pi e}{\hbar} \int_{-\infty}^{\infty} [f(E_F - eV + \epsilon) - f(E_F + \epsilon)] \times \rho_L(E_F - eV + \epsilon) \rho_R(E_F + \epsilon) |M|^2 d\epsilon, \quad (2.2)$$

with the tunneling matrix element  $M$  and the Fermi distribution, describing the temperature dependent smearing of the DOS:

$$f(E) = \frac{1}{1 + \exp\left(\frac{E - E_F}{k_B T}\right)}. \quad (2.3)$$

The influence of the specific materials used as electrodes as well as the distance between them enters  $|M|$ . The wave functions are represented by the decay constant  $\kappa_0$  of the averaged work-function and the work functions by  $W_{L,R}$ .

$$M(\epsilon) = M(0) \cdot e^{-\frac{\kappa_0 \epsilon d}{W_L + W_R}}, \quad (2.4)$$

where  $d$  is the separation of the two electrodes. If the broadening of spectroscopic features is not significant (because of a low enough temperature) one may ignore the Fermi function. Additionally, assuming a constant tunneling matrix element  $|M|$  over the energy range of interest, one gets the simple relation:

$$I(V) \propto \int_0^{eV} \rho_L(E_F - eV + \epsilon) \rho_R(E_F + \epsilon) d\epsilon. \quad (2.5)$$

Clearly, a measured current follows from the convolution of the two electrode's densities of states. And the differential conductance signal is directly proportional to the convolution of the electrodes densities of states:

$$dG(V) = \left( \frac{dI}{dU} \right)_{U=V} \approx \rho_L(E_F + eV) \rho_R(E_F). \quad (2.6)$$

Obtaining the structure of the density of states in a tunneling experiment was achieved by Leo

<sup>5</sup>Schrödinger was awarded the Nobel prize in Physics 1933: "for the discovery of new productive forms of atomic theory" [Nobel Media AB18].

<sup>6</sup>Bardeen was awarded the Nobel prize in physics 1956 together with William Shockley and Walter Brattain: "for their researches on semiconductors and their discovery of the transistor effect" [Nobel Media AB18].

<sup>7</sup>The simplifications are given by assuming: orthogonal tip and sample states, weak tunneling, electron-electron interactions can be ignored, independent tip and sample DOS unaltered by the tunneling and electrochemical equilibrium between tip and sample [Gottlieb06]

## Chapter 2. Tunneling between superconductors

---

Esaki<sup>8</sup> and P.J. Stiles in 1965 [Esaki65].

Another possibility to look at the tunneling process is based on conduction channels between the electrodes, each supporting a maximal current at a certain voltage, defined by the quantum of conductance  $G_0 = \frac{2e^2}{\pi h}$ , with  $h$  being the Planck constant. According to the Landauer theory, the tunneling process between several states in each electrode can be split in pairs with one state in each electrode, yielding one transport channel each [Landauer87, Chen07]. In the tunneling regime the conductance is then given by the sum of the transmission coefficients  $T_N \propto \rho_L \rho_R$  ranging between 0 and 1 over all  $N$  channels:

$$G = G_0 \sum_N T_N. \quad (2.7)$$

An experimental signature of the quantized transport channels is the integer Quantum Hall effect demonstrated by Klaus von Klitzing [Klitzing80]<sup>9</sup>. Another demonstration is the transport in quantum point contacts [van Wees88, Wharam88]. We will get back to the idea of transmission channels later in chapter 4, where it will be necessary to describe the Josephson effect in the few channel limit in our experiment.

### 2.1.2 Scanning tunneling microscopy

Scanning tunneling microscopy adds some very useful options to tunneling experiments. The most obvious and renown capability is probably the imaging of surfaces with atomic precision, based on the exponential dependence of tunneling current  $I$  and distance between the electrodes  $d$ . Another is the manipulation of single atoms or molecules on the surface. The electrodes in the scanning tunneling microscope (STM) are a conducting sample and a conducting wire with an atomically sharp apex, the tip.

Control over the distance  $d$ , as well as the lateral position of the tip with respect to the sample is realized by piezoelectric motors and actuators, adding some complexity to the experimental setup. After the invention of the STM by Gerd Binnig and Heinrich Rohrer<sup>10</sup> in 1982 [Binnig82] STM quickly evolved to a powerful measurement technique, not only to image surfaces but also for (local) spectroscopic analysis of electronic material properties. The details of the tunneling process was studied by Tersoff and Hamann [Tersoff83, Tersoff85] who found in 1983 a quantitative theoretical description using a spherical tip, finding that STM images the local density of states (DOS). They used Bardeen's approach and included the tip with a spherical potential originating in a point, without any geometric features, significantly simplifying the description of the tips states. The most important result is that the STM measures the DOS of the sample in a local fashion, instead of the atomic structure directly, assuming a constant tip

---

<sup>8</sup>Esaki was awarded the Nobel price in Physics 1973 (together with Giaever and Josephson): "for their experimental discoveries regarding tunneling phenomena in semiconductors and superconductors, respectively" [Nobel Media AB18].

<sup>9</sup>Von Klitzing was awarded the Nobel prize in physics 1985: "for the discovery of the quantized Hall effect" [Nobel Media AB18].

<sup>10</sup>Rohrer and Binnig were awarded the Nobel price in Physics 1986: "for their design of the scanning tunneling microscope" [Nobel Media AB18].

## 2.1. Tunneling and scanning tunneling microscopy

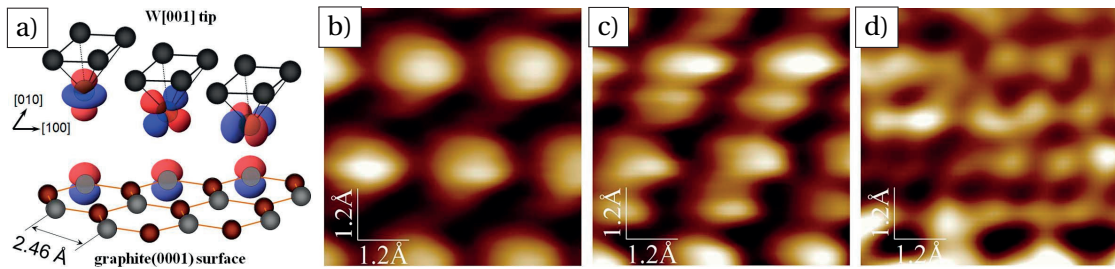


Figure 2.2 – **Influence of the tip orbitals on the imaging of a surface.** Current dependent imaging of a graphite surface with the different  $d$ -orbitals of a W(001) tip, with current increasing from b) to d). Demonstrating that an STM measurement is always a convolution of tip and sample properties, i.e. the smallest structure (orbital) is the probe, irrespective of belonging to tip or sample. Image taken from [Chaika14], under: CC BY-NC-SA 3.0.

DOS [Chen07]. The differential conductance<sup>11</sup>  $dG$  is then proportional to the local DOS of the sample  $\rho_S$ :

$$dG = \frac{dI}{dV} \propto \rho_S(E_F + eV, r_0). \quad (2.8)$$

For feature sizes larger than  $\approx 1$  nm STM images can be modeled with good agreement, but for atomically resolved images the reproductions fails. A model reproducing the topographic resolution of STM down to the atomic level, and by that the transport properties can be achieved, by taking into account all possible electronic orbitals at the tip apex and the sample surface. Because the STM does not directly probe height, but the local DOS, especially at the atomic level, the location of surface atoms does not have to be at the same position where the locally measured signal is the strongest [Barth90]. Imagining the tip apex to feature either  $s$ -,  $p$ - or  $d$ -orbitals illustrates the problem. Depending on which orbital it is, the overlap of the tips states with the sample states has to change. To demonstrate the effect of probing a surface with different tip orbitals let us now consider some experimental data by Chaika et al. [Chaika14]. In figure 2.2 the influence of the orbital structure of the tip on the imaging of a surface becomes rather obvious. In a) the orbitals of a W(001)-tip and a graphite(0001)-surface are depicted. In b), c) and d) measurements of the surface at successively higher conductance are shown, where the scanning of the surface is strongly dominated by the differently oriented  $d$ -orbitals of the tip, effectively the tip's orbitals are periodically imaged on the sample. One impressive consequence of the possibility to restrict the transport in the STM down to a single orbital is that one can directly observe the quantum of conductance in a single atom junction of  $s$ -like metals [Levy Yeyati97]. Another interesting outcome of the detailed analysis of the tunneling process is that even an inversion of contrast can be achieved. For further reading, especially for all the derivations of the theoretical models we want to direct the reader to the 'Introduction to Scanning Tunneling Microscopy' by Julian Chen [Chen07].

<sup>11</sup>The differential conductance can be obtained either numerically from a measured  $IV$ -curve or directly by a lock-in measurement.

A difficulty with planar junctions is that the measurements average over some area, possibly including defects, which alter the results, i.e. early Tedrow-Meservey-Fulde experiments [Meservey70, Tedrow71, Meservey94]. In the STM on the other hand, one can precisely choose, to either measure far away from a defect to obtain cleaner result of the substrate properties or, which may even be more interesting, go on purpose to the location of a defect to look at the interactions changing the substrate's properties.

### 2.2 Superconductivity

The phenomenon of vanishing resistance, known as superconductivity, was discovered in 1911 by Heike Kamerlingh Onnes<sup>12</sup>. Superconductivity (SC) is actually not limited to dissipationless conduction of electricity but also includes a transition to perfect diamagnetism, expelling magnetic fields, an effect discovered by and named after Walther Meißner and Robert Ochsenfeld [Meissner33]. A first microscopic description of the effect was developed by John Bardeen, Leon Neil Cooper and John Robert Schrieffer<sup>13</sup>, the BCS-model [Bardeen57]. Its underlying idea is that electrons bind together to pairs, the so-called Cooper pairs, and condense into an energetically favorable ground-state. The basic idea is illustrated in figure 2.3. Electron  $e_1$  passes point  $x_0$  at time zero, the positively charged lattice atoms are slightly attracted by the electrons charge, resulting in a lattice deformation and a local positive charge. Another electron  $e_2$  is attracted by this charge after  $e_1$  moved on. This can be seen as an indirect coupling via phonon exchange with the lattice. A direct experimental demonstration of the importance of phonons for superconductivity is the isotope effect, published in 1950 by Emanuel Maxwell [Maxwell50] and Reynolds et al. [Reynolds50]. They could show, using different isotopes of a material that  $T_c$  is inversely proportional to the square root of the atomic mass of an element. To break one of these Cooper pairs the whole macroscopic ground state has to be excited, by which the energy scale to do so becomes rather large. This property results in one of the hallmarks of superconductivity, a symmetric gap in the density of states around  $E_F$ . The DOS  $\rho$  has the form [Tinkham04]:

$$\rho_{\text{BCS}}(E) = \text{sign}(E) \Re \frac{E}{\sqrt{E^2 - \Delta^2}}, \quad (2.9)$$

where  $E$  is the energy and  $\Delta$  is the order parameter of the superconductor, giving the size of the energy gap. This DOS gap is shown in figure 2.4 a) in blue, the height of the peaks is infinite, due to the singularity at the order parameter, here  $\Delta = 710 \mu\text{eV}$ . It was first measured by Ivar Giaever in 1962 in a tunneling experiment [Giaever61, Giaever62]. The size of the gap in BCS SCs is equivalent with the real part of the order parameter  $\Delta$  [Tinkham04]:

$$\Delta_{\text{BCS}} = \frac{\hbar\omega_D}{\sinh(1/(\rho_N(E_F)V_0))} \approx 2\hbar\omega_D e^{-1/(\rho_N(E_F)V_0)}. \quad (2.10)$$

<sup>12</sup>Onnes was awarded the Nobel price in Physics 1913: “for his investigations on the properties of matter at low temperatures which led, inter alia, to the production of liquid helium” [Nobel Media AB18].

<sup>13</sup>Bardeen, Cooper and Schrieffer were awarded the Nobel price in Physics 1972: “for their jointly developed theory of superconductivity, usually called the BCS theory” [Nobel Media AB18].

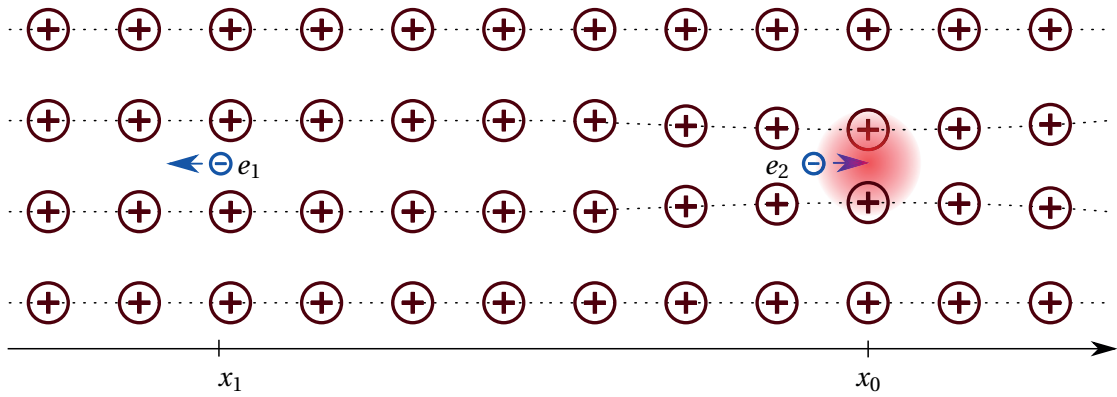


Figure 2.3 – **Cooper Pairs.** Electron one ( $e_1$ ) passed position  $x_0$  at time  $t_0$ , slightly deforming the lattice and creating a local positive charge (red area). After a time of the order  $\approx 1$  ps  $e_1$  moved about 100 nm to position  $x_1$  and  $e_2$  is attracted by the local charge created by  $e_1$ . The two electrons have opposite momenta.

The order parameter is thereby defined by the following material parameters:

1. size of the normal state density of states at Fermi energy  $\rho_N(E_F)$ ,
2. the coupling potential  $V_0$ , including the attractive electron-phonon and repulsive Coulomb interaction,
3. the Debye frequency  $\omega_D$ .

$\Delta_{\text{BCS}} = |\Delta_{\text{BCS}}| \cdot e^{i\phi}$  with the phase of the macroscopic ground-state wave function being  $\phi$ . The BCS theory is consistent with many experimental results of some mostly general material parameters, like the ratio  $\frac{2\Delta}{T_c} = 3.53$ . An important characteristic length scale is the distance over which the superconducting condensate recovers from a perturbation. For instance a local transition between normal and superconducting state, induced by proximity to a magnet. This distance is the so-called coherence length  $\xi$ . In the BCS picture it is defined as:

$$\xi \equiv \frac{\hbar v_F}{\pi \Delta_{T=0}}. \quad (2.11)$$

Ultimately though the BCS model is restricted to the limit of weak coupling  $V_0$ . The model of viewing electrons as bound in a Cooper pair is of course limited in the sense that the electrons have opposite momentum and can extend over hundreds of nm. They are thereby not two electrons traveling together through the host crystal.

Following the uncertainty relation one can easily extract some simple approximations for the behavior of the Cooper pairs. With a binding energy of elemental SC in the range of  $E_{\text{CP}} \approx 1$  meV from which an interaction- or lifetime of  $\tau_{\text{CP}} = \hbar / E_{\text{CP}} \approx 1$  ps can be concluded, multiplied with a Fermi velocity  $v_F$ , one finds a value matching the scale of coherence length  $\xi$  [Tinkham04, Gross12].

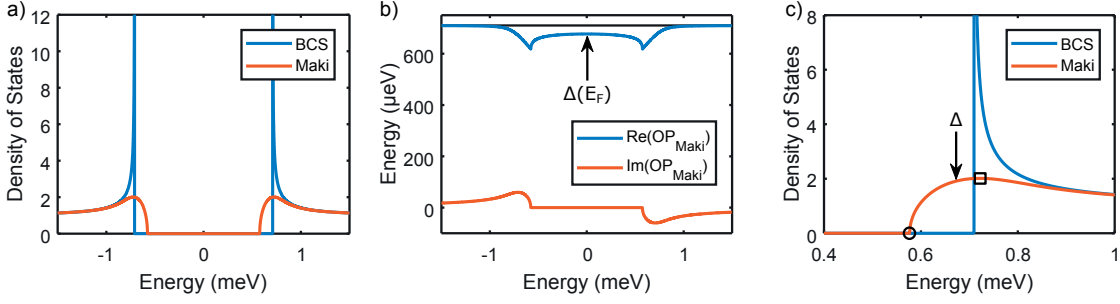


Figure 2.4 – **Comparison of a bare BCS gap and one altered by magnetic impurities, Maki theory.** While in the bare case, at zero temperature, the gap-edge, the coherence peak maximum and the order parameter  $\Delta$  are at the same energy, their values differ when impurities are induced, as modeled with the Maki theory. In a) the density of states of a BCS gap of  $710 \mu\text{eV}$  is plotted in blue together with the density of states of a Maki gap in orange, one can see the influence of the background of magnetic impurities on the quasi-particle spectrum. The Maki DOS has the dimensionless parameter  $\zeta=0.042$ . In b) the order parameter corresponding to the Maki model is plotted. The real part of the order parameter resembles its magnitude, it is not constant anymore as for the simple BCS case (black line). The value at zero voltage, which has to be used in the Josephson effect for instance, is significantly reduced (black arrow). In c) a zoom of the DOS is shown to highlight the differences between gap-edge at  $577 \mu\text{eV}$  (circle), the coherence peak maximum at  $722 \mu\text{eV}$  (rectangle) and the actual order parameter at  $677 \mu\text{eV}$  (arrow) in the perturbed DOS.

**Some extensions used in this work:** To introduce a broadening of the DOS the so called Dynes parameter  $\Gamma$  can be implemented  $E \rightarrow E + i\Gamma$ , making the energy complex [Dynes78]. The imaginary part of this phenomenological model introduces a finite quasi-particle lifetime inside the gap. Consequences of this will be investigated in chapter 6.3.1. An important possibility to adapt the BCS theory to superconductors with some macroscopic magnetic alteration, due to magnetic impurities, is the Maki model [Maki64, Worledge00]. The quasi-particle DOS of a superconductor in the Maki model, neglecting magnetic fields follows [Tinkham04]:

$$\rho_{\text{Maki}}(E) = \text{sign}(E) \Re \left( \frac{u}{\sqrt{u^2 - 1}} \right), \quad u = \frac{E}{\Delta_{\text{BCS}}} + \frac{\zeta u}{\sqrt{1 - u^2}} \quad (2.12)$$

$\Delta_{\text{BCS}}$  is the unperturbed order parameter and  $\zeta$  is the depairing parameter. The now energy dependent order parameter is given by:

$$\Delta_{\text{Maki}}(E) = \Delta_{\text{BCS}} - \zeta \frac{\Delta_{\text{Maki}}(E)}{\sqrt{\Delta_{\text{Maki}}^2(E) - E^2}}. \quad (2.13)$$

The Maki density of states with a large but realistic depairing parameter, is plotted together with the BCS DOS in figure 2.4 a), showing the significant effect of magnetic scattering in bulk SC. In addition to altering the DOS, the depairing also renders the order parameter energy dependent, as demonstrated in b). Using  $\Delta_{\text{BCS}} = 710 \mu\text{eV}$  and a depairing  $\zeta = 0.042$  as



input parameters the resulting order parameter at the Fermi energy is reduced to  $\Delta(E_F)_{\text{Maki}} = 677 \mu\text{eV}$ . In c) we take a closer look at the difference of the gap-edge, the coherence peak maximum and the value of the order parameter. While these entities are at the same energy for a BCS-like DOS and thereby make the order parameter easily accessible, this is not true anymore for a Maki-like DOS.

A tunneling effect closely related to superconductivity is the filling of the gap upon increasing tunneling conductance. We will study responsible process, Andreev reflection in chapter 4.

### 2.2.1 Local pair breaking potentials – Yu-Shiba-Rusinov states

The interaction of a local pair breaking potential, for instance due to a magnetic moment, with a superconductor was described by Luh Yu, Hiroyuki Shiba and A.I. Rusinov [Yu65, Shiba68, Rusinov69a], in the following abbreviated as YSR. Later more advanced theory concerned with the local effects of impurities on superconductivity [Salkola97, Flatté97b, Flatté97a] was developed, introducing the phenomenon as an ideal field to study by STM. Early experimental STM work on YSR interactions was done by Ali Yazdani et al. in 1997 [Yazdani97] followed for instance by E. W. Hudson in 2001 [Hudson01] and in 2008 by Shuai-Hua Ji [Ji08] with significantly enhanced energy resolution.

A review, covering in length the theoretical background of YSR-states was written by Alexander Balatsky et al. in 2006 [Balatsky06]. The experimental STM accomplishments concerning YSR-states on  $s$ -wave superconductors can be found in the recent review of Benjamin Heinrich et al., from 2018 [Heinrich18].

Following Balatsky et al., the effect of a single paramagnetic impurity in an  $s$ -wave BCS-like superconductor, is described on the next pages. The impurity induces a bound state with energy [Yu65, Rusinov69b, Balatsky06]:

$$E_{\text{YSR}} = \Delta \cos(\delta^+ - \delta^-). \quad (2.14)$$

Where  $\Delta$  is the superconducting order parameter and  $\delta^\pm$  are the phase shifts for spin-up (+) and spin-down (−) electrons:

$$\tan(\delta^\pm) = \pi \rho_N(E_F) \cdot (V \pm JS/2). \quad (2.15)$$

The phase shifts are defined by the normal state density of states at the Fermi energy  $N(E_F)$ , the Coulomb potential  $V$  and the magnetic potential  $J$ , as well as the spin  $S$  of the impurity. One can directly see that for non-magnetic scattering the YSR-state has to be at the energy of the order parameter  $\Delta$ , the gap-edge in the pure BCS-case. Magnetic scattering induces states at energies lower than  $\Delta$ , and can move the YSR-state towards the center of the superconducting gap. For purely magnetic scattering and spherically symmetric exchange  $J$  the

## Chapter 2. Tunneling between superconductors

---

energy simplifies to [Shiba68, Balatsky06]:

$$E_{\text{YSR}} = \Delta \frac{1 - (JS\pi\rho_N(E_F))^2}{1 + (JS\pi\rho_N(E_F))^2}. \quad (2.16)$$

The wave functions for electron  $u(r)$  and hole  $v(r)$  part of the YSR-resonance are [Rusinov69a, Balatsky06]:

$$u(r), v(r) \propto \frac{\sin(k_F r + \delta^{+,-})}{k_F r} \exp\left(-r \left| \sin(\delta^+ - \delta^-) \right| \frac{1}{\xi}\right) \quad (2.17)$$

From the above equation, it follows that the wave-functions are typically out of phase and have a characteristic oscillation in space, defined by the Fermi vector  $k_F$  and an overall decay that is given by the coherence length  $\xi$  and  $k_F$ . YSR-resonances appear as peaks in the quasi-particle spectrum that are symmetric in the energy position and usually asymmetric in peak height. An illustration describing the above effect is given in figure 2.5. A spin (red) is placed on a superconducting substrate (blue). When a Cooper pair enters the vicinity of the impurity-spin, its electrons (spin-up and spin-down for a singlet CP) interact with it via Coulomb and exchange coupling, creating a bound state. This bound state can now be excited at energies below  $\Delta$ , yielding resonance-peaks in the superconducting gap. Should the exchange coupling  $J$  exceed the pairing energy  $\Delta$ , the system undergoes a quantum phase transition where the magnetic ground-state changes [Balatsky06]. In this case Cooper pairs break into Bogoliubov quasi-particles and the spectral asymmetry between the YSR-states can change its weight between positive and negative voltage [Salkola97, Hatter15].

Concurrently the order parameter can be affected by local potentials and is predicted to show oscillations in its amplitude [Schlottmann76, Balatsky06]:

$$d\Delta(r) \propto \begin{cases} \frac{1}{(k_F r)^3} \cdot \frac{\xi \Delta}{\omega_D} & \text{if } r \gg \xi, \\ \sin^2(k_F r) & \text{if } r \ll \xi \omega_D / E_F. \end{cases} \quad (2.18)$$

In the limit of very strong coupling, even a sign change of the macroscopic phase may occur [Salkola97]. The order parameter oscillations were also covered in [Flatté97b].

Experimentally the spatial extent of the YSR states found so far, for unknown defects in the 2D superconductor NbSe<sub>2</sub> have intensity modulations ranging at least 6 nm [Ménard15] and for Mn atoms on Pb(111) with observable oscillations for about 5 nm [Ruby16].<sup>14</sup> In both cases the oscillations are strongly spatially focused with 6 or 3 fold symmetry, respectively. The origin of this focused oscillation can be traced back to the Fermi surfaces of the material. Other interesting work resolved multiple YSR-states to different orbital origins [Ruby16, Choi17]

---

<sup>14</sup>The measurement with an STM actually probes the square of the YSR-wave function, resulting the oscillation frequency by half.



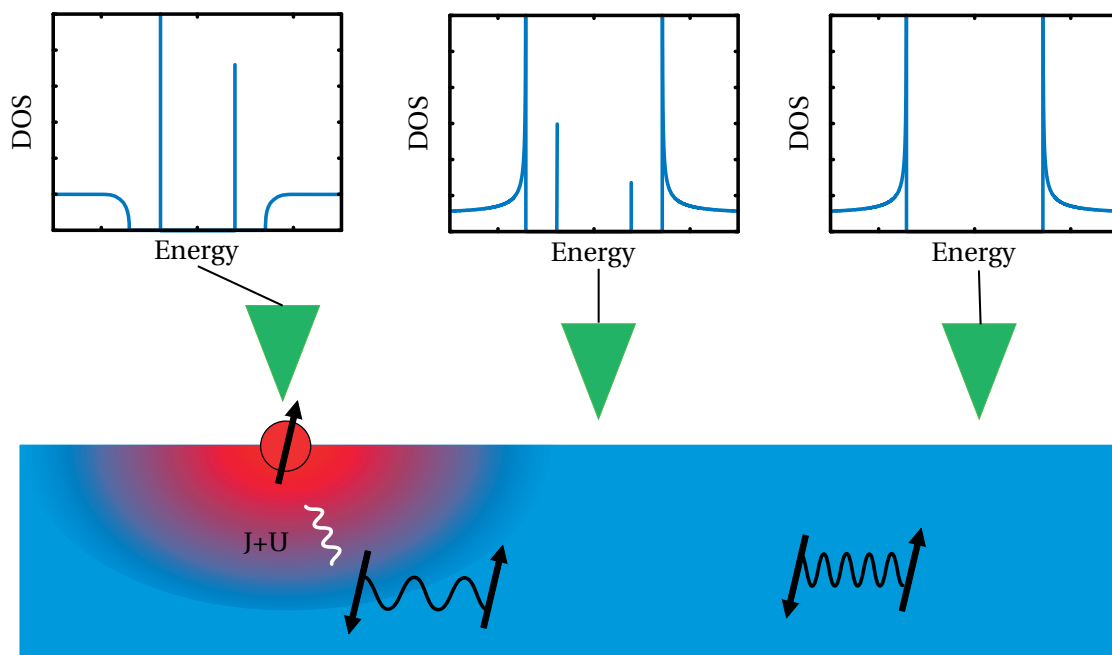


Figure 2.5 – **Sketch of an impurity interaction with a superconducting host.** An impurity (red) has a Coulomb potential  $U$  and an exchange potential  $J$ , which interact with a nearby Cooper pair. This interaction leads to a bound state, which gives YSR-resonance peaks in the density of states with typically asymmetric peak height. A local spectroscopy will measure oscillations of the peak intensity with distance  $r$  from the impurity center, until it decayed. Directly at scattering center the coherence peaks of the superconducting host are suppressed, further away a convolution of the YSR-peaks with the SC-gap is detected.

and study the effect of hybridization between single impurities [Ji08, Kezilebieke18, Choi]. Also the interplay of the YSR-effect and the Kondo-effect [Kondo64], coincidentally resulting from magnetic interactions with conduction electrons, was under investigation [Frankel11]. YSR-states in a BCS superconductor are protected from decay channels inside the gap [Heinrich13] but can experience some broadening induced by thermal decay [Ruby15a] or residual quasiparticles in the gap [Martin14]. In unconventional SCs, the situation can be different, for instance in d-wave SCs because of their non-trivial order parameter they display an intrinsic broadening of YSR-states [Salkola97, Hudson01]. YSR-resonances gained a lot of interest due to their relation to the possible realization of Majorana bound states in magnetic chains on a superconducting surface [Nadj-Perge14, Ruby15a].

We will return to the topic of YSR-resonances, concerning magnetic interactions with a superconductor with a complex valued and energy dependent order parameter, in chapter 6. We will show theoretical calculations and experimental data demonstrating YSR-peaks outside of the gap and resolve the origin of their significant spectral broadening.

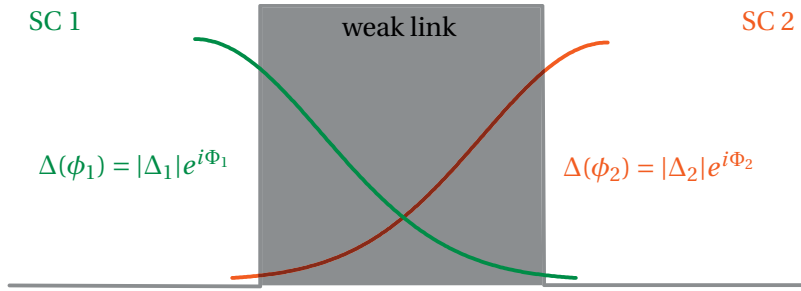


Figure 2.6 – **Sketch of the wave function overlap of two superconducting baths.** Similar as quasi-particles also Cooper pairs have a wave-function that extends outside of their host material. Given an overlap with another conductor Cooper pairs have a finite probability to travel through the energy barrier. If the second electrode is a superconductor the transfer occurs without the need of a bias energy. The current flow is driven by the difference of the phases  $\Phi_{1,2}$ . Its amplitude is defined by the size of the involved order parameters  $|\Delta_{1,2}|$  and the normal state conductance at Fermi energy  $G_N(E_F)$ . The actual maximal experimental current is reduced by broadening effects, interactions with the environment to the so called switching current  $I_s$ .

### 2.2.2 The Josephson effect

Brian Josephson derived the theory for the tunneling of Cooper pairs between superconductors in 1962 [Josephson62, Josephson64, Josephson65]<sup>15</sup>. He concluded that the difference of the macroscopic phases of two superconducting condensates  $\phi = \Phi_1 - \Phi_2$  drives a current at zero voltage. The maximal Cooper pair current that the junction can support is the critical Josephson current  $I_c$ . Two equations capture the basics of the Josephson effect. The first describes the DC Josephson effect: at a set phase difference  $\phi$  a current  $I$  will flow in the junction at zero voltage, following [Tinkham04]:

$$I(t) = I_c \sin(\phi(t)). \quad (2.19)$$

The second yields the AC Josephson effect: a voltage  $V$  applied to the junction has as a consequence that the phase difference will change with time:

$$\frac{d\phi}{dt} = \frac{2e}{\hbar} V. \quad (2.20)$$

Thereby an alternating current will flow with the energy  $\nu h = 2eV$ , enabling perfect conversion of frequency to voltage.<sup>16</sup> The basic element of a Josephson junction is the weak link between two superconducting electrodes. It is not restricted to tunneling; a narrow constriction in the

<sup>15</sup>Josephson was awarded the Nobel price in Physics 1973: “for his theoretical predictions of the properties of a supercurrent through a tunnel barrier, in particular those phenomena which are generally known as the Josephson effects” [Nobel Media AB18].

<sup>16</sup>For this reason the Josephson effect is used as the voltage standard, by the International Organization for Standardization (ISO).

dimensions of a superconductor is enough.

The strength of the coupling of the two phases is given by the Josephson coupling energy [Tinkham04]:

$$E_J = \frac{\hbar}{2e} I_C, \quad (2.21)$$

In the case where the weak link is a tunneling junction with identical electrodes, the critical current is given by the Ambegaokar-Baratoff relation [Ambegaokar63]:

$$I_C = G_N \frac{\pi \Delta}{2e} \tanh\left(\frac{\Delta}{2k_B T}\right). \quad (2.22)$$

$G_N$  is the normal state conductance and  $T$  the temperature. In the limit of zero temperature it reduces to:

$$I_C = G_N \frac{\pi \Delta}{2e}. \quad (2.23)$$

The Josephson effect also crucially depends on the ratios of the Josephson coupling energy  $E_J$  and the charging energy of the junction  $E_C$  [Iansiti87]:

$$E_C = \frac{Q^2}{2C_J}, \quad (2.24)$$

as well as the thermal energy  $E_{th}$ :

$$E_{th} = k_B T. \quad (2.25)$$

Significant thermal noise ( $E_{th}$ ) or capacitive noise ( $E_C$ ) in the junction, compared to  $E_J$ , can induce a premature switching out of the Cooper pair transport branch, because they induce fluctuations of the phase difference  $\phi$ . This results in a finite slope in the  $IV$ -curve around zero voltage and a reduced maximal current the junction can support, defined as the switching current  $I_s < I_C$ . An example of Josephson  $IV$ -curves demonstrating this effect is shown in figure 2.7. On the left side a voltage biased measurement is plotted and on the right hand side a current biased measurement of the same junction is shown. The voltage bias is the usual working mode of STM and is also used in the other experimental data presented in this thesis. To illustrate two important measurement parameters we show the exact same junction measured in the current biased mode. These are the switching current  $I_s$  and the retrapping current  $I_r$ , which mark the switching out of the ground state and the re-trapping into the ground state, respectively.<sup>17</sup>

The switching current  $I_s$  can be related to  $E_J$  and also to the order parameter  $\Delta$  in a junction

---

<sup>17</sup>In planar junction geometries (phase coherent tunneling) one may study the statistics of  $I_s$  to analyze the macroscopic quantum tunneling effect [Massarotti15].

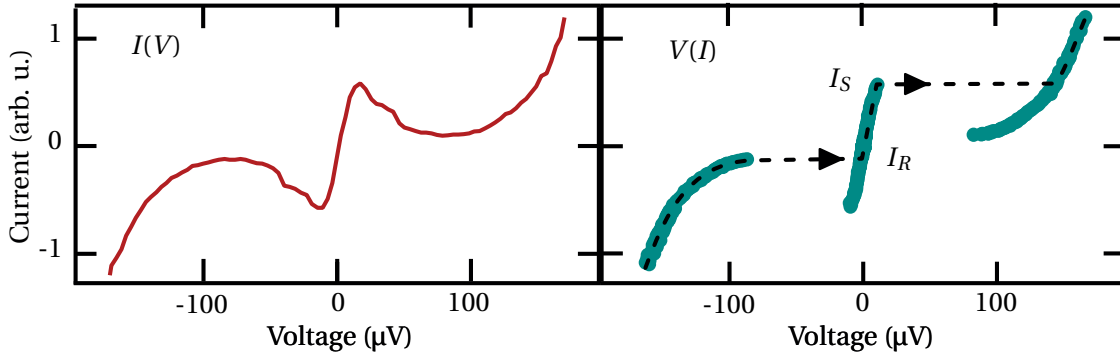


Figure 2.7 – **Measurement of the Josephson effect in voltage and current biased mode.** On the left side a  $I(V)$ -curve of a Al-Al junction is measured with a voltage bias. On the right side the same junction is measured in with a current bias. Here the directly accessible quantities, the switching current  $I_S$  and the retrapping current  $I_R$  are highlighted. An appropriate model can extract the Josephson critical current  $I_C$  from these measurements.

with non-negligible thermal energy  $E_{th}$  and  $E_J \approx E_C$  [Iansiti87]:

$$I_s \propto \frac{E_J^2}{E_C} \propto G_N^2 \Delta^2. \quad (2.26)$$

The quantum mechanical nature of the Josephson junction is also apparent in the commutator relation of charge  $Q$  and phase  $\phi$ :

$$[\phi, Q] = 2\pi e \quad (2.27)$$

If  $E_J \gg E_C$  the junction is in a regime, where the transport of Cooper pairs happens coherently and the phase  $\phi$  is a good quantum number. In the opposite case  $E_J \ll E_C$  the charge  $Q$  is a good quantum number and sequential tunneling takes place. The latter resembles the situation for typical STM junctions with a superconducting tip and sample, with a conductance in the tunneling regime and superconductors of low  $\Delta$  (elemental superconductors).

On of the first experimental observations of the Josephson effect was published in 1963 by P. W. Anderson and J. M. Rowell [Anderson63]. A review of Josephson physics can be found in [Seidel11] and a focus on the current-phase relation in [Golubov04].

## 3 Description of the experimental setup

### 3.1 The milli-Kelvin scanning tunneling microscope

The milli-Kelvin scanning tunneling microscope (mK-STM) was designed with the focus on reaching the limit in energy resolution for an STM experiment. A main obstacle in realizing this is the vibrational noise that a dilution refrigerator, which is necessary to cool down to milli-Kelvin temperatures continuously, may introduce to the STM junction.<sup>1</sup> Another very important point is allowing as little electromagnetic radiation as possible to get to the junction, because it would add an effective temperature, broadening spectroscopic features. The system comprises an ultra-high vacuum (UHV) preparation chamber for sputtering, annealing and cleaving of samples. Also several evaporators are mounted to expand the realm of sample systems to explore. To ensure the highest junction stability against mechanical vibrations a new STM-head was developed for the mK-STM, it is shown in figure 3.1. The sample transfer is realized from the bottom of the cryostat and has no line of sight. To prevent damaging the sample during transfer a guiding cone is mounted on the STM-head, directing the tip and sample in the correct position. An important point in the design is that the STM-head is completely closed, once the sample is screwed in. Having the junction fully enclosed with a metal shielding at base temperature helps to reach the best energy resolution. The construction and first experiments were published in 2013 and are detailed in the PhD-thesis of Maximilian Assig [Assig11, Assig13]. He demonstrated an effective temperature of 38 mK by fitting the superconducting gap of Al. This can also be expressed as a spectral energy broadening of  $\delta E = 3.5k_B T = 11.4\mu\text{eV}$ .

Experimental work with this new experiment covered, for instance, probing absolute spin polarization at the atomic scale [Eltchka14], based on the Tedrow-Meservey-Fulde (TMF) effect [Meservey94]. In this technique the spin-splitting of the superconducting density of states under magnetic fields, and the resulting spin dependent tunneling is used to resolve the magnetic structure of a sample. In this publication the variations of the spin-polarization of Co nano-island on Cu(111) were studied. Additionally, it was shown that the spin-polarization

---

<sup>1</sup>There are several other STM setups based on dilution refrigeration, e.g. [Moussy01, Suderow02, Kambara07, Song10, Marz10, Misra13, Roychowdhury14]

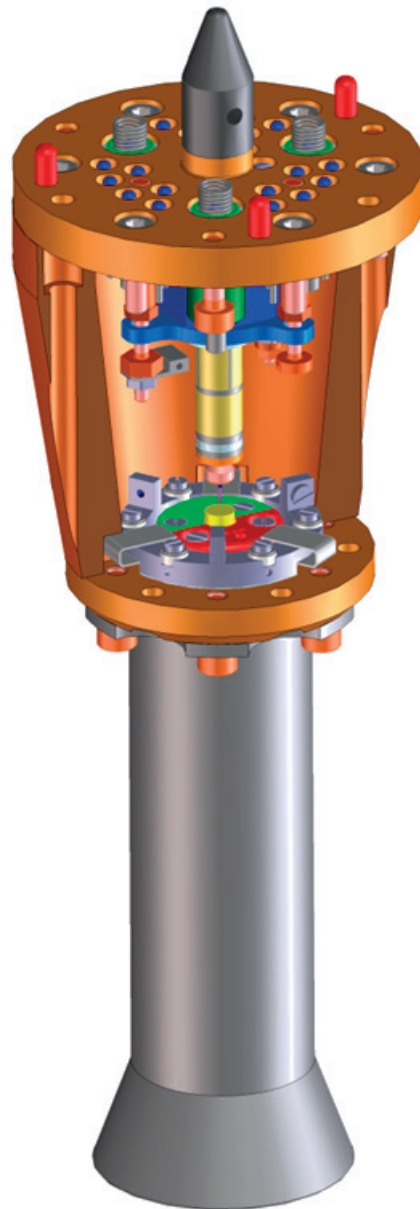


Figure 3.1 – **STM-head developed for the mK-STM.** To realize the highest mechanical stability of the junction and shielding against electromagnetic noise a special STM-head and sample-holder was developed for the mK-STM. In the lower part the guiding cone is visible in gray, on top of it the actual STM-head is shown in a copper-golden color. The sample-holder is screwed in the bottom of the head, the sample (yellow-golden) is mounted between the red and green colored thermocouples. The diameter of the sample is 6.2 mm. Directly above it the tip (pink) is mounted on the piezo-actuator (gray with yellow patches). On top of the head the electrical connections can be seen, marked in blue and green. [Assig13]

### 3.1. The milli-Kelvin scanning tunneling microscope

---

of the tunneling current depends on the tip-sample distance, demonstrating the different extend of spin-states into the vacuum. Furthermore, some first experiments concerning YSR-resonances from the interaction of CuPc-molecules on a V(100) surface were realized. This topics are part of the PhD-thesis of Matthias Eltschka [Eltschka15].

Another field of research with the mK-STM focused on the Josephson effect in STM junctions. It could be shown that the Cooper pair tunneling in the STM is characterized by the dynamical Coulomb blockade regime and the critical Josephson current  $I_c$  can be extracted from  $IV$ -curves with the  $P(E)$ -model. A result from this was the advance in the understanding of how the tunneling process in an STM at ultra-low temperatures is influenced by its electromagnetic environment. The electromagnetic environment was found to be given by the capacitance between tip and sample and by the tip's behavior as an  $\lambda/4$ -antenna [Jäck15b]. The findings about this research are detailed in the PhD-thesis of Berthold Jäck [Jäck15].

The work presented in this thesis would certainly not have been possible without the important research of the previous PhD-students.

#### 3.1.1 Operation principle

The cooling of the mK-STM is based a dilution refrigerator inset, which is shielded by liquid helium and nitrogen tanks from ambient temperature. The STM-head is thermally connected to the mixing chamber of the dilution refrigerator, the coldest point in the system.

Boiling of liquid nitrogen can introduce significant vibrations to STM experiments, to eliminate this disturbance we freeze the nitrogen, using a vacuum pump. In a dilution refrigerator system, achieving a temperature in the range of milli-Kelvin uses the separation of a  $^3\text{He}$  rich and a  $^3\text{He}$  poor phase of a  $^3\text{He}$ - $^4\text{He}$  mixture [Assig11]. The mixture is pre-cooled by coupling it to a helium reservoir at 1 K. This so-called 1 K-pot is cooled by pumping it with a vacuum pump. It can be used in a constant mode, where the flow from the helium tank is regulated with a needle-valve to achieve an equilibrium between the evaporated helium gas and the liquid helium refilling the reservoir. We found that this continuous mode introduces vibrations to the system, which reduce the junction stability significantly, therefore we operate the 1 K-pot in a single shot mode. This can easily be achieved, by closing the needle-valve which regulates the flow to the 1 K-pot. The possible continuous operation length of the system does not decrease because of this action, it is limited by the time the nitrogen tank empties, which is about 30 h. In this mode we get a strongly reduced level of mechanical vibrations in the junction.

To realize an STM with a dilution refrigerator needs strong pumps to cycle the mixture, which can introduce mechanical noise to the tunnel junction. An important task is therefore to find ways, to move the vacuum pumps away from the actual junction and to hinder vibrations and sound waves to travel along the necessary tube connections. Furthermore, the junction's susceptibility to noise should be reduced as much as possible.

An important measure to reach high spectral energy resolution, is to keep radio-frequency (RF) radiation from getting to the STM's junction. This was realized by adding filters with a cutoff frequency of about 10 kHz to all electrical connectors on the cryostat. More specifics of the cooling and operation are described in detail in the PhD thesis of M. Assig [Assig13].

### 3.1.2 The Precision Laboratory

In contrast to the work of previous PhD students working with the mK-STM all data was acquired in the new precision laboratory (PL) enabling significantly better experimental stability and reliability. The basic concept of the PL is to provide a lab environment to particularly sensitive experiments that ensures most reliable operation with reduced maintenance necessities. It helps to get as close as possible to the full potential of experiments.

Environmental influences that can significantly limit the performance of STM are vibrational and acoustic noise, which induce instabilities in the tunnel junction. Furthermore, electromagnetic radiation at radio frequencies (RF) limits the achievable energy resolution at low temperatures.

To protect experiments from these influences the PL provides 11 separated lab spaces (boxes) designed to the special needs of the hosted experiments and with possible future developments in mind. The box with the mK-STM is depicted in figure 3.2. The outer shell of the box is a welded steel Faraday cage with tightly closing metal doors suppressing RF-noise by 100 dB. All connections going into the box, also including cooling water and pump lines, are RF-filtered in order to prevent electromagnetic radiation from leaking to the inside. The structural basis of the box is made from concrete and built on an individual foundation. The walls provide an acoustic damping from the outside by 60 dB. Sounds originating from within the box are dampened by sound baffles on the walls and carpets on the floors. The experiment is mounted on a 100 t fiberglass reinforced concrete slab, which itself is supported by 12 air dampers, yielding an extremely low vibration level below  $10 \text{ nm s}^{-1}$ .

The necessary pumps are located next to the box in a separate room, with no direct structural connection. To reduce vibrations and acoustics traveling to the STM several steps of acoustic quieting are taken. This includes passive damping by coupling pumping lines to heavy masses, decoupling of parts of the line by T-dampers as well as active damping of tube movements.

A possible source for strong noise can be found in the He-recovery line. Fluctuations in the He pressure can be accounted for by damping the gas flow and using back pressure valves optimized for little noise emission.

Additionally, several isolated power grids are available to avoid electrical connections between the measurement electronics and electronics needed to run the experiment, like vacuum pumps or peripheral IT-equipment. Network connections are realized with optical fibers. The grounding of the otherwise galvanically isolated experiment is realized by a shielded separate ground connection.

Overall the lab provides exceptional conditions, which I am lucky to be provided with for my work. In my opinion, reliably good lab conditions cannot be overestimated in their importance.



### 3.1. The milli-Kelvin scanning tunneling microscope

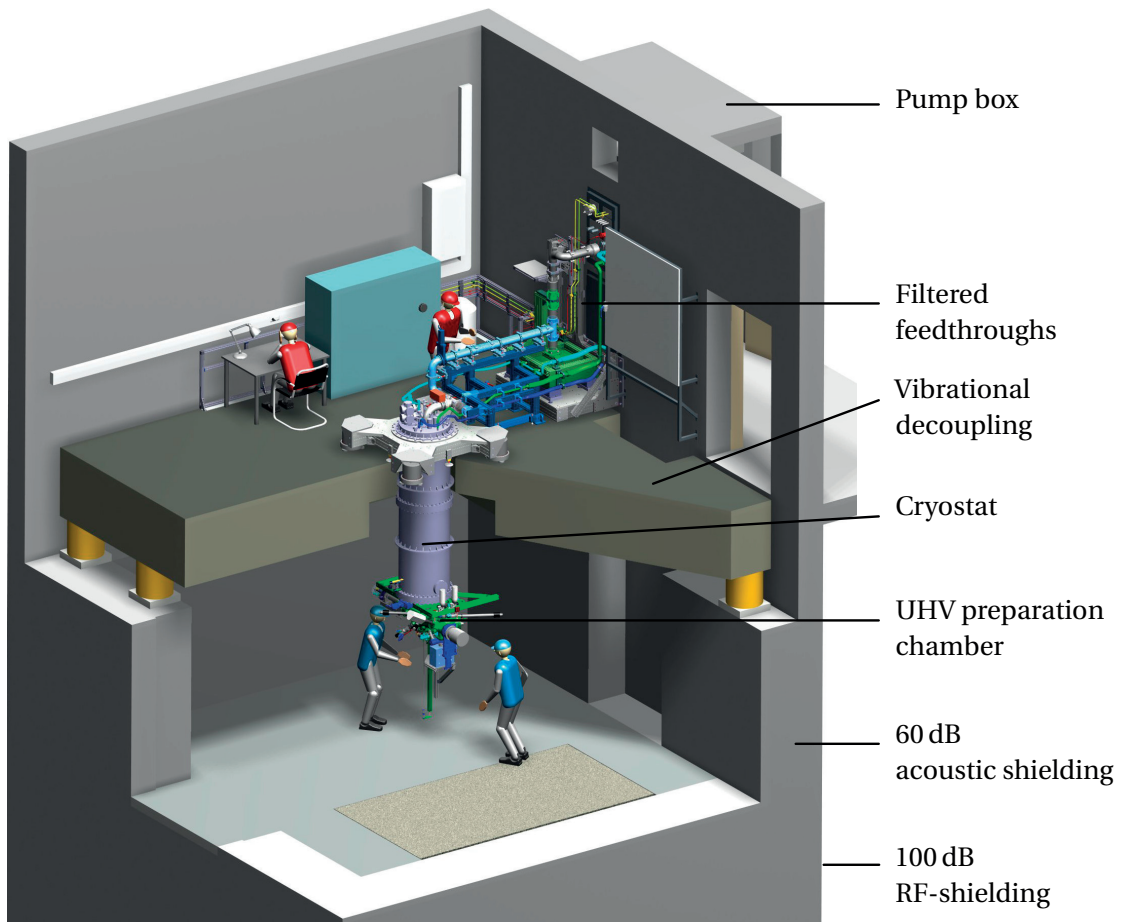


Figure 3.2 – **The mK-STM in the Precision Laboratory** Here the mK-STM is shown in its new lab environment located in the Precision Laboratory. Electromagnetic, acoustic and vibrational shielding/decoupling guaranty excellent working conditions for most sensitive experiments. The lab (box) has two floors, in the lower one the preparation chamber of the STM can be accessed and samples/tips are transferred from here. The preparation chamber is mounted at the bottom of the cryostat without any electrically conducting connection to it. The STM-head's position in the cryostat is approximately where the line is pointing that marks the cryostat. The whole experiment is mounted on a 100 t concrete slab in the upper floor. It has no connection to the walls and is fully supported on air springs (yellow). Here, on top of the cryostat are all the electrical connection going to the STM. Also the tubing for cycling the mixture and pumping the 1 K-pot and the nitrogen tank are going from here to the pump box next to the box with the experiment.

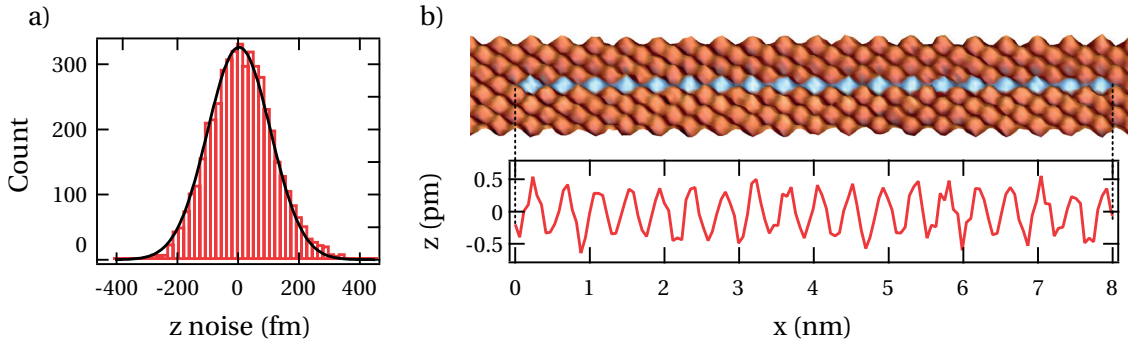


Figure 3.3 – **Mechanical stability of the experimental setup.** In a) the STM’s junction stability is analyzed in form of a histogram. It shows the noise obtained in a measurement at  $V_T = 1$  V,  $I_T = 1$  nA without feedback. A Gaussian fit yields a FWHM value of 250 fm. b) shows the topography of an Al(100) crystal,  $V_T = 10$  mV,  $I_T = 1$  nA. In white the position of the line cut below (representing raw data) is highlighted. It attests the high stability level realizable in a dilution refrigerator STM setup. All data taken at 15 mK.

### 3.1.3 Stability improvements

Here we want to give an idea about the enhancement of the STM-stability achieved by moving the machine to the PL and carefully optimizing the operation conditions. As described in the thesis of Maximilian Assig [Assig11] the vibrational noise between tip and sample in the old laboratory, located in the sixth floor of the institutes main building, was about 3.8 pm (FWHM). In comparison, after installing the mK-STM in Box 1 of the PL, as shown in figure 3.2 the typical vibrational noise reduced down to 250 fm. The data and fit of this measurement is depicted as a histogram in figure 3.3 a). This value of the mechanical stability is obtained with a sampling period of 20 ms. In figure 3.3 b) we present topography of an Al(100) crystal with a line scan of raw data attesting the excellent stability while operating the dilution refrigeration cycle.

### 3.1.4 Energy resolution enhancement

Working on the optimization of the STM we could enhance the energy resolution significantly by changing the electric grounding concept. A comparison of data before (green) and after (red) the change can be seen in figure 3.4. In (a) quasi-particle (QP) spectra are shown and in (b) Josephson IV-curves (J-IV). The data was acquired with an aluminum tip and an Al(100)-sample in the superconducting state at a temperature of 15 mK. In (c) the same junction was driven to the normal conducting state by applying a magnetic field at the same temperature. In this state the dynamical Coulomb blockade can be seen as a dip in spectroscopy, again revealing the increase of resolution. Panel d) shows the measurement circuit. The wires are low-pass filtered at the entry to the cryostat and carefully thermalized at all temperature stages. In the following we will introduce a model to describe the energy resolution in the STM and its dependence on the junction details.

### 3.1. The milli-Kelvin scanning tunneling microscope

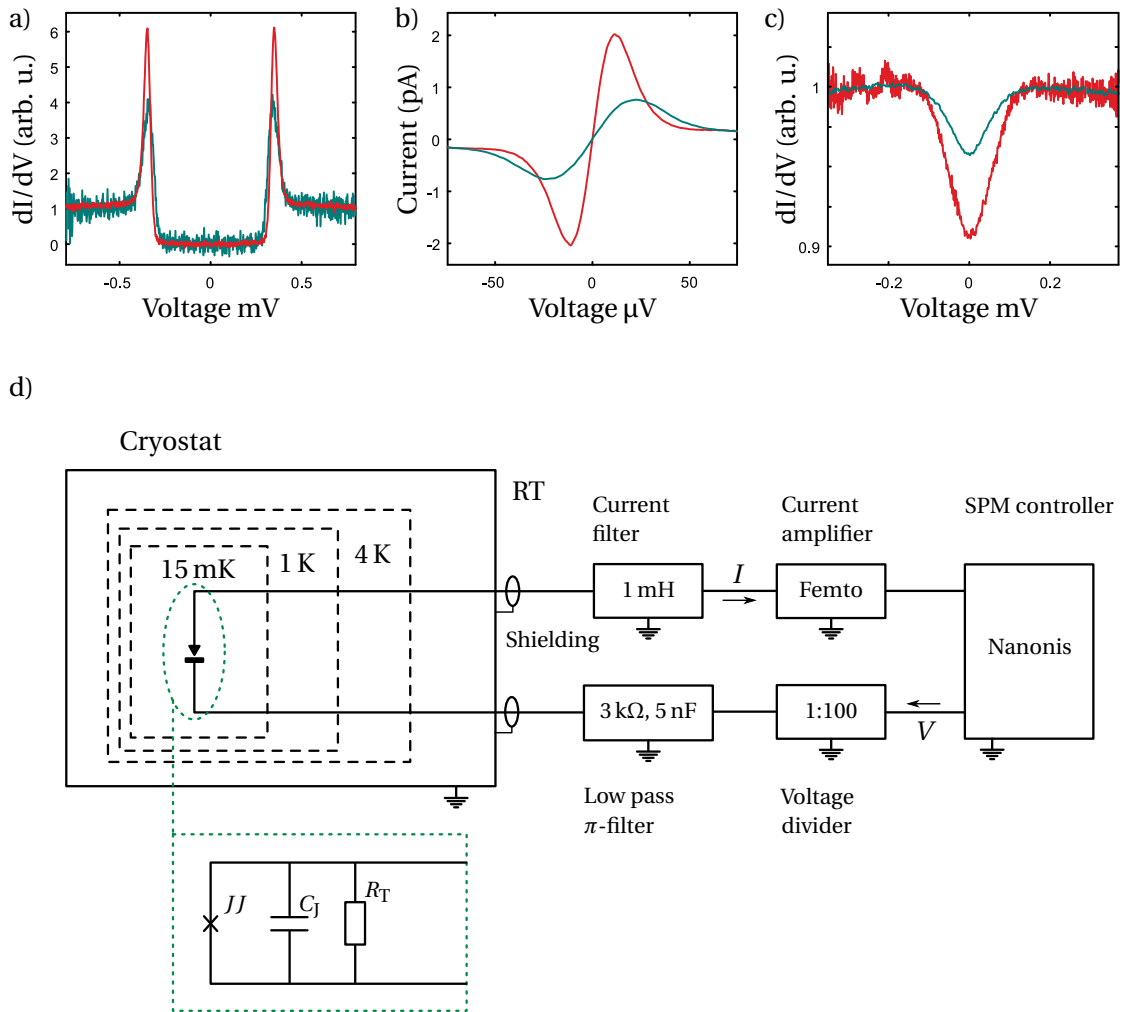


Figure 3.4 – **Influence of optimizations in grounding and filtering on the energy resolution.** Here we show the difference of the optimized conditions (red) in contrast to the non-optimized conditions (green) on spectroscopy. a) and b) show how the reduced broadening increases peak intensities in  $dI/dV$ -curves and Josephson  $IV$ -curves of the superconducting Al-Al STM junction, respectively. In b) the enhanced energy resolution is also apparent from the peak separation. c) presents data from the same junction in the normal conducting state. Here quenching superconductivity by a magnetic field reveals the dynamical Coulomb Blockade as a dip in spectroscopy. The differences in noise are a result of a different amount of averaged data. In d) the measurement circuit is shown. The bias voltage  $V$  is supplied by a Nanonis SPM controller, it is divided by a factor of 100 before being filtered by a low pass  $\pi$ -filter with a cut of frequency of about 10 kHz. The wiring is thermalized at each temperature stage. All wires outside of the cryostat are shielded (BNC) and the grounding is realized in a star shape manner, centered at a copper plate on top of the cryostat. The wire for the current measurement is filtered at the entry to the cryostat with an inductive filter before the signal is detected by a Femto transimpedance amplifier and passed to the Nanonis electronics. The tunnel junction (highlighted by a green dashed line) is not only given by its resistance  $R_T$  but also by the size of its capacitance  $C_J$

### 3.2 The physical characteristics of mK-STM

Scanning tunneling microscopy and spectroscopy at ultra-low temperatures is strongly affected by quantum effects inherent to the experiment. Spectroscopic measurements have to be analyzed taking into account these effects. At a temperature of 15 mK the thermal energy  $E_{\text{th}}$  is so small that characteristics of the STM junction itself like the charging energy  $E_C$  and even the electromagnetic behavior of the tip define the physics under investigation [Jäck15b]. A large charging energy in relation to a small thermal energy leads to a dynamical Coulomb blockade (DCB), which is directly observable as a dip in the conductance around zero voltage, with normal conducting tip and sample. We will now focus on the implications of this for the understanding of the physical phenomena under investigation.

#### 3.2.1 The Dynamical Coulomb Blockade

The dynamical Coulomb blockade (DCB) is a consequence of the quantization of charge, the capacitive nature of tunnel junctions and their electromagnetic environment. This quantum effect becomes observable, when the charging energy of the junction is large compared to the thermal energy  $E_{\text{th}} \ll E_C$ . The DCB is a dissipation effect for tunneling [Caldeira83, Devoret90]. A particle of charge  $Q$  can only tunnel, if it can excite an electromagnetic mode of the environment [Levy Yeyati01, Golubev01, Levy Yeyati05]. In a normal conducting junction this results in a reduction of the tunneling probability around zero voltage. It can be understood as a quantum back-action on the tunneling particles in STM, which probe the sample. In a tunnel junction with a capacitance  $C_j$  in the range of fF the blockade can be detectable up to a temperature of about 1 K.

The DCB is different from a Coulomb blockade, as observable for instance in a single electron transistor, where the blockade is a result of having no state available for tunneling. This naturally leads to a suppression of conductance, until states become available at high enough energy.

The energy exchange of the tunneling particles with the electromagnetic environment can be accounted for by the  $P(E)$ -theory, if the junction is in the low transmission range [Devoret90]. The DCB manifests as a dip in the differential conductance at zero bias for normal conducting electrodes. In figure 3.5 some exemplary plots of the DCB-dip are shown. The plot is calculated from the derivative of equation 3.17 in the next chapter. The effective temperature is  $T = 20$  mK, the junction capacitances are  $C_j = 10$  fF and 1 fF in a) and b) respectively. A bigger capacitance has the effect that the dip gets narrower and less deep. Additionally, the influence of the charge of the quasi-particles populating the electrodes is demonstrated for 1  $e$  in blue, but also for 3  $e$  in orange. With bigger quasi-particle charge the effect is smeared out by a larger capacitive junction noise. We will get to experimental results on the transmission dependence of the DCB and its similarity to the behavior of shot-noise in chapter 5.2.

Modeling a junction with the  $P(E)$ -function yields a quantum-model of the junction that is not only valid for the DCB (at low transmission) but also when tip and sample are superconducting.

### 3.2. The physical characteristics of mK-STM

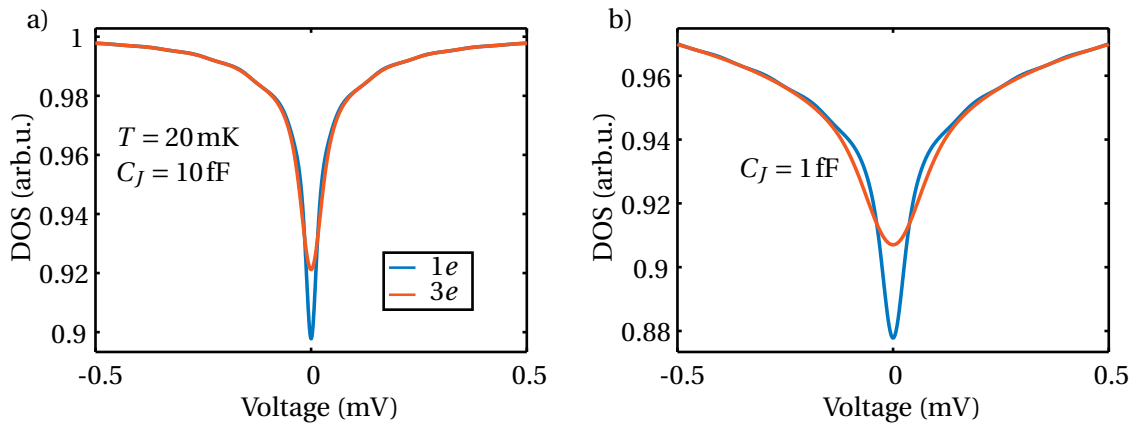


Figure 3.5 – **Model of the dynamical Coulomb blockade.** Comparison of the DCB for different junction capacitances  $C_J = 10\text{ fF}$ ,  $1\text{ fF}$  in a) and b) respectively. The temperature of the junction is  $T = 20\text{ mK}$ . Additionally, the dip is modeled not only for a quasi-particle charge  $Q$  of  $1e$  in blue, but also for  $3e$  in orange, to illustrate its influence. On top of the reduction the dips show a structure that relates to the details of the electromagnetic environment, i.e. possible resonance modes.

Taking it as the basis to describe broadening in quasi-particle spectra and  $IV$ -curves of the Josephson effect [Ingold94], the tunneling of Cooper pairs around zero voltage, achieves excellent quantitative agreement with experimental data. We will demonstrate this in the following.

#### Description of the tunnel junction: The $P(E)$ -model

Now we will elaborate on the details of the  $P(E)$ -function and show some examples. For superconducting electrodes the Josephson coupling energy  $E_J = \hbar I_0 / 2e$  comes into play for the description of the system.

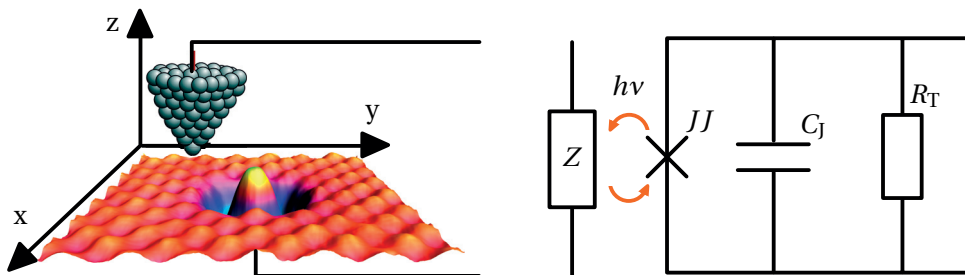


Figure 3.6 – **Sketch of the STM junction and equivalent circuit diagram.** The tunnel junction can be represented as a junction resistance  $R_T$  a junction capacitance  $C_J$  the tunneling element  $JJ$  and the electromagnetic environment  $Z$ . The tunneling characteristics are influenced by the energy exchange of the particles tunneling between tip and sample with the environmental impedance  $Z$ , for instance via photons with the energy  $h\nu$ .

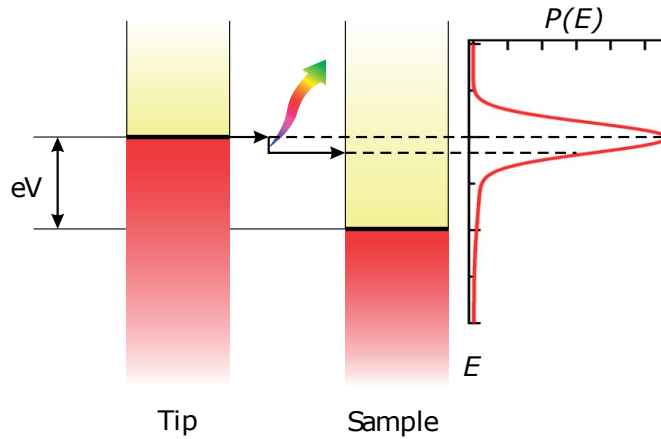


Figure 3.7 – **Energy diagram for tunneling in the dynamical Coulomb blockade regime.** Particles tunneling in the dynamical Coulomb blockade regime interact with the surrounding electromagnetic environment and can lose or gain energy by photon exchange with it. Electrons traveling through the vacuum between tip and sample will end in an energy distribution described by the  $P(E)$ -model. Taken from [Ast16].

The ratio of the three characterizing energies defines the physical regime of the junction. If  $E_J \ll E_C$ , the DCB has a characterizing order, Cooper Pairs (CP) tunnel sequentially, and  $E_J$  can be regarded as a perturbation of  $E_C$ . A suitable analytical approach to model the dynamical Coulomb blockade dip as well as the Josephson  $IV$ -curve is the  $P(E)$ -theory. It gives a probability for inelastic energy exchange between the tunneling particle and the environment [Ingold92, Ingold94]. It yields a characteristic quantum-model for a junction describing the quantum back-action on the tunneling particles. We find that it agrees excellently with our data for DCB-dip, Josephson  $IV$ -curve and quasi-particle (QP) spectra, where it reduces fit parameters to  $R_N$  and  $\Delta$ .

In figure 3.6 the STM-junction is represented on the left. On the right an equivalent circuit diagram of the junction is shown. The image of the STM junction helps to highlight the differences to other geometries, were the  $P(E)$ -model was used before. First, the weak link between the electrodes is not a constriction or an insulating oxide layer but vacuum. Second, the tip-electrode acts as a  $\lambda/4$ -antenna and has a dominating role in the electromagnetic environment [Jäck15]. These details are shown again in the equivalent circuit diagram in b). The Josephson junction can be represented by the Josephson contact ( $JJ$ ), the junction capacitance  $C_J$  and tunneling resistance  $R_T$  in parallel. Additionally, the vacuum impedance  $Z$ , with which the inelastic energy transfer of the tunneling particles takes place, is included. The exchange of photons with energy  $h\nu$  is symbolized by arrows.

We look a bit closer at the tunneling process in the energy diagram in figure 3.7. If a tunneling junction is in the DCB-regime particles with charges  $Q$  will lose or gain energy during the transfer. The inelastic energy transfer of the tunneling particles with the environment is described by a probability distribution following the so called  $P(E)$ -function.

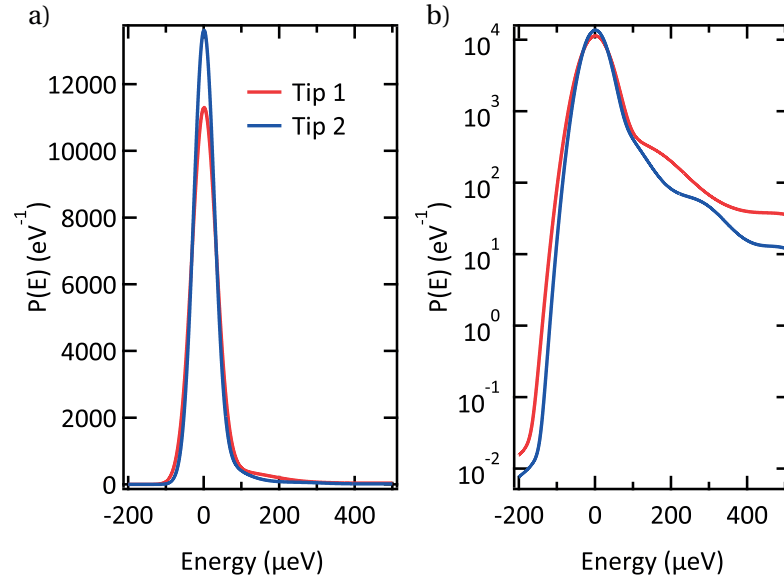


Figure 3.8 – Calculated  $P(E)$ -function for two tips with different diameter and different capacitance  $C_J$ . The function for tip 1 with a capacitance  $C_J \approx 3.5$  fF is plotted in red and the thicker tip 2, with  $C_J \approx 7.0$  fF is plotted in blue, see a). In b) the same figure is repeated with a logarithmic scale. Here the asymmetry of the  $P(E)$ -function becomes obvious. An analysis of the broadening effect of the different  $C_J$  follows in the next section. Figure taken from [Ast16].

The  $P(E)$ -function is defined with the equilibrium phase correlation function  $J(t)$  [Ingold94]:

$$P(E) = \int_{-\infty}^{\infty} dt \frac{1}{2\pi\hbar} \exp\left(J(t) + \frac{iEt}{\hbar}\right). \quad (3.1)$$

To include the capacitive noise as well as the energy exchange with the electromagnetic environment as independent processes we separate the correlation function to:

$$J(t) = J_0(t) + J_N(t). \quad (3.2)$$

$J_0(t)$  describes the electromagnetic environment. The phase correlation function of the capacitive noise is  $J_N(t)$ .

The probability distribution for the interaction with the electromagnetic environment  $P_0(E)$  is defined as [Ingold91]:

$$P_0(E) = I(E) + \int_{-\infty}^{\infty} d\omega K(E, \omega) P_0(E - \hbar\omega). \quad (3.3)$$



### Chapter 3. Description of the experimental setup

---

$K(E, \omega)$  is the integral kernel:

$$K(E, \omega) = \frac{\hbar E}{D^2 + E^2} k(\omega) + \frac{\hbar D}{D^2 + E^2} \kappa(\omega), \quad (3.4)$$

with:

$$k(\omega) = \frac{G_0 \Re Z_T(\omega)}{1 - e^{-\beta \hbar \omega}} - \frac{G_0 \Re Z_T(0)}{\beta \hbar \omega}. \quad (3.5)$$

$G_0$  is the quantum of conductance and  $\beta$ :

$$\beta = \frac{1}{k_B T}, \quad (3.6)$$

where  $T$  is the temperature. The function  $\kappa$  is given by:

$$\kappa(\omega) = \frac{G_0 \Im Z_T(\omega)}{1 - e^{-\beta \hbar \omega}} - \frac{2}{\beta \hbar} \sum_{n=1}^{\infty} \frac{G_0 Z_T(-i\nu_n) \nu_n}{\nu_n^2 + \omega^2}. \quad (3.7)$$

$\nu$  are the Matsubara frequencies:

$$\nu = \frac{1n\pi}{\hbar\beta}. \quad (3.8)$$

The inhomogeneity  $I(E)$  is defined as:

$$I(E) = \frac{1}{\pi} \frac{D}{D^2 + E^2}, \quad (3.9)$$

with:

$$D = \frac{G_0 \pi \Re Z_T(0)}{\beta}. \quad (3.10)$$

The total impedance  $Z_T(\omega)$  has a frequency  $\omega$  dependence and is characterized by the junction capacitance  $C_j$ :

$$Z_T(\omega) = \frac{1}{i\omega C_j + Z^{-1}(\omega)} \quad (3.11)$$

with:

$$Z(\omega) = R_{\text{env}} \frac{1 + \frac{i}{\alpha} \tan\left(\frac{\pi}{2} \frac{\omega}{\omega_0}\right)}{1 + i\alpha \tan\left(\frac{\pi}{2} \frac{\omega}{\omega_0}\right)} \quad (3.12)$$

$R_{\text{env}}$  is the effective d.c. resistance, in the STM this is the vacuum impedance  $R_{\text{env}} = 376.73 \Omega$ .  $\omega_0$  is the resonance frequency, in the STM dependent on the tip length and  $\alpha$  is an effective damping parameter [Jäck15b].



### 3.2. The physical characteristics of mK-STM

The probability distribution describing the thermal capacitive noise  $P_N(E)$  is modeled by a Gaussian [Ingold94]:

$$P_N(E) = \frac{1}{\sqrt{4\pi E_C k_B T}} \exp\left(-\frac{E^2}{4\pi E_C k_B T}\right). \quad (3.13)$$

The capacitive energy of the junction depends on the charge  $Q$  of the particles that populate it. It follows the relation:

$$E_C = \frac{Q^2}{2C_J}. \quad (3.14)$$

The full  $P(E)$ -function including the environmental part  $P_0(E)$  and the capacitive noise  $P_N(E)$  is then given by their convolution:

$$P(E) = \int_{-\infty}^{\infty} dE' P_0(E - E') P_N(E'). \quad (3.15)$$

The shape of the  $P(E)$ -function is displayed in figure 3.8. We have used two different junction capacitances (tip 1 and tip 2) the capacitance values are  $C_J(\text{tip 1}) \approx 3.5 \text{ fF}$  and  $C_J(\text{tip 2}) \approx 7.0 \text{ fF}$ . In a) the curves are plotted on a linear scale, revealing a reduced peak height for tip 1 with a smaller capacitance. The difference in the width of the two curves can be seen in the semi-logarithmic plot in b). The peak corresponding to tip 1 is broader. Because the  $P(E)$ -function obeys the detailed balance symmetry [Ingold91] the overall shape of the function is asymmetric. This asymmetry stems from the  $P_0(E)$ -function and the main part of the width from the capacitive noise in the junction, which are convolved. We will detail on this junction inherent broadening effect in the next section.

### Chapter 3. Description of the experimental setup

Deriving the tunneling probability in the junction under this inelastic influence, one obtains for one direction [Odintsov88, Devoret90]:

$$\vec{\Gamma}(V) = \frac{G_T}{e^2} \int_{-\infty}^{\infty} \int_{-\infty}^{\infty} dE dE' \rho_s(E' + eV) \rho_t(E) f(E) [1 - f(E' + eV)] P(E - E') \quad (3.16)$$

with the Fermi function  $f(E) = 1/(1 + \exp(E/k_B T))$ . In the case of vanishing interaction with the environment the  $P(E)$ -function is simply given by the delta function  $P(E) = \delta(E)$  and the standard symmetric transfer for tunneling is retained. The tunneling current is given by the difference of the tunneling rates in both directions:

$$I(V) = e \left( \vec{\Gamma}(V) - \overleftarrow{\Gamma}(V) \right). \quad (3.17)$$

The parameters for modeling the  $P(E)$ -function are:

Effective temperature	Junction capacitance	Damping factor	Environmental resistance	Particle charge	Resonance frequency
$T_{\text{eff}}$	$C_J$	$\alpha$	$R_{\text{env}}$	$Q$	$\omega_0$

Let us now consider the Josephson effect in this in the DCB regime, with a Josephson coupling energy  $E_J$  much smaller than the capacitive charging energy  $E_C$ . For some previous STM experiments the Ivanchenko-Zil'berman model [Ivanchenko69] was used to explain the data. Because this model is only valid in the classical phase diffusion limit, where  $E_C \ll E_{\text{th}}$  [Ivanchenko69, Ingold94], we cannot use it, because we are certainly not operating our experiment in this regime but rather in the opposite range, with  $E_C \gg E_{\text{th}}$ . Additionally, the resonances of the antenna like behavior of the STM-tip are not accounted for in the Ivanchenko-Zil'berman model. STM experiments with low  $T_c$  superconductors should generally be in the range, where the capacitive energy is larger than the Josephson coupling energy and therefore in the tunneling regime that is characterized by sequential transfer of charges.

For the description of the Josephson current the Josephson coupling energy  $E_J$  basically acts as a scaling parameter [Ingold94]:

$$I(V) = \frac{\pi e E_J^2}{\hbar} [P(2eV) - P(-2eV)] \quad (3.18)$$

To develop a comprehensive picture of the sequential charge tunneling in the DCB let us now consider its effect on some experimental examples. In figure 3.9 the  $P(E)$ -model is used to describe measurements of three different physical phenomena. Note that the same  $P(E)$ -function was used in all three fits. In a) the junction was forced to its normal conducting state with a magnetic field of 10 mT to measure the conductance dip around zero voltage, which is

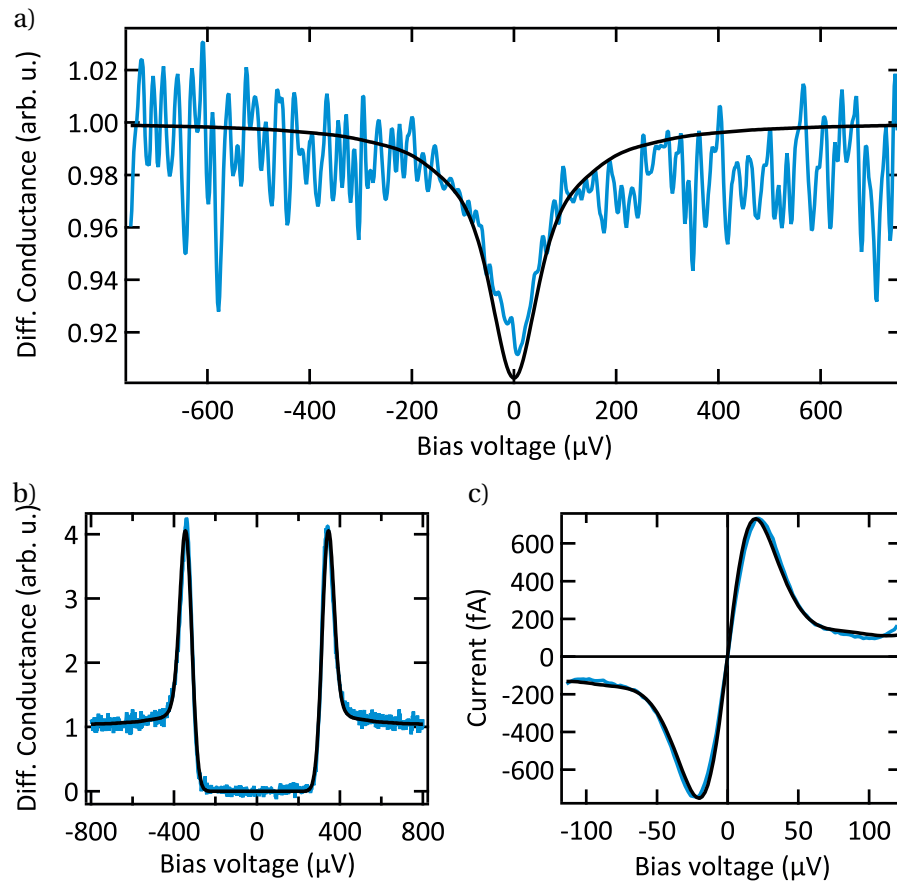


Figure 3.9 – **Modelling the Josephson effect, quasi-particle tunneling and the dynamical Coulomb blockade based on one characteristic  $P(E)$ -function.** Here we demonstrate, how the junction characteristic  $P(E)$ -model is able to describe measurements of three different physical phenomena. In a) a measurement of the dynamical Coulomb blockade is modeled with the derivative of equation 3.17. The normal conducting state of the junction was achieved by quenching superconductivity with a magnetic field of 10 mT. After turning off the magnetic field and retaining the superconducting phase in tip and sample a  $dI/dV$ -curve was measured. It is shown in b). Here the same  $P(E)$ -function (equation 3.15) is used to describe the broadening of the measurement which shows the convolution of two . The third application is the Josephson effect. The data and the fit based on equation 3.18 is plotted in c). Also here excellent agreement is found between fit and measurement. Data is plotted in blue and fits in black. Figure taken from [Ast16].

the hallmark of the dynamical Coulomb blockade. The fit was done based on the derivative of the tunnel current as described in equation 3.17. After reestablishing the superconducting phase of the junction we measured a  $dI/dV$ -curve resulting from the convolution of the gaped spectra of the two superconductors, at a low conductance. The data is presented in b), together with a fit based on the gap density of states as found in the BCS-theory (equation 2.9) only adding a convolution with the  $P(E)$ -function (equation 3.15) to describe the broadening. In panel c) we show the Josephson effect, which becomes apparent at higher conductance in the micro-volt range around zero volt. Again the fit is based on the same  $P(E)$ -function as is a) and b). The  $IV$ -curve can be modeled following equation 3.18 with excellent agreement. The used effective temperature is  $T = 100$  mK, the junction capacitance is  $C_J = 7$  fF, the damping factor is  $\alpha = 0.75$ , the environmental resistance is  $R_{\text{env}} = 376.73\Omega$  and the resonance energy is  $\hbar\omega_0 = 70\mu\text{eV}$ . The particle charge used is  $1e$  for the DCB and  $2e$  for the  $dI/dV$ -curve and the Josephson effect.

With the combination of these results the deep connection of the  $P(E)$ -model to the tunneling process in the STM is rather obvious. We have to understand it as the quantum-model of the STM-junction that governs the transfer of charges between tip and sample.

### 3.2.2 Junction influence on the energy resolution

We will now look closer on the part of the junction model that introduces the capacitive noise dominating the spectroscopic energy resolution in ultra-low scanning tunneling spectroscopy and other small capacitance tunneling experiments. This noise and therefore the restriction of the energy resolution is a direct consequence of the quantization of charge.

In our publication *Sensing the quantum limit in scanning tunneling spectroscopy*, by Christian R. Ast, Berthold Jäck, Jacob Senkpiel<sup>2</sup>, Matthias Eltschka, Markus Etzkorn, Joachim Ankerhold, and Klaus Kern, published in Nature Communication in 2016 we conclude that the junction itself poses a limiting effect on the achievable energy resolution in tunneling spectroscopy [Ast16]. The following chapter is based on this publication.

To better understand and test a model it is helpful to predict the effect of varying a parameter of the system under investigation. Therefore, we tested if an increase of the junction capacitance indeed reduces the observed broadening and is also consistent with the model's description of the Josephson effect. We chose Al as tip and sample material, because it shows narrow coherence peaks with very little intrinsic broadening. It therefore is an ideal material to test the junction inherent broadening. It is reasonable to assume that such a system will give the clearest result, because it can be nicely modeled with the simple BCS-description of superconductivity. We further decided to use the tip diameter as a means to change the capacitance  $C_J$  of the junction. The diameter of the tip wire was therefore increased from the standard of 0.25 mm to 1 mm.

---

<sup>2</sup>My contribution to this publication lies mainly in the experimental part and measurement of data. Naturally I also contributed with discussing the projects analysis and completing the manuscript.

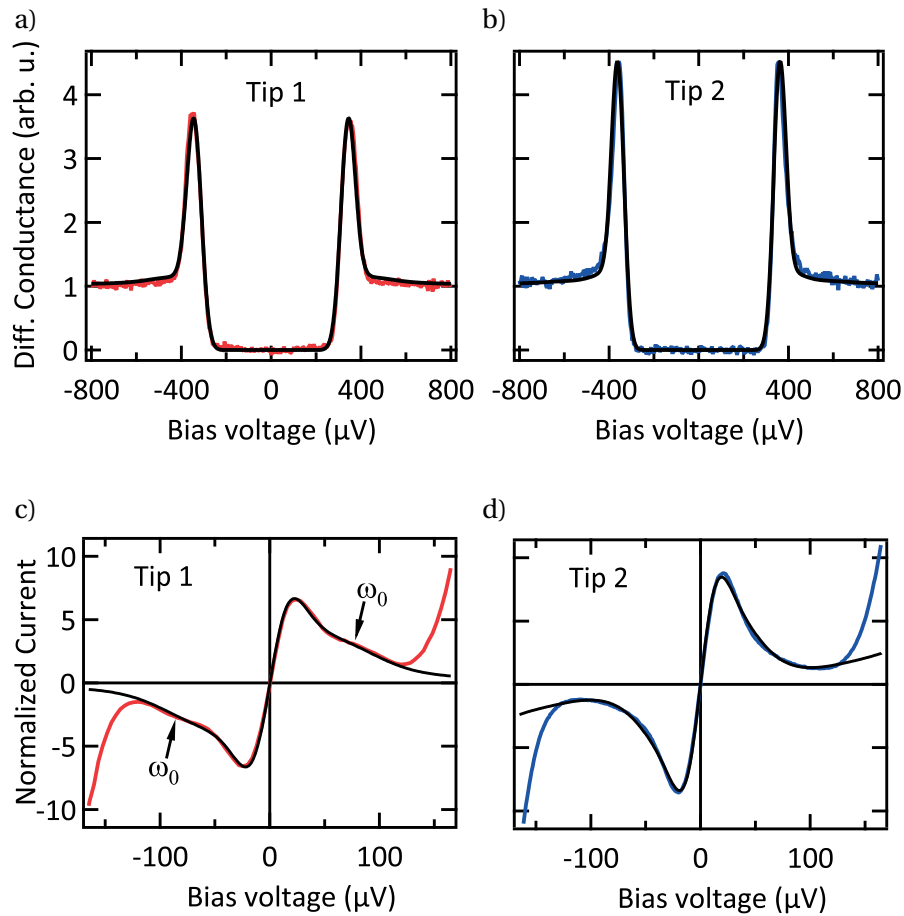


Figure 3.10 – **Influence of tip sample capacitance on the broadening of spectroscopic features.** To study the influence of the junction capacitance  $C_J$  on the energy resolution we build STM-tips from wires with significantly different diameter. For tip 1 a wire with 0.25 mm was used and for tip 2 a wire with 1 mm was used. In a) and b) the quasi-particle measurements are plotted together with BCS-like fits only perturbed by the broadening of the  $P(E)$ -function. The spectra were measured at a setpoint of  $V = 2$  mV and  $I = 50$  pA. In c) and d) the corresponding Josephson spectra are plotted together with fits based on the same  $P(E)$ -models used in a) and b), respectively. This demonstrates, how the  $P(E)$ -model and the capacitive noise therein governs the broadening of tunneling spectra in the STM for junctions with different  $C_J$ . The  $P(E)$ -functions used here are plotted in the previous section in figure 3.8. Figure taken from [Ast16].

### Chapter 3. Description of the experimental setup

---

In figure 3.10, the quasi-particle and Josephson spectra of these two tips are plotted. Tip 1 represents the tips with a wire diameter of 0.25 mm, the data obtained with it is colored in red. The measurements with the broader tip 2, with a wire diameter of 1 mm are plotted in blue. The presented data is significantly different for the two cases, although the tunneling conditions were the same. Quasi-particle measurements with the thicker tip wire are much sharper and have a higher peak maximum, which can directly be seen in the panels a) and b). The voltage corresponding to the switching current of the Josephson measurements in panels c) and d) is reduced and the peak height increased, pointing to a reduced interaction with the electromagnetic environment. This can also be concluded from the much less pronounced resonance  $\omega_0$  that appears to be suppressed by the thicker diameter tip.<sup>3</sup> The  $P(E)$ -functions used for these fits are the ones plotted in figure 3.8, their FWHM-value is  $77.2 \mu\text{eV}$  for tip 1 and  $65.4 \mu\text{eV}$  for tip 2. We used the following parameters for the modeling of tip 1; effective temperature is  $T = 100 \text{ mK}$ , damping factor  $\alpha = 0.75$ , the environmental resistance  $R_{\text{env}} = 376.73 \Omega$  and the resonance energy  $\hbar\omega_0 = 70 \mu\text{eV}$ . The junction capacitance is  $C_{J,1} = 3.5 \text{ fF}$  for tip 1 and  $C_{J,1} = 7 \text{ fF}$  for tip 2.

The parameters for modeling the  $P(E)$ -function are:

$T$	$C_{J,1,2}$	$\alpha$	$R_{\text{env}}$	$Q$	$\hbar\omega_0$
100 mK	3.5 fF, 7 fF	0.75	376.73 $\Omega$	2	70 $\mu\text{eV}$

We find that the convolution with this capacitive noise term will give a broadening that can be approximated with a Gaussian function. The full width half maximum value (FWHM) of this Gaussian is  $\approx 2.24 \cdot \sqrt{2E_C k_B T}$ , for Cooper pair noise. In case of a normal conducting junction the capacitive noise should be reduced to about 50 %, because of the dependence of  $E_C$  on  $Q$ .<sup>4</sup>

This conclusion is illustrated in figure 3.11. By assuming a probable range of capacitance for STM junctions from  $C_J = 1 \text{ fF}$  to  $C_J = 50 \text{ fF}$  and covering temperatures down from the typical liquid helium cooled experiments (below 5 K) we want to give an impression of the expected impact of our result on other experiments. We plot the expected FWHM of the  $P(E)$ -broadening function for the case of a superconducting junction together with the temperature induced smearing of the Fermi-function, where the width is given by  $3.5 k_B T$ . The total broadening is then given by the combination of both terms. At about 1 K the contributions have roughly the same impact, depending on the actual junction capacitance. At lower temperature the capacitive broadening will gain in weight relative to the thermal broadening and will clearly dominate at very low temperature. A simple measure of the relative energy resolution, is given by looking at the voltage at the switching current  $V(I_S)$ .  $I_S$  is the maximal Cooper pair current the Josephson junction can support before it switches into the quasi-particle transport regime. Because of the dissipative tunneling process in the dynamical Coulomb blockade regime  $I_S$

<sup>3</sup>A wire with a length-width ratio close to 1 is not expected to be a good antenna.

<sup>4</sup>The easiest way to include a phenomenological broadening to a quasi-particle spectrum is probably a convolution with a Gaussian of reasonable FWHM, neglecting the asymmetry of the full  $P(E)$ -model. This simple approach can already yield quite good results [Rodrigo04a]

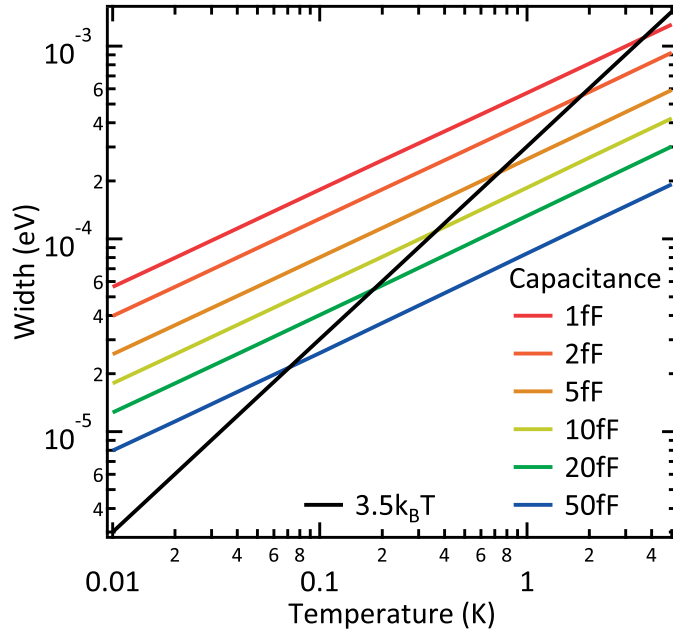


Figure 3.11 – **Comparison of broadening intrinsic to a junction’s capacitance with broadening due to temperature.** To illustrate the impact of the broadening resulting from the interaction of tunneling particles with the environment we plot the expected FWHM value of the  $P(E)$ -function together with broadening due to temperature. For the thermal smearing of the Fermi function we take the standard value  $3.5k_B T$ . To get the junction inherent part we assume a range of capacitance reasonable for the STM. Figure taken from [Ast16].

is reduced, compared to the theoretical maximum. This induces that the switching does not happen at zero voltage, but at a finite voltage  $V(I_S)$ , indicating the amount of back-action on the tunneling particles. After the optimizations during my PhD-work we find this voltage to be about  $V(I_S) = 11 \mu\text{V}$  compared to about  $V(I_S) = 19 \mu\text{V}$  before.

### 3.2.3 The capacitance of the tunnel junction

Determining the actual junction capacitance and even more so the environmental impedance of the STM junction independently is interestingly a non-trivial endeavor on its own. Simple lock-in measurements do not only contain the immediate area of the junction, but also include the capacitance of the wiring as well as tip and sample holder that are not of importance for the tunneling process. Not to mention that the frequency range of the Cooper pair photon emission lies in the GHz range, which is impossible to feed or detect in the current setup of the STM. One approach to get an approximate answer to the magnitude of  $C_J$  is using a simple but analytical model for the tip capacitance. We used the following equation to do so [Ast16]:

$$C_J = \frac{\pi\epsilon_0 d}{\sin(\alpha/2) \ln(\cot(\alpha/4))}, \quad (3.19)$$

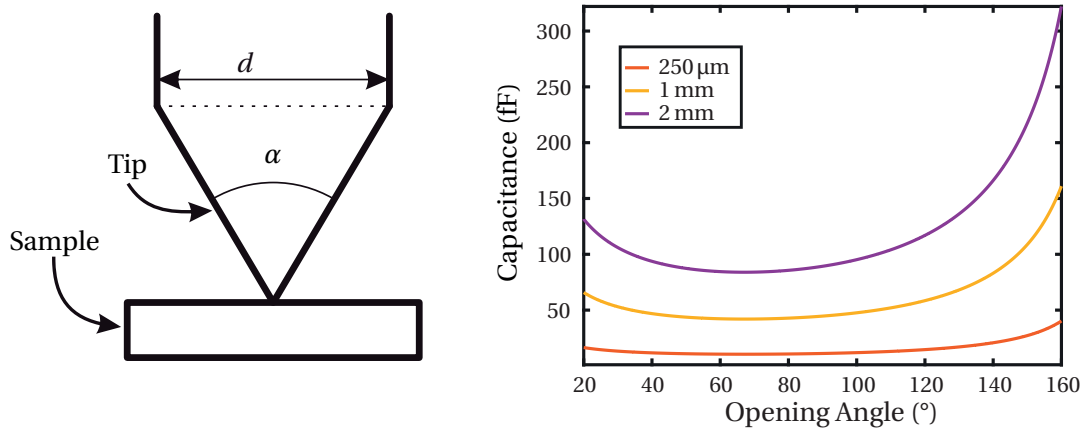


Figure 3.12 – **Simple analytical model to estimate the junction capacitance.** Simple model of tip and sample for estimating the junction capacitance. a) the tip is assumed to be conical and touches the (flat) sample in one point. The diameter  $d$  of the tip wire as well as the opening angle  $\alpha$  are indicated. Figure taken from [Ast16]. b) Relation of  $C_J$  to opening angle  $\alpha$  and tip diameter. Although the model is very simplistic and therefore disregards many details of the real junction the size of  $C_J$  lies within a factor of 10 of the values extracted from the  $P(E)$ -model.

here  $\epsilon_0$  is the vacuum permittivity,  $d$  is the wire diameter and  $\alpha$  is the opening angle of the tip apex. The apex of the tip is placed directly on the sample.

The model and its parameters are visualized on the left side of figure 3.12. How the capacitance depends on the opening angle is plotted on the right side for wire diameters of 0.25 mm in red, 1 mm in yellow and 2 mm in purple. Interestingly the model yields a minimum for  $\alpha \approx 70^\circ$ , the reason for this may be an overestimation of contributions far away from the sample, with a small opening angle the model integrates over a unrealistically long distance until the full diameter is retained. Approaching  $\alpha = 0^\circ$  will give an infinite length. On the other hand a rising  $C_J$  for large  $\alpha$  seems very plausible. An unrealistic aspect of the model that induces an unlikely capacitance at large opening angles is that there is no distance between tip and sample. Both cases would anyway be extreme cases for a real tip, having an opening angle between  $40^\circ$  and  $120^\circ$  seems plausible. The model suggests that  $C_J$  can mainly be influenced by the wire diameter and less so by the opening angle, disregarding extremely flat tips. In comparison to the values we used in our analysis we may underestimate the capacitance, but regarding the simplicity of the model the results still confirm the qualitative order. A quantitatively more meaningful model will have to be much more elaborate.

### 3.3 Conclusions

Operating an STM at low and ultra-low temperatures the tunneling process becomes significantly influenced by the quantum back-action of the electromagnetic environment. In this



regime the granularity in the tunneling and the quantization of charge become non-negligible and have to be regarded in the understanding of acquired data. The most direct observation of this back-action is the dynamical Coulomb blockade in the normal conducting junction. It induces a reduction of the tunneling probability around zero voltage and accordingly yields a dip in the differential conductance. The back-action becomes observable at low temperatures, where the thermal energy  $E_{\text{th}}$  is smaller than the capacitive energy  $E_C$  of the tip sample junction. Its behavior can be modeled in the framework of the  $P(E)$ -theory. For spectroscopic measurements it yields a broadening function that has to be convoluted with a theoretical model to properly reproduce the data. It can be understood as the function describing the energy resolution in scanning tunneling spectroscopy. For the dynamical Coulomb blockade it directly gives the characteristic dip around zero voltage. And in addition, it also models the Josephson effect of a superconducting junction. The parameters of the  $P(E)$ -function are the same in all cases, except for the charge because it depends on the kind of quasi-particle populating the tip and sample. This result highlights the universality of this model for the tunneling process in milli-Kelvin STM.

We detail on a simple possibility to reduce the quantum back-action in the junction. The tip-sample capacitance  $E_C$  and the tips behavior as an antenna appear are the main source for the interaction of tunneling particles with the environment. Using a tip of a larger macroscopic diameter results in a larger  $E_C$  (by increasing the cross section of tip and sample) and also makes the tip a bad antenna, which significantly increases the spectroscopic energy resolution. We conclude that up to a temperature of about 1 K the influence of the environmental back-action can play an important role. At this temperature the thermally induced broadening  $3.5 k_B T$  is of the size of the broadening expected from the  $P(E)$ -model.

**Further analysis of the physical characteristics of mK-STM:** A stronger focus on the physical regime and its peculiarities is beyond the scope of this thesis. For the interested reader we want to point out our publication; *Quantum Brownian Motion at Strong Dissipation Probed by Superconducting Tunnel Junctions*, authored by; Berthold Jäck, Jacob Senkpiel, Markus Etzkorn, Joachim Ankerhold, Christian R. Ast and Klaus Kern, published in Physical Review Letters, 2017. [Jäck17] Here we analyze current biased measurements with a quantum-Smoluchowski equation. We demonstrate that the Josephson junction is an over damped quantum system that behaves as expected from quasi-classical dynamics but with significant corrections because of quantum effects.

Additionally, our following publication may be of interest; *Signatures of phase-coherent transport and the role of quantum fluctuations in the dynamical Coulomb blockade regime*, with the authors; Berthold Jäck, Jacob Senkpiel, Markus Etzkorn, Joachim Ankerhold, Christian R. Ast and Klaus Kern, arXiv:1712.07172 [cond-mat.mes-hall] [Jäck18]. In this work we study the interplay of internal quantum fluctuations and quantum fluctuations with external origin, both related to different Cooper pair transport mechanisms. We find signatures of coherent Cooper pair transport at low voltages and at higher voltages signatures for incoherent transport.



## 4 Transmission channels in atomic contacts

In this chapter we will study the electronic transport properties of the STM junction concerning the channels that participate and how measurements may be influenced by the channel configuration.<sup>1</sup> In break-junction experiments it was found that the number of transmission channels can be traced back to the valence orbitals, by comparing experimental data with computed Andreev reflection spectra [Scheer00]<sup>2</sup>. Orbitals giving a significant contribution to the DOS around  $E_F$ , have to be considered for as possible tunneling channels. This means that depending on the chemical group of the metal at hand only  $s$ - and  $p$ - or additionally also  $d$ -orbitals need to be taken into account with possible constraints due to the junction symmetry [Cuevas98a]. Strong indications were found that the channel configuration is the same in the superconducting and the normal conducting state of a junction [Scheer00]. The junction of choice for the experiments we conducted consists of an Al-tip and a Al(100)-sample with one single atom at both ends. First we will analyze Andreev reflection spectra of the junction to determine the number of participating channels and their transmission, as has been done before. We will demonstrate that the number of significant channels can be reduced from three (corresponding to the valence of Al) to one by STM manipulation of a single Al-atom on the sample surface.

After that the transmission dependence of two physical phenomena, the Josephson effect and the dynamical Coulomb blockade of the single channel junction will be studied. Concerning the Josephson effect we will introduce a model that is non-linear in transmission and includes multiple Cooper pair tunneling. It is based on the full Andreev bound state relation and corresponds very well to the experimental data. At the end of this part of the thesis we will present some early results on how the dynamical Coulomb blockade dip gets smaller with rising transmission in a single channel system.

---

<sup>1</sup>Apart from the electronic transport properties also thermal conduction in atomic contacts is in the focus of recent publications. For instance work on the quantization of thermal transport in single atomic contacts was published in 2017 [Cui17].

<sup>2</sup>Experimental determination of conduction channels in atomic-scale conductors is also possible based on shot noise measurements [Vardimon13].

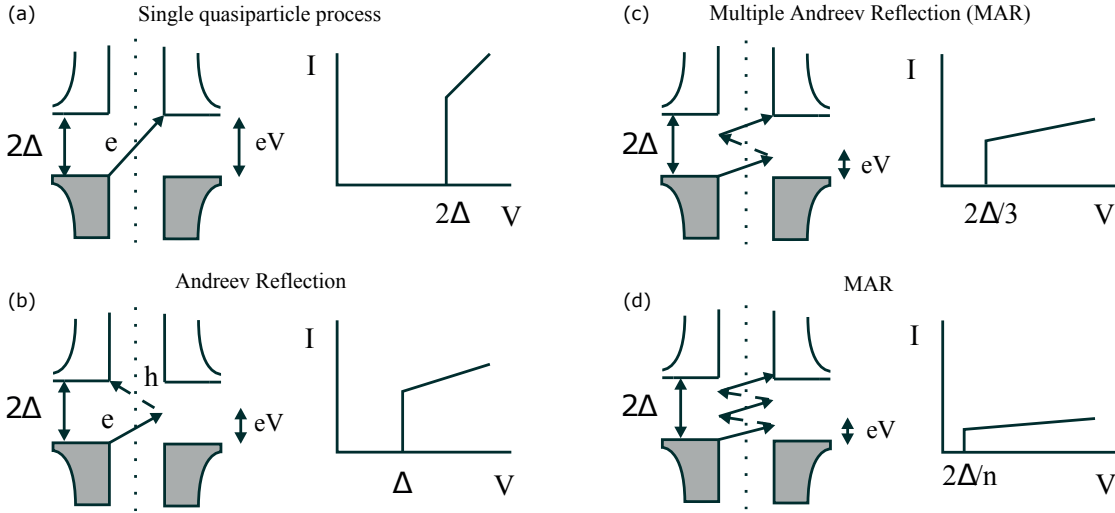


Figure 4.1 – **Illustration of quasiparticle tunneling and (multiple) Andreev reflections in an SIS junction.** On the left side the reflection scheme is depicted and the right side the resulting contributions to the IV-curve is shown. The Bias voltage necessary to enable the tunneling process is marked as  $eV$ . The order of the tunneling process rises from panel a) to panel d). Images taken from [Cuevas99].

## 4.1 Andreev reflections

Let us start with a short description of what Andreev reflections are. An Andreev reflection is one possibility of tunneling between two SC's or an SC and a normal conductor at bias voltages lower than  $\Delta/e$ . As depicted in figure 4.1 tunneling of quasi particles in a tunnel junction of two SC is possible, when the applied bias voltage provides enough energy to split Cooper pairs in both electrodes, in a symmetric junction  $V = 2\Delta/e$ . In an asymmetric junction made of a superconductor and a normal conductor tunneling can occur already at  $V = \Delta/e$ , only one energy gap has to be overcome. In this case, where one electron charge  $e$  is transported from one electrode to the other, also known as quasi-particle tunneling no transport is allowed for energies below the superconducting gap, see figure 4.1 a). An Andreev reflection makes just this possible. In the first order process an electron transverses the barrier but has only half the energy needed to reach the quasi-particle continuum. It can anyway enter the superconductor, if it forms a Cooper pair with another electron at the Fermi level and a hole is reflected, which then enters the quasi-particle continuum of the first electrode, compare figure 4.1 b). Also higher order processes, where multiples  $n$  of  $e$  are transferred and the reflection goes back and forth several times is possible. These multiple Andreev reflection (MAR) are depicted in c) and d). The energies, at which above phenomenon can happen result in steps in the current-voltages curves at  $V \sim 2\Delta/ne$ . At  $n = 1$  tunneling of quasi-particles occurs and dominates the current for  $V \geq 2\Delta/e$ , proportional to the transmission  $\tau$ . Equivalently for  $n = 2, 3, 4, \dots$  Andreev reflections of rising orders generate steps at  $V \sim 2\Delta/ne$  and add current above this voltage proportional to  $\tau^n$ , compare 4.1. The reflection process consists of transporting an electron (hole) from electrode one to the electrode two and transporting a hole (electron) back to the

## 4.2. Modeling transport channels in atomic contacts

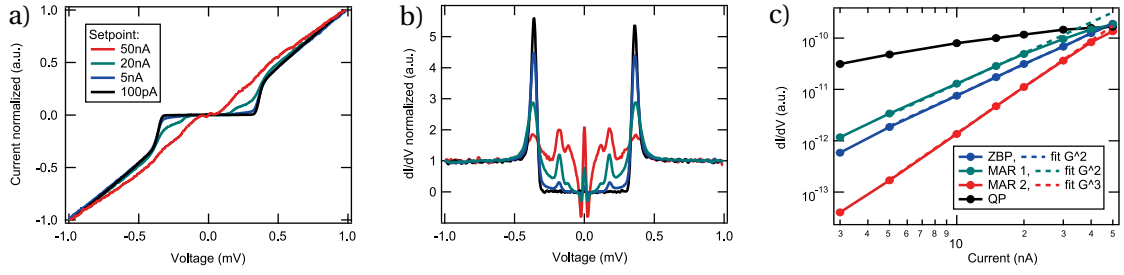


Figure 4.2 – **Experimental observation of Andreev reflections at different junction conductances.** In a) and b) we show normalized  $IV$ -curves and normalized  $dI/dV$ -spectra. The filling of the superconducting gap and the steps/peaks at the voltages corresponding to the order of the Andreev process are visible. In c) the dependence of the maxima of coherence peaks (QP), first (MAR1) and second (MAR2) Andreev reflection and Josephson peak (ZBP) on the conductance is plotted. The ZBP nicely follows a quadratic dependence off  $G$ , as well as MAR1 showing deviations above currents of 20 nA. The second Andreev reflection follows  $G^3$ .

first one. This effectively generates a Cooper pair in the second electrode. In case of  $n$  being odd an additional quasi-particle is transferred to the second electrode. This series of transmission dependent reflections is the origin of the structured filling of the superconducting gap and also an additional current outside of the gap, the excess current.

Experimental observation of Andreev processes were already published in 1963 [Taylor63]. More detailed studies followed later [Blonder82, Octavio83] and also the STM was used to detect Andreev reflections ([Scheer98]) of asymmetric superconducting junctions, with superconducting gaps of different size [Ternes06]. Furthermore, they have been used to observe local variations in the tunneling channels at the point contact limit in STM [Kim15]. We want to show now some of our data to illustrate the filling of the gap by Andreev processes. In figure 4.2 some experimental Andreev reflection spectra are shown. In a) normalized  $IV$ -curves for rising setpoint currents (100 pA to 50 nA), which corresponds to an equally rising conductance are shown. The same data is plotted in b) as differential conductance. In both the data was normalized to 1 at the setpoint conditions to make the gap filling easily observable. A simple analysis of the peak heights in the  $dI/dV$ -data is given in c). The first order Andreev peak (MAR1) grows quadratically with the conductance, as does the Josephson effect. The second one (MAR2) grows with the conductance to the power of 3, as expected from theory. The strong setpoint dependence of Andreev reflections is the key to analyzing the transport channels of a tunnel junction.

## 4.2 Modeling transport channels in atomic contacts

Here one well-established theoretical framework on how to model the Andreev processes shall be described in a manner that introduces some of the main points, but leaves out most of the

details. The following will be a very condensed reproduction of the work of Juan Carlos Cuevas et al. [Cuevas96, Cuevas98a, Cuevas98b, Cuevas99].<sup>3</sup>

To describe the analysis of our data we follow the PhD work of Juan Carlos Cuevas enabling the extraction of number and conduction ratios of channels in an atomic junction yielding the transmission coefficients of each channel of the contact [Cuevas99]. To model the electrical transport in an atomic size junction the current can be split into several independent conduction channels. These channels, with their individual conductance  $G_i = \tau_i \cdot G_0$  add up to the total conductance of the junction,  $G_0$  being the quantum of conductance  $G_0 = 2e^2/h$  and  $\tau_i$  the individual transmission coefficients ranging between 0 and 1. The junction can hereby be characterized by the full set of transmission coefficients  $\{\tau_i\}$ , yielding the so called PIN-code. Based on these the total current through  $N$  channels is given by:

$$I(V) = \sum_{i=1}^N I_i(V, \tau_i). \quad (4.1)$$

The theoretical background to arrive at this conclusion will be described in the following, reproducing the work of J. C. Cuevas [Cuevas99]. The single channel Hamiltonian of a quantum point contact or tunnel junction is given by:

$$\hat{H} = \hat{H}_L + \hat{H}_R + \sum_{\sigma} (\chi c_{L\sigma}^{\dagger} c_{R\sigma} + \chi^* c_{R\sigma}^{\dagger} c_{L\sigma}) - \mu_L \hat{N}_L - \mu_R \hat{N}_R. \quad (4.2)$$

With  $\chi$  being the hopping parameter, and  $\hat{H}_{L,R}$  the BCS-Hamiltonians representing the uncoupled electrodes. The particle number operators are  $N_{L,R}$ ,  $\mu_{L,R}$  and the electrostatic potentials are  $\mu_{L,R}$  and  $c_{L\sigma,R\sigma}$  and  $c_{L\sigma,R\sigma}^{\dagger}$  are the creation and annihilation operators, respectively. The bias voltage is then  $V = \mu_L - \mu_R$ . A gauge transformation yields the time-dependent form:

$$\hat{H}(t) = \hat{H}_L + \hat{H}_R + \sum_{\sigma} (\chi e^{i\phi(t)/2} c_{L\sigma}^{\dagger} c_{R\sigma} + \chi^* e^{i\phi(t)/2} c_{R\sigma}^{\dagger} c_{L\sigma}). \quad (4.3)$$

Here  $t$  is the time and  $\phi(t)$  is the phase difference of the superconducting condensates.

Continuing from here, three different junction types can be described. First some results for the normal conductor-insulator-normal conductor (N-I-N) case and the normal conductor-insulator-superconductor (N-I-S) case will be presented. The reason for this is that these are analytically solvable and basic aspects of the general description can be nicely highlighted here. After that an equation describing the current in the S-I-S junction will be presented, without going into any details, those can easily be looked up in the above mentioned publications and go well beyond the scope of this thesis.

**N-I-N junction:** This case can be solved based on the time-independent Hamiltonian 4.2. With a Green's function formalism the tunneling current can be found.

---

<sup>3</sup>Other ways to model single channel tunneling, which may be equally suitable, e.g. [Averin95], will not be regarded here.

## 4.2. Modeling transport channels in atomic contacts

The current in the normal conducting junction is:

$$I_{NN} = \frac{2e}{h} \int_{-\infty}^{\infty} T(\omega, V) [n_F(\omega, eV) - n_F(\omega)] d\omega. \quad (4.4)$$

With energy  $\omega$  and the transmission coefficient:

$$T(\omega, V) = \frac{4\chi^2 \rho_{LL}(\omega - eV) \rho_{RR}(\omega)}{|1 - \chi^2 g_{LL}(\omega - eV), g_{RR}(\omega)|^2}. \quad (4.5)$$

The electrode properties are included via the Green's functions  $g_{LL}$  and  $g_{RR}$ . In the tunneling limit, where only the first order coupling is regarded this reduces to:

$$T(\omega, V) \sim 4\pi^2 \chi^2 \rho_{LL}(\omega - eV) \rho_{RR}(\omega). \quad (4.6)$$

This expression then gives a tunneling current identical to the description in equation 2.2. Working in the low voltage regime with an ohmic  $IV$ -characteristic,  $T$  becomes a constant, defining the transmission  $\tau$

$$T(\omega, V) \simeq \frac{4\chi^2 \pi^2 \rho^2(E_F)}{(1 + \chi^2 \pi^2 \rho^2(E_F))^2} \equiv \tau. \quad (4.7)$$

$\rho^2(E_F)$  is the density of states at the Fermi level. The transmission can lie between 0 and 1.

**N-I-S junction** Similar to the N-I-N junction also the N-I-S junction can be solved with the time-independent approach.

The current with one superconducting electrode is:

$$I_{NS} = \frac{2e}{h} \int_0^{\infty} \{T_N(\omega) [n_F(\omega - eV) - n_F(\omega)] + 2R(\omega) [n_F(\omega - eV) - n_F(\omega + eV)]\} d\omega. \quad (4.8)$$

With the electron transmission probability:

$$T_N(\omega) = \begin{cases} 0 & \text{if } |\omega| \leq \Delta \\ 2\tau \frac{\alpha(1 - \Delta^2/\omega^2) + (2 - \tau)\sqrt{1 - \Delta^2/\omega^2}}{[\tau + (2 - \tau)\sqrt{1 - \Delta^2/\omega^2}]^2} & \text{if } |\omega| \geq \Delta \end{cases} \quad (4.9)$$

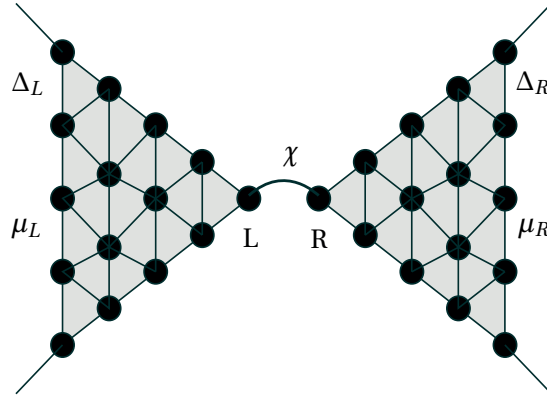


Figure 4.3 – Schematic drawing of the single channel junction in the theoretical model. Images taken from [Cuevas99].

and the Andreev reflection probability:

$$R(\omega) = \begin{cases} \frac{\tau^2}{(2-\alpha)^2 - 4(1-\tau)(\omega/\Delta)^2} & \text{if } |\omega| \leq \Delta, \\ \frac{\tau^2(\Delta/\omega)^2}{[\tau + (2-\alpha)\sqrt{1-\Delta^2/\omega^2}]^2} & \text{if } |\omega| \geq \Delta \end{cases} \quad (4.10)$$

Here  $\tau$  is the normal transmission coefficient. Several important points can be seen in these equations. Tunneling of quasi-particles is only allowed outside of the gap and on the other hand there is an additional tunneling outside of the gap resulting from reflection processes leading to the excess current. For the conductance  $G_{NS}(V) = (2e^2/h)[T_N(V) + 2R(V)]$  follows:

$$G_{NS}(V) = \frac{4e^2}{h} \begin{cases} \frac{\tau^2}{(2-\tau)^2 - 4(1-\tau)((eV)/\Delta)^2}, & \text{if } eV \leq \Delta \\ \frac{\alpha}{\tau + (2-\tau)\sqrt{1-(\Delta/(eV))^2}}, & \text{if } eV \geq \Delta \end{cases} \quad (4.11)$$

which is equivalent to the result found from the scattering approach in the BTK model [Blonder82]. The Andreev processes lead to a transport of Bogolyubov quasi-particles outside of the gap, the excess current:

$$I_{exc} = \frac{e\Delta}{h} \frac{\tau^2}{1-\tau} \left[ 1 - \frac{\tau^2}{2(2-\tau)\sqrt{1-\tau}} \ln \left( \frac{1+\sqrt{1-\tau}}{1-\sqrt{1-\tau}} \right) \right] \quad (4.12)$$

which in the ballistic limit of  $\tau = 1$  becomes  $I_{exc} = 8/3 \cdot (e\Delta)/h$ .

**S-I-S junction** Solving the presented model for two superconducting electrodes is based on the time-dependent Hamiltonian 4.3. For this case only a numerical solution can be derived



## 4.2. Modeling transport channels in atomic contacts

for arbitrary transmissions. In contrast, for the limits of transmission  $\tau = 0$  or  $\tau = 1$  also an analytical solution can be found. The model is developed for a single channel junction a zero temperature which can then be used for a multi-channel system. Due to an explicit time dependence the current can be written as a Fourier series, also describing the Josephson effect in a quantum point contact:

$$I(t) = \sum_{m=-\infty}^{\infty} I_m e^{im\phi(t)}. \quad (4.13)$$

$I_m$  are the Fourier components of the current.

Our analysis will be limited to the DC case ( $m = 0$ ), where the current for an asymmetric superconducting junction is:

$$I_0 = -\frac{2e}{h} \int_{-\infty}^{\infty} \sum_{n=\text{odd}} [\hat{T}_{LR,0n}^r \hat{g}_{RR,nn}^{+-} \hat{T}_{RL,n0}^a \hat{g}_{LL,00}^a + \hat{g}_{RR,00}^r \hat{T}_{RL,0n}^r \hat{g}_{LL,nn}^{+-} \hat{T}_{LR,n0}^a - \hat{g}_{LL,00}^r \hat{T}_{LR,0n}^r \hat{g}_{RR,nn}^{+-} \hat{T}_{RL,n0}^a - \hat{T}_{RL,0n}^r \hat{g}_{LL,nn}^{+-} \hat{T}_{LR,n0}^a \hat{g}_{RR,00}^a]_{11} d\omega, \quad (4.14)$$

which can only be solved numerically for arbitrary transmissions.  $\hat{T}$  are the hopping components and  $\hat{g}$  are the Green functions of the uncoupled electrodes.

More details can be found in the appendix C, of the PhD thesis by Carlos Cuevas.<sup>4</sup> The excess current can be approximated by doubling the result for the N-I-S junction. Restrictions for this model are that the length of the junction constriction has to be much smaller than the coherence length of the SC and that the range of the applied voltage  $V$  has to fulfill:  $eV \sim \Delta$ .

<sup>4</sup>Note that different variables names have been used here, to reach a more consistent picture with the rest of the thesis.

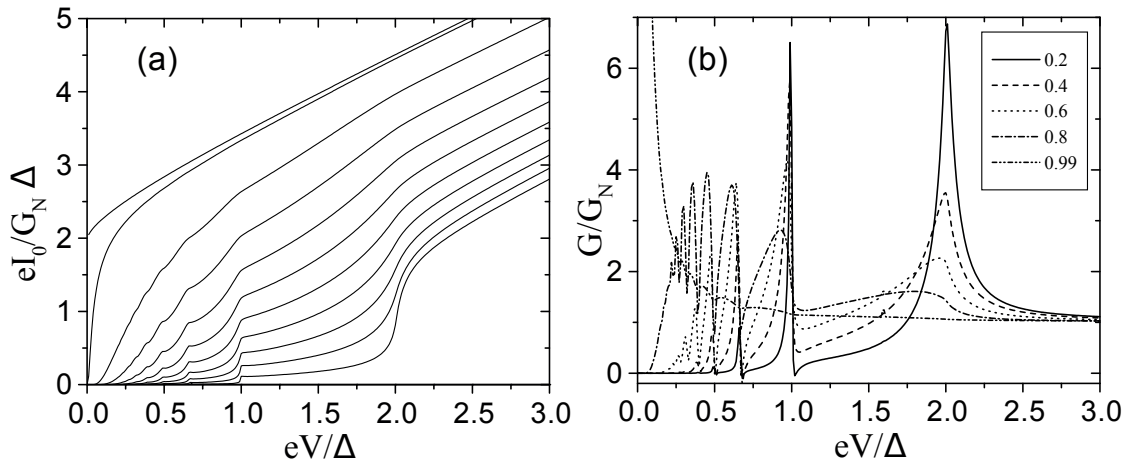


Figure 4.4 – Numerical result for zero temperature of  $IV$ - and  $dI/dV$ -curves for an SIS junction. The transmission in the  $IV$ -curve in (a) changes in steps of 0.1, between 0.1 and 1 (bottom to top), additionally  $\alpha = 0.99$  is shown. The conductance  $G$  is plotted for some example values of  $\alpha$  in (b).  $G_N = (2e^2/h)\alpha$  is the single channel normal conductance. Images taken from [Cuevas99].

Some important aspects of Andreev tunneling are:

- The transport of Andreev reflected particles is bound to one channel and does not change to other channels during the process.
- The transport channels are independent of each other.
- The transport channels are the same in the superconducting and the normal conducting state.
- The transport in a multi channel junction can be analyzed with the model of a single channel junction by summation over the independent channels.

The resulting  $IV$ -curve in an  $N$  channel junction, each with a transmission  $\tau$ , therefore is given by:

$$I(V) = \sum_{i=1}^N I_i(\tau_i, V). \quad (4.15)$$

The numerical results of this model for a range of transmissions is shown as  $IV$ -curves and  $dI/dV$ -curves in figure 4.4. As observable especially in figure 4.4 (b) there are pronounced peaks in the conductance at intermediate transmission rates, which smooth out at high transmissions leaving a single peak around zero voltage in the ballistic limit.

The code J. C. Cuevas developed on the basis of his model described above is the basis for our analysis of the experimental in this chapter. He kindly provided us this code for our analysis.

---

### 4.3. Transport in a single channel Al-STM junction

The code was also used for the analysis of experimental findings, coinciding the publication of the model [Scheer97, Scheer98, Scheer00].

For the sake of completeness we also want to mention the possibility of determining channel transmissions in the normal conducting state relying on shot-noise measurements [Vardimon13]. Furthermore, shot noise analysis can yield information about the spin polarization in single atom contacts [Burtzloff15].

### 4.3 Transport in a single channel Al-STM junction

Probing local variations of the superconducting order parameter on a quantitative level requires an excellent understanding of the current-phase relation of the Josephson effect in the STM to extract the Josephson coupling energy  $E_J$ . To unambiguously connect the local  $E_J$  to variations of the superconducting order parameter  $\Delta$  also the details of the underlying transport processes have to be known. Local changes of the transport channels are likely to emerge at least at distinct structural features, like adatoms or molecules.

In our experiment the junction's constriction is defined by the transport between two single Al atoms. Consequently, we find the number of significant channels reduced from three to one. We are thereby effectively restricting the possible number of available orbital channels by geometrical means and realize a single channel junction as it would be expected for normal s-like metals, e.g. Au or Ag [Levy Yeyati97]. Here lies one of the differences to the groundbreaking work of Elke Scheer et al. [Scheer97], where the calculated junction geometry consists of only one single atom connected to several atoms on each side. In their analysis of transport via one single Al atom three significant transport channels are found, corresponding to the valence of the junction material. A comparable result was found by Vardimon et al using the complementary shot noise analysis, again based on break junction experiments [Vardimon13].

**Treatment of the sample system:** To obtain the above mentioned single atom - single atom junction we prepare the surface of an Al(100) single crystal<sup>5</sup> by means of sputtering and annealing. The preparation procedure follows the work of E. Jona [Jona67]. The annealing temperature in the first cycle is 480 °C where it is kept constant for one hour. In the following cycles the annealing temperature is iteratively reduced down to 435 °C. The sputtering is done with Ar ions accelerated by a 500 eV potential and an emission current of 10 mA, yielding a sputtering current of about 0.3  $\mu$ A. The time per sputtering cycle is one hour.

As tip material we use aluminum wire of high purity (99.9999 %) with 1 mm diameter. Superconducting Al as a tip material has already been used before, for instance by I. Guillamon et al. [Guillamon08]. The tip is prepared by cutting it into shape with a razor blade, sputtering of the oxide layer with Ar ion at 500 eV and field emission on the surface of an Al crystal. The typical parameters for field emission are 42 V and 10  $\mu$ A for about 20 min. We control the current setpoint and the height  $Z$  of the tip with our measurement electronics (Nanonis) to

---

<sup>5</sup>Supplied by: Surface Preparation Laboratory.

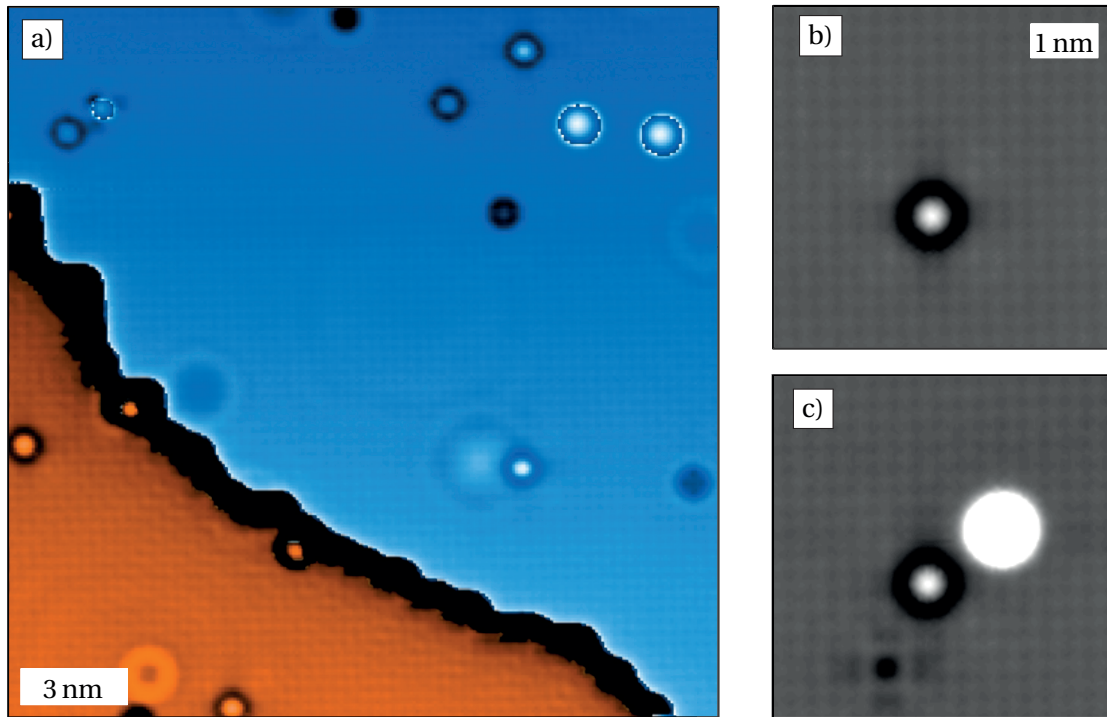


Figure 4.5 – **Typical surface of the Al(100) crystal and extraction of a single atom.** In a) a step edge on the surface of Al(100) is shown, several defects can be seen, together with two Al adatoms on the top right corner. A topography before the extraction of a single Al atom from the surface is shown in b). The pristine surface is shown with an intrinsic defect as a reference for the position and tip shape, for comparison. By approaching and subsequent retraction of the tip to the surface we extract an atom from the lattice (bottom left to defect) and move it on the surface to a hollow position (top right to defect), see c). The color code in b) and c) is the same and ranges from the lowest point (black) to 31 pm. The adatom is saturated in this representation, its apparent height is about 180 pm. The setpoint for all images is  $V = 1.5$  mV and  $I = 1$  nA. Single Al adatoms like this are then used for the transmission dependent Andreev and Josephson measurements.

### 4.3. Transport in a single channel Al-STM junction

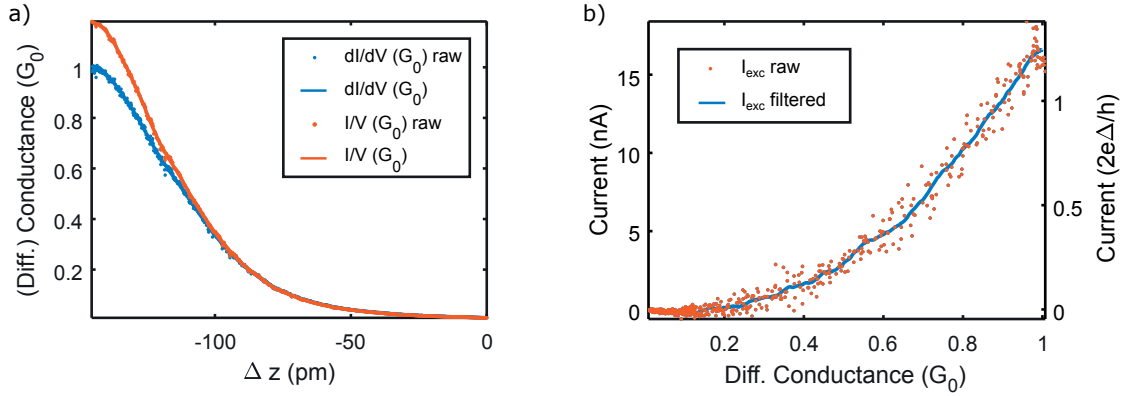


Figure 4.6 – **Approach curve on an aluminum adatom on the surface of Al(100) and extracted excess current**, with a start set point of 1.5 mV and 1 nA. Note that the actual junction voltage decreases with rising current, because of the cable resistances. A clear deviation between conductance ( $G = I/V$ ) and differential conductance ( $dG = dI/dV$ ) is apparent, the  $dG$  curve peaks at about  $G_0$  whereas the  $G$  curve has its maximum at about  $1.2 G_0$ . From this difference one can extract the excess current  $I_{exc}$  at a  $z$ -dependent junction voltage, as shown in b). The filtering was done with a Savitzky-Golay filter.

check the variation of  $Z$  over time to gain a stable tip with changes smaller than the lattice constant. Further preparation of the tip follows standard tip dipping (about hundreds of pm), nano-indentation (about tens of nm) and pulsing until an atomically sharp tip with the desired spectroscopic features is obtained. The goal is to realize a BCS-like superconducting gap with an order parameter as close as possible to the expected value  $180 \mu\text{eV}$  relating to an unperturbed gap.

A topography of the clean Al surface is shown in figure 4.5 a), featuring a step edge in the diagonal direction and several surface defects. Surface defects on Al with a sombrero-like shape (bright dome centered in a dark ring) have previously been associated with oxygen and carbon impurities [Brune92, Brune93]. The single aluminum atom is extracted from the surface by approaching the tip about 400 pm to the pristine surface from a setpoint of 10 mV and 100 pA. One can rationalize that the atom is indeed removed from the sample in two ways, one is that the imaging of the tip does not change, the other is that after this procedure one atom is missing from the surface. The result of this atom manipulation can be seen in figure 4.5 b) and c). An image of the surface is shown before b) and after the extraction from the crystal c). The adatom was also moved away from the extraction location to demonstrate that a surface atom is missing. The surface defect in both images clarifies that the tip did not change, both images are taken at the very same position. An artistic view of the single atom junction is presented in figure 5.1.

To assess the quality of the junction we check that the appearance of the adatom is nicely round and that there are no shadows of the tip, compare figure 4.5 c). Another important test is measuring an  $IZ$ -curve on top of the adatom, which ideally shows a behavior as presented in figure 4.6 (a). Here the differential conductance rises when moving the tip closer and has a

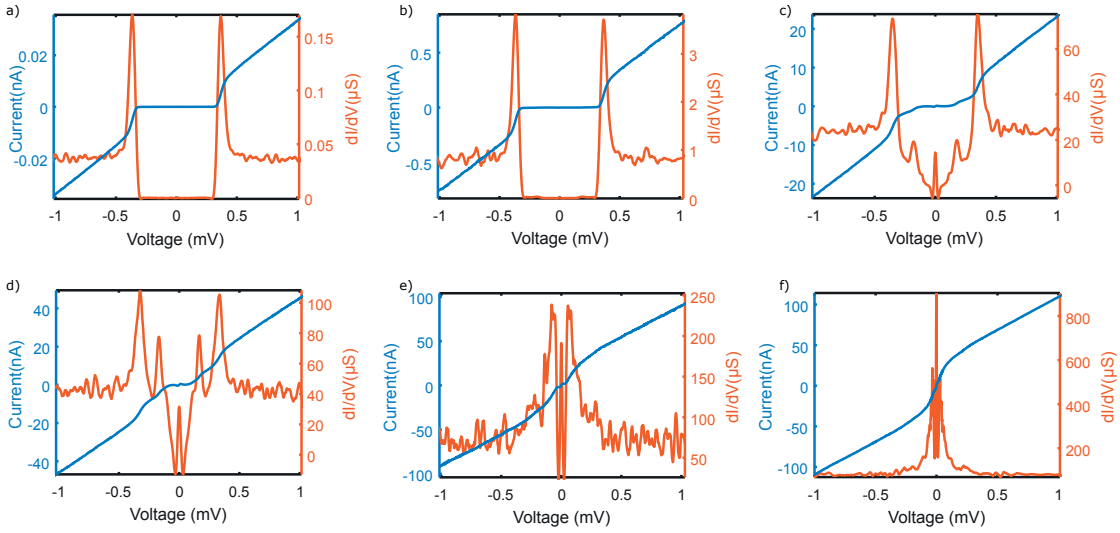


Figure 4.7 – **Andreev reflection spectra from very low to very high transmission.** This series of images shows  $dI/dV$ -spectra numerically derived from the simultaneously plotted  $IV$ -curves. Obviously the quantum of conductance limiting the transport for quasi-particles in the single channel system does not affect the transport of Cooper pairs.

maximum at  $dG \approx G_0$ . Another interesting result from this measurement becomes obvious in the difference between differential conductance  $dG(z) = dI/dV$  and conductance  $G(z) = I/V$ , which stems from the excess current  $I_{exc}$ . Figure 4.6 (b) shows  $I_{exc}$  obtained by subtracting  $dG$  from  $G$  and multiplication with  $V(z)$ . Note that these results are given with a  $z$  dependent voltage  $V$ , because of the voltage drop in the leads that significantly increases with  $I(z)$ . In comparison to the theoretical expectation of  $8/3 \cdot 2e\Delta/h \approx 37.2$  nA only about half is reached at the ballistic limit. A reduced excess current has previously been connected to a reduction of the mean free path in the junction [Kulik00], which may be an explanation for our observation. For a more detailed analysis we are working on calculating the voltage dependent values of  $I_{exc}$ .

After these first measurements on the single adatom we want to further analyze the transport channels, based on the Andreev model described earlier. For this we measure  $IV$ -curves at several conductance values of the curve displayed in figure 4.6. Beginning at about  $0.03 G_0$  we measure the empty superconducting gaps of the Al-vacuum-Al Josephson junction, where, because of the low conductance, neither the Josephson effect, nor the Andreev reflections are visible. The obtained  $IV$ -curve is shown as a blue line in figure 4.7 a), together with the numerically derived  $dI/dV$ -curve in orange. The panels b) to f) display measurements at successively rising conductance. One can clearly see how the gap fills as the Andreev reflections get stronger. Not only the first but also the second order of Andreev reflections can be seen directly, higher order processes are difficult to see, because the width of the peaks is larger than their separation. Furthermore, the spectral weight in the data moves to lower energies as the junction conductance rises, demonstrating how higher order processes get stronger, although they are not separately visible.

### 4.3. Transport in a single channel Al-STM junction

Simultaneously the coherence peaks get smaller and the Andreev reflections increase in height, scaling with the power of the relating reflection order. The rising intensity of the Andreev peaks of higher order  $n$  (multiple Andreev processes) becomes more and more visible at higher conductance, as expected from theory ( $\propto \tau^n$ ). At a conductance close to  $G_0$  the AR-peaks and the Josephson-peak in the  $dI/dV$ -curve merged to one single peak around zero voltage, dropping to the quantum of conductance at a voltage of approximately  $500 \mu\text{V}$ . Theoretically, in a perfect one channel system with  $G = G_0$  and no broadening or dissipation, the  $IV$ -curve would cut the  $I$ -axis at an offset corresponding to the critical Josephson current  $I_c$ ,  $dG(V = 0)$  in this case should be infinite. This may be visualized imagining that more and more steps in the current get closer to zero voltage, adding up, until the maximal current (given by the quantum of conductance and the number of channels) is reached at all points of the voltage range. At infinite order this has to combine to a linear  $IV$ -curve without any steps, except at zero voltage. In the experimental data close to  $G_0$  we find extreme variations of the spectra with only small changes in the junction conductance. It seems questionable, if it is indeed possible to exactly achieve this ballistic limit experimentally in the STM. The separation of tip and sample will always be subject to some fluctuations (however small) and may therefore make it impossible to obtain the right coupling for a long enough time to acquire a measurement.

A comparison of the measured  $IV$ -curves with the fits based on the previously introduced Andreev-reflection model (chapter 4.2) is given in figure 4.8. The data range between  $\pm 70 \mu\text{V}$  was excluded from the fit, because the Josephson effect is not included in the model. Ranging from low conductance and a transmission of  $\tau = 0.09$  in a) up to high transmission of  $\tau = 0.80$  in f) we find a very good agreement between data and theory. The goal for this analysis is to find the number of involved transport channels and their individual transmission. We determine the density of states of tip and sample, as well as the energy broadening by analyzing a  $dI/dV$ -curve at low conductance, where no sign of the Josephson effect or Andreev-reflections is visible, compare figure 4.7 a). All higher transmission  $IV$ -curves are then fitted based on these junction parameters. The results presented here show already a good agreement to the data, the step positions are well reproduced and the overall  $IV$ -dependence is in good agreement. There is a difference in the slope of the steps, possibly related to the fact that the broadening of the  $P(E)$ -model is not included here. In contrast to our usual approach, we analyze the data presented here without using the  $P(E)$ -function to describe the energy resolution, attributed to how the Andreev model was derived. As shown for the standard equation for the tunneling current in the STM, in chapter 3.2.2 the simplification of a symmetric junction (used to derive the Andreev model) cannot be used with the  $P(E)$ -model. In case of the Andreev model this introduces significant complications. An interesting question arising from the multiple tunneling of higher order Andreev processes is, if it results in an increased spectral broadening. A particle that passes the junction several times might also be subject to environmental influences each time it goes from one electrode to the other.<sup>6,7</sup> We use a purely

<sup>6</sup>We are currently working on the implementation of the  $P(E)$ -model with the Andreev-model to obtain a more precise model, in collaboration with Joachim Ankerhold and his group.

<sup>7</sup>Shot noise experiments could associate the quasi-particles involved in Andreev reflections with effective charges larger than the elementary charge  $e$  [Cron01] and even effective charges smaller than  $e$  have been reported for Bogolyubov quasi-particles outside the superconducting gap [Ronen16].



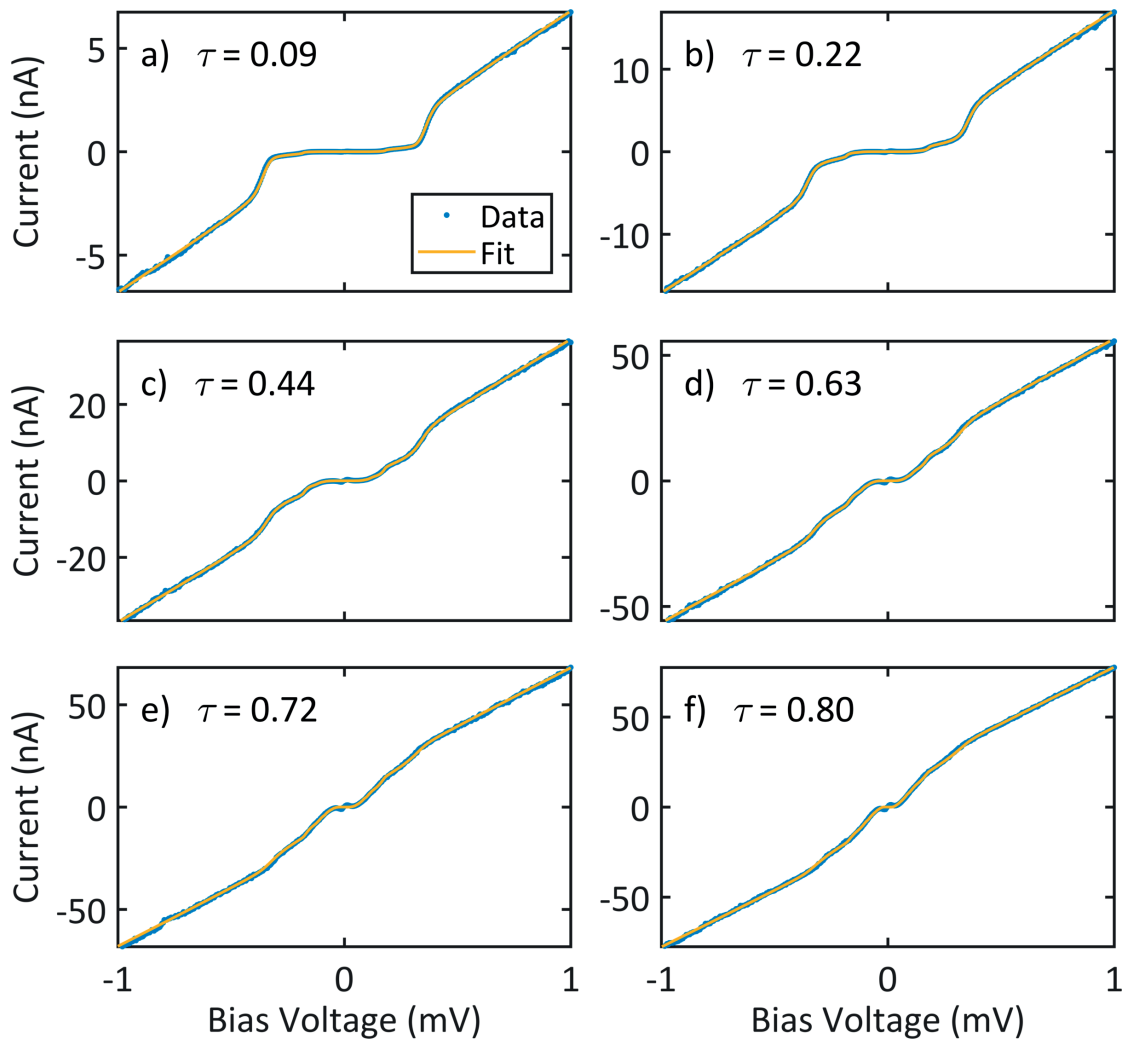


Figure 4.8 – **Andreev fits to experimental  $IV$ -curves on a single Al-atom.** The experimental data is plotted as blue dots and the corresponding fits are shown as orange lines. The panels start at a low transmission of  $\tau = 0.09$  in a) and go up to  $\tau = 0.80$  in f). The region  $\pm 70\mu\text{V}$ , where the Josephson effect is prominent was excluded from the fits.



### 4.3. Transport in a single channel Al-STM junction

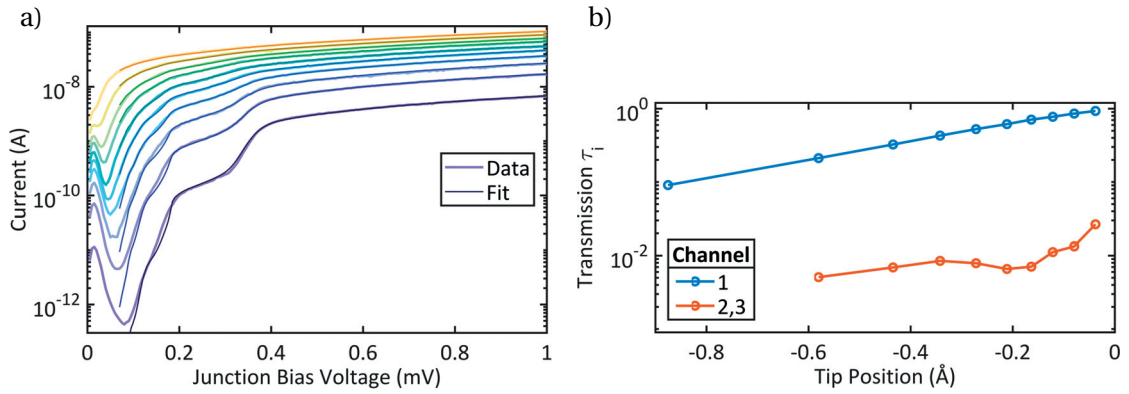


Figure 4.9 – **Spectroscopy on a single adatom on the surface of an Al(100) crystal.** a) shows I-V-spectra over a range of nearly 5 orders of magnitude with a logarithmic current axis, the filling of the gap with Andreev reflection and the Josephson effect can be seen. The corresponding fits are plotted with a slightly thinner line and a darker tone, compared to the corresponding experimental data. Additionally, the fits from the Andreev model are plotted with the data, here the voltage range of  $\pm 70\mu\text{V}$  is excluded. In b) the extracted PIN-code of the transmission channels is plotted versus the tip-sample distance. We set the origin at the position of unity transmission. The transport is strongly dominated by a single channel. Two degenerate channels have a transmission of about or below  $\tau = 0.1$  (the model's precision limit) and may have a transport contribution only at very high conductance.

phenomenological broadening in the Andreev fits based on a convolution with a Gaussian function, applied once to the calculated curve.

The current-voltage characteristics for varied distance between tip and sample is presented again in figure 4.9 a) on a semi-logarithmic scale, to highlight the in gap steps. The tip-sample distance is encoded in the color scale of the plotted data, large distance is indicated by a dark blue (smaller junction conductance) and a small distance is given by a yellow color (larger junction conductance). The fits are displayed as thinner lines in a darker tone on top of the data. The results of the transmission channel analysis is plotted in b). We assume three possible conduction channels, based on the numerous literature results linking the number of channels to the material's valence, which is three for Al. Our analysis shows that two of these channels are degenerate, in the sense that they follow the exact same dependence. Furthermore, they are both strongly suppressed compared to the single main channel. Only when the main channel transmission reaches about  $\tau = 0.9$ , the other channels clearly surpass  $\tau = 0.01$ , the precision limit of the model. This means that they are either below the precision limit of the model or they are two weakly contributing orbitals with similar spatial extend, with respect to the surface orbitals. We can conclude that single channel transmission is characterizing the transport in our junction of two single Al atoms in very good approximation up to a conductance close to  $G_0$ . This demonstrates a pure BCS-like junction of an elemental superconductor with a single channel of conductance that is arbitrarily adjustable for transmissions up to  $\tau = 1$ .

### 4.4 Conclusions

In conclusion, we realized a BCS-like superconducting single channel junction built up from single Al-atoms at tip and sample. We geometrically constrict the transport to one of the three available transport channels of Al. Our analysis of experimental  $IV$ -curves, ranging from the tunneling regime up to a conductance close to  $G_0$ , is based on a well established model of the Andreev reflection structure in the superconducting gap. The good agreement of model and data provided clear evidence for a junction that is strongly dominated by a single channel of conductance. This result is further supported by a measurement of the dependence of the differential conductance  $dG(z)$  and conductance  $G(z)$  on the distance between tip and the adatom on the surface. One observation in this measurement is the maximum in  $dG(z)$  close to the quantum of conductance, indicating a single transport channel with transmission 1. Another outcome is the difference between  $dG(z)$  and  $G(z)$  from which we extracted the excess current. The demonstrated system allows us now to study the transmission dependence of the Josephson effect and the dynamical Coulomb blockade in the single channel limit.

# 5 Effects of single channel transport at high transmission

In the previous chapter we demonstrated a single channel junction in the dynamical Coulomb blockade regime. We now want to understand the consequences these transport conditions have on two physical phenomena. First we will present how the Josephson effect deviates from the picture of many channels with low transmission. Second we study the transmission dependence of the suppression of conductance in the dynamical Coulomb blockade in the normal conducting state of the junction.

## 5.1 Transmission dependence of the Josephson effect

Here we study the deviations between the linear Ambegaokar-Baratoff relation<sup>1</sup> and experimental data in the sequential charge tunneling regime and the limit of a single transport channel. Our data ranges from low tunneling conductance up to the quantum of conductance  $G_0$ , for one dominant channel with transmission  $\tau \approx 1$ . We introduce a theory modeling the Josephson effect based on the full energy-phase relation of the Andreev bound state and find a non-linear behavior with excellent agreement to the experimental data. On top of the non-linearity, transport by multiple Cooper pair tunneling and its interaction with the electromagnetic environment gives a significant contribution at high transmission. An extrapolation of our findings to few channel junctions, which should be typical for nearly all STM experiments, suggests that measurements at intermediate conductance can exhibit deviations to the many channel picture that should be taken into account. We use the same junction constructed by STM manipulation that was introduced in the previous chapter, yielding an aluminum junction with one single atom at the ends of each electrode and exactly known transmission properties. It is shown in an artistic three-dimensional representation in figure 5.1 for low and high transmission  $\tau$ , in a) and b) respectively.

For our analysis of the Josephson effect we use the same data as presented in the channel analysis, but focusing on the voltage range of  $\pm 100 \mu\text{V}$ . In figure 5.2 some of the measured  $IV$ -curves are shown as blue dots, ranging from transmissions of  $\tau = 0.09$  up to  $\tau = 0.80$ . To

---

<sup>1</sup>Where  $E_J \propto \Delta \cdot G$  in the simplest case of a symmetric junction and  $E = E_J \cos(\phi)$ .

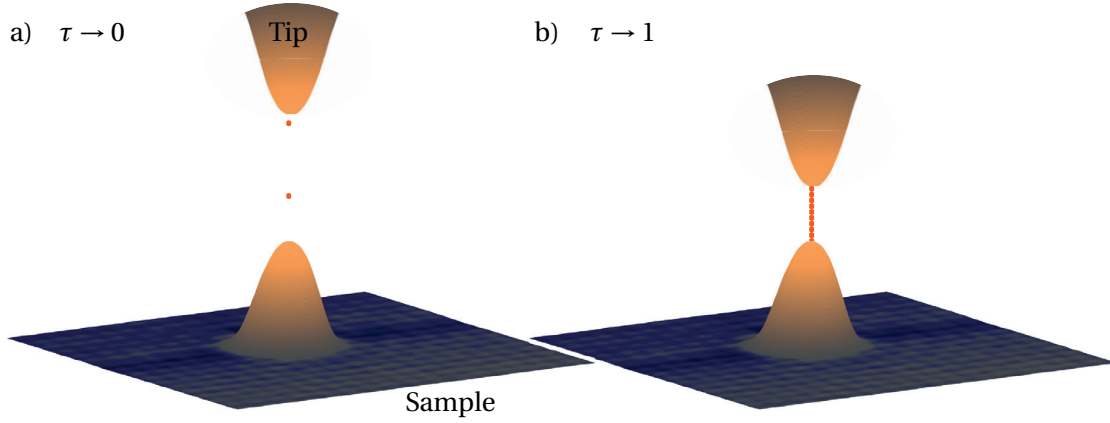


Figure 5.1 – **Illustration of our Josephson junction made of one single Al-atom at the end of each electrode** (tip/sample), constructed with STM manipulation. Due to this arrangement the transport is limited to essentially one channel for the whole range from tunneling to point contact at  $G_0$ . The displayed topography has a size of 5 nm by 5 nm and the adatom an apparent height of about 180 pm.

analyse the data we first use a model for the junction based on the  $P(E)$ -approach introduced in section 3.2.2, equation 3.18. The superconducting order parameters of tip and sample  $\Delta_{t,s}$  are obtained from the fit of a  $dI/dV$ -curve at very low conductance and also used for the Andreev analysis. The  $P(E)$ -parameters ( $C_J$ ,  $T_{eff}$ ,  $Q$ ,  $\omega$ ) of the junction are determined by fitting an  $IV$ -curve with the many channel AB model at low transmission, where the Josephson effect is clearly visible, but Andreev reflections are as low as possible. The transmissions of each curve are obtained from the Andreev-reflection fits from chapter 4.3. The modeling is then done, by taking these independently extracted parameters and calculating the Josephson  $IV$ -curve for each transmission  $\tau$ .

In the STM it is in generally likely that the number of channels is small, it should be approximately the number of valence electrons of the tip apex atom. Working with the STM's few channel junction makes it necessary to adapt the AB-model. The limiting case to study the impact of this restriction is obviously a single channel with a conductance up to  $G_0$ . As demonstrated in the previous chapter we can explore this regime in our STM junction of two single Al atoms. Let us now take a look at the model that was used. The relation of the Josephson energy  $E_J$  and the phase difference of the superconducting order parameters  $\phi$  is given by the energy phase relation:

$$E^\pm(\phi) = \pm\Delta\sqrt{1 - \tau \sin^2\left(\frac{\phi}{2}\right)}, \quad (5.1)$$

which translates, for the assumption of low transmission, to the Ambegaokar-Baratoff relation:

$$E(\phi) = E_J \cos(\phi). \quad (5.2)$$

We derive a model for the Josephson current for just few channels with arbitrary transmission. For this model we start from the current-phase relation 5.1 including higher orders and find significant differences, especially at high conductance. Additionally, it takes into account multiple Cooper pair tunneling. The theory was developed by S. Dambach, B. Kubala and J. Ankerhold in Ulm.<sup>2</sup>

We start with the single channel Andreev bound state energy from equation 5.1, which relates energy  $E$  and phase  $\phi$  and convert it from phase to charge space by Fourier transformation:

$$E^\pm(\phi) = \sum_{m=-\infty}^{\infty} E_m^\pm e^{im\phi}, \quad (5.3)$$

with the Fourier components  $E_m^\pm$  for each possible number  $m$  of transferred Cooper pairs defined as:

$$E_m^\pm = \pm \Delta \sum_{k=|m|}^{+\infty} \binom{\frac{1}{2}}{k} \binom{2k}{k+m} (-1)^{m+k} \left(\frac{\tau}{4}\right)^k. \quad (5.4)$$

Transferring several Cooper pairs in on process will change the energy exchange with the environment. Therefore, the  $P(E)$ -model has to be adapted to get a complete model of the tunneling.

We adapt the  $P(E)$ -function to the multiple tunneling of Cooper pairs to:

$$P_m(E) = \int_{-\infty}^{+\infty} \frac{1}{2\pi\hbar} e^{m^2 J(t) + iEt/\hbar} dt. \quad (5.5)$$

And find the Josephson current as:

$$I^\pm(V) = \mp \frac{4\pi e}{\hbar} \sum_{m=1}^{+\infty} m |E_m^\pm|^2 [P_m(2meV) - P_m(-2meV)]. \quad (5.6)$$

In figure 5.2 the experimental Josephson  $IV$ -curves for some selected conductance values are plotted as blue dots. With rising conductance a large background current, caused by Andreev reflections emerges. As demonstrated in the previous chapter we can model this background and therefore account for it by subtracting the spectral weight it induces from the data. Additionally, plots of the  $P(E)$ -Josephson model as described by equation 3.18 (orange) and the

<sup>2</sup>Institut für Komplexe Quantensysteme and IQST, Universität Ulm, Albert-Einstein-Allee 11, 89069 Ulm, Germany.

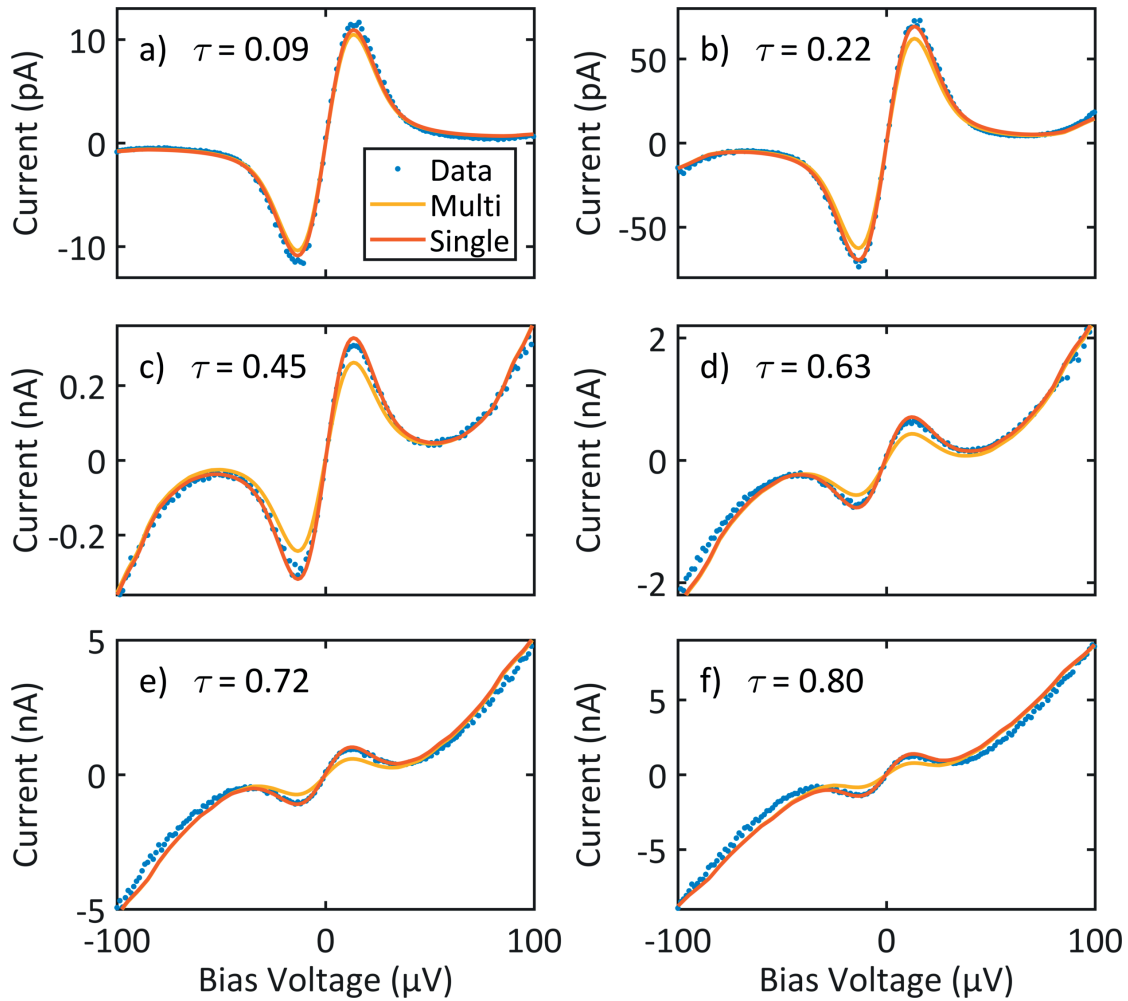


Figure 5.2 – **Single channel Josephson spectra from low to high conductance.** Panels a)-f) display  $IV$ -curves starting at a transmission of  $\tau = 0.09$  and going up to  $\tau = 0.80$ , data as blue dots. Yellow lines show results for the standard second order perturbation analysis 3.18, whereas orange lines depict the results from the extended model 5.6 implementing the full Andreev bound state relation. The standard model show deviations to the data that increase, as the transmission increases. The graphs based on the full Andreev bound state model show good agreement with the data over the complete conductance range. We actually do not fit the data, but use the input from the channel analysis to model it. The used theory was developed by the group of Joachim Ankerhold.

## 5.1. Transmission dependence of the Josephson effect

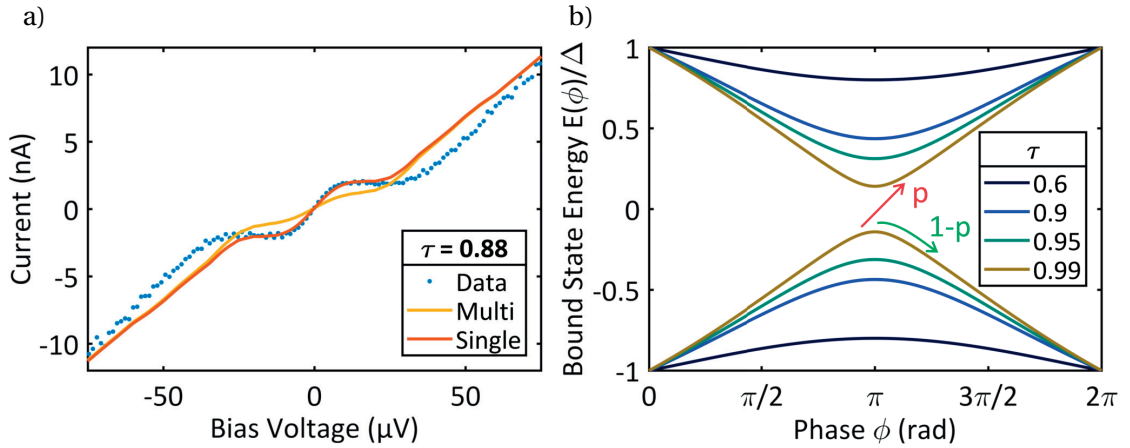


Figure 5.3 – **Limits of the modeling at very high transmission.** In a) a high transmission  $IV$ -curve of the Josephson effect is plotted, where the deviation of the single channel model to the data becomes apparent. At low voltage the model works very satisfactory but fails to reproduce the data above  $\approx 18\mu\text{V}$  at  $\tau = 0.88$ . This deviation can be explained by non-adiabatic processes in the Andreev bound states, which occur dependent on the transmission  $\tau$  above a certain threshold voltage. These processes follow the Landau-Zener probability  $p$ , compare b).

new model with validity from sequential tunneling at low transmissions to tunneling including multiple Cooper pairs at high transmission are shown, compare equation 5.6. Beginning at low transmission ( $\tau \approx 0.09$ ) both models show nearly the same result. With rising  $\tau$  the new model still gives very satisfactory agreement with the data. Clear divergence to the data only emerge at very high transmissions at about  $\tau = 0.80$ . In comparison, the simple second order model produces significant deviations to the data which increase with  $\tau$ . The parameters for modeling the  $P(E)$ -function are:

$T$	$C_J$	$\alpha$	$R_{env}$	$Q$	$\hbar\omega_0$
100 mK	19 fF	0.9	377 $\Omega$	2	80 $\mu\text{eV}$

At very high transmission, above  $\tau = 0.80$  we find deviations between the experimental data and the single channel model. In figure 5.3 a) this difference can be seen for an  $IV$ -curve at  $\tau = 0.88$ . Although the data is nicely reproduced close to zero voltage, the model show some discrepancy for voltages above approximately  $18\mu\text{V}$ . Deviations like this have been previously explained with non-adiabatic processes in the Andreev bound states [Chauvin07], compare figure 5.3 b). The relation of voltage and transmission to the non-adiabatic transition can be calculated with the Landau-Zener probability:

$$p = \exp\left(-\pi(1-\tau)\frac{\Delta}{eV}\right). \quad (5.7)$$

## Chapter 5. Effects of single channel transport at high transmission

---

At a voltage of  $V = (1 - \tau)\Delta$  one can therefore expect that corrections to the single channel model are necessary to model the data. For the example in figure 5.3 a) we find this threshold to be at about  $20 \mu\text{V}$ , in accordance with our observation.

We now want to take a closer look at the differences resulting from the two models. For that we compare the coupling  $E_J(\tau)$  of the many channel AB model, colored in violet, with the coupling parameters of a single channel  $E_m$ , see figure 5.4 a). We include multiple Cooper pair tunneling up to  $m = 3$  in the single channel transport. The coupling for individual CP tunneling  $E_1$  is plotted in blue and shows larger coupling than  $E_J$ . The deviation gets stronger with rising transmission. The multiple processes  $E_{2,3}$  colored in orange and yellow, respectively, give a much smaller coupling but become significant at high  $\tau$ . Close to  $\tau = 1$  the coupling from  $E_2$  is roughly at 25 % of  $E_J$ . Multiple CP transmissions can give a non-negligible current contribution for Josephson junctions that are not characterized by vanishing transmissions per channel. In figure 5.4 b) different few channel systems are compared with the many channel system. We regard coupling deviations for junctions with 1 to 5 equivalent channels.<sup>3</sup> As to be expected, the single channel calculation has the largest deviation to the many channel calculation, more than 15 % at  $\tau = 0.5$ . For more channels the deviations get smaller but stay above 1 % for  $\tau > 0.2$ , and have to be taken into account for a precise quantitative analysis. We have no reason to assume a significant heating of the junction by the high currents, because of the excellent agreement of theory and experimental data.

The impact on typical STM measurements should be rather small, due to the very small transmissions used. Nevertheless, it is important to check if local variations of a quantity, e.g.  $I_c$ , stem from a variation in the transport details rather than from an actual property change of the sample under investigation.

---

<sup>3</sup> This should yield an underestimation of the deviation observed in experiments with atomically sharp electrodes, because of simple geometric considerations. The transmission will most likely be dominated by the fraction of orbitals pointing in the direction of the opposite electrode.



## 5.2. Transmission dependence of the dynamical Coulomb blockade

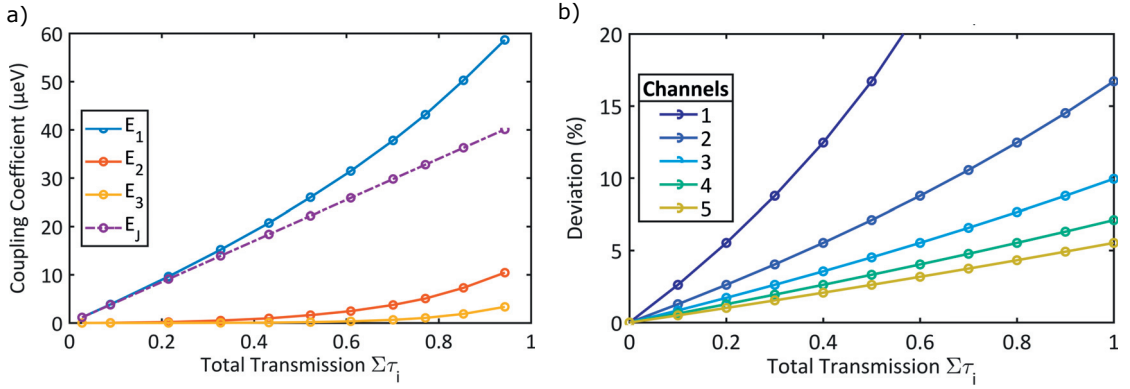


Figure 5.4 – **Theoretical comparison of the many channel and the few channel Josephson tunneling model.** In a) the coupling coefficients  $E_m^\pm$  are plotted for  $m = 1, 2, 3$  (blue, orange, yellow) together with the linear AB behavior (violet). In contrast to the AB-model the coupling changes non-linearly with the transmission. Additionally, the transfer of multiple Cooper pairs becomes important at high transmission. The difference of the Josephson coupling of a many channel junction (AB model) to junctions with one to five channels, each with the same transmission  $\tau_i$  is shown in b). Strong differences can be seen not only at high conductance for the single channel system, but even at  $0.1 G_0$  and five channels at least 0.6 % error can be expected. Because the transmission is likely to be concentrated in the orbitals pointing towards the sample, and not equally distributed, this value is likely to be an underestimation. Theory by the group of Joachim Ankerhold.

## 5.2 Transmission dependence of the dynamical Coulomb blockade

Another intriguing experiment with a precisely tunable single channel junction at hand is testing the behavior of the dynamical Coulomb blockade when the transmission is changed. Theoretical predictions expect the vanishing of the DCB at perfect transmission, similar to the vanishing of shot noise [Levy Yeyati01]. Shot noise  $S$  appears as a result of the quantization of charge with suitable electromagnetic environment and low enough temperatures. It relates to the transmission  $\tau$  as:

$$S = 2eVG_0 \sum \tau_i (1 - \tau_i) \quad (5.8)$$

This problem was already addressed in the PhD work of Ronald Cron [Cron01] shortly after its theoretical formulation, using the break junction technique. More recently Parmentier et al. [Parmentier11] studied the influence of the conductance on the environmental back-action induced DCB conductance dip.

As discussed before in section 4.3 an STM setup has some advantages addressing the controlled realization of tunable single channel junctions with Al electrodes in comparison to the break junction setup. We can construct and test a junction of an Al adatom and sufficiently sharp tip apex that has negligible transport in the second and third channel. The dip in the conductance, due to the DCB can be modeled by the  $P(E)$ -function in the low conductance regime, compare

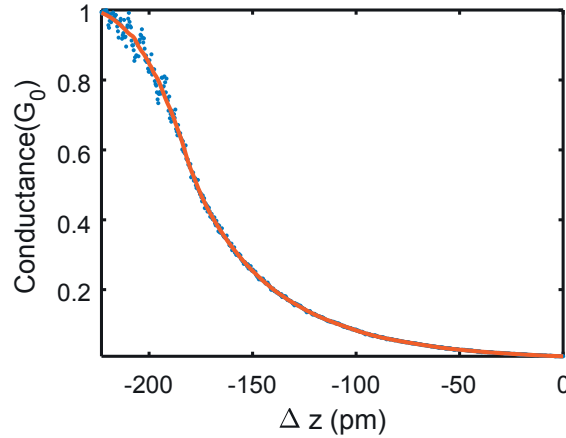


Figure 5.5 – **Approach curve to a single adatom in the normal conducting phase.** The conductance curve reaches  $G_0$  at its peak, as expected for a single channel normal conducting junction. Blue dots show the result based on raw data and the orange line shows the data smoothed with a Savitzky-Golay filter.

3.2.1. In the transmission dependent data presented here this approach is not sufficient to model the effect anymore. A different theoretical description for the conductance reduction has to be employed. We are currently working on the theoretical description of the effect.

To drive our Al electrodes in the normal conducting state we apply a magnetic field of 20 mT. As in the superconducting case we now place a single Al adatom on the crystal surface and first characterize it with an  $I - Z$  curve on the highest point moving the tip closer to the adatom, until we reach a maximum of conductance at about one  $G_0$ . After this approach we retract the tip again and obtain the same behavior as in the previous approach. Additionally, we compare topography before and after to make sure the procedure is non-destructive to the junction. The resulting  $z$ -dependence can be seen in figure 5.5, the conductance data  $G(z)$  is presented in blue dots, whereas the orange line shows  $G(z)$  in a smoothed representation. In comparison to the approach curve with the superconducting junction the missing excess current gets obvious because the conductance curve ( $G(z)$ ) presented here fits on top of the differential conductance ( $dG(z)$ ) in figure 4.6 a).

In figure 5.6 a) measurements of the dynamical Coulomb blockade with a junction conductance ranging between  $0.03 G_0$  and  $1 G_0$  are plotted. The data was acquired by lock-in measurements with a modulation amplitude of  $V_M^{pp} = 20 \mu V$ . Starting at  $0.03 G_0$  a reduction of  $G$  at zero voltage can be seen, the characteristic DCB-dip. The presented data was smoothed with a Savitzky-Golay filter. This dip has a minimum at about 92 % of the surrounding conductance, unaffected by the DCB. With rising junction conductance the dip becomes smaller and is not distinguishable anymore at about  $1 G_0$ . In figure 5.6 b) the reduction of  $G$  at zero voltage is displayed against the junction conductance  $G$ . Because the values are just a readout by hand and not yet from a fit to the data an estimation for the absolute error is  $\pm 1 \%$  for the conductance reduction and a relative error for the setpoint conductance of about  $\pm 1 \%$ . One representative error bar is plotted with the data. Additionally we add a dashed line, indicating

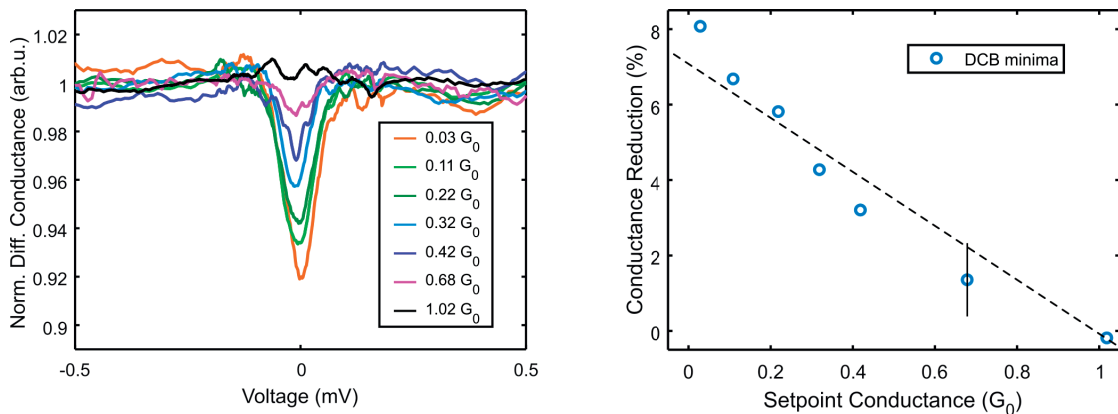


Figure 5.6 – **Conductance dependence of the dynamical Coulomb blockade.** In (a) measurements of the dynamical Coulomb blockade on top of a single Al-atom are compared. Superconductivity is quenched by a magnetic field of 20 mT. We find the depth of the DCB-dip to be decreasing with higher conductance as expected for a single channel system. For  $G_0$  the dip vanishes. From this we can confirm a shot noise like behavior for the DCB in a single channel system. (b) shows the reduction of conductance around zero depending on the junction conductance. We included an error bar representing the estimated error of the very simple analysis. The dashed line is a guide to the eye, indicating a linear dependence.

a linear reduction of the dip as a guide to the eye. The presented data is qualitatively in accordance with the behavior expected for a single channel DCB. The wiggles on the curves are likely stemming from the relatively large current noise in the single atom junction at high conductance, compared to data taken at low conductance on the surface. Another possible explanation for the wiggles are interference effects dependent on the atomic arrangement in the junction, which has been reported before [Levy Yeyati05].

### 5.3 Conclusions

By means of single atom manipulation we realized a tunnel junction between two single atoms on the tip and the sample in our STM. In the superconducting state the junction exhibits an undisturbed, BCS-like density of states, related to the Al electrodes. We demonstrate the strong restriction of the tunneling current to a single channel by modeling experimental  $IV$ -curves with a well-established Andreev reflection analysis for atomic contacts. Additionally, we show the height dependence of the current  $I(z)$  and the differential conductance  $dI/dV(z)$  on top of the adatom. As expected for a single channel the  $dI/dV(z)$ -curve peaks at the quantum of conductance  $G_0$ . By comparison to the calculated conductance  $G(z) = I(z)/V(z)$  we get the excess current  $I_{exc}$  of the Al Josephson junction. We find that it is, in comparison to the theoretical expectation, reduced by a factor of about 2. For now we do not have an answer to why this is, a previously reported reason for finding a reduced value of  $I_{exc}$  is a reduced mean free path in the electrodes.

After proving the single channel junction we used this interesting limit to study the single

## Chapter 5. Effects of single channel transport at high transmission

---

channel Josephson effect. Comparing our data with the many channel and low transmission picture used by Ambegaokar and Baratoff, we find strong deviations which increase with higher transmission  $\tau$ . Then we analyze our data by comparing it with a new model, derived from the full Andreev bound state relation. It shows a non-linear transmission dependence, resulting in an 17 % increased Josephson coupling at a conductance  $0.5 G_0$ , compared to the linear AB model. Furthermore, it includes multiple Cooper pair tunneling, which alone accounts for a quarter of the coupling from the AB model at unity transmission. Compared to our experimental data we find that the new model reproduced the data in great detail up to channel transmissions of  $\tau = 0.8$ . At higher transmissions non-adiabatic Andreev bound state processes gain a significant influence.

To extrapolate the effect of few channel transmission, typical for most STM experiments, we model the coupling for up to five channels with equal transmission. We find that at a conductance of  $0.1 G_0$  deviations between 0.6 % and 2.6 % have to be expected. For a high conductance of  $0.5 G_0$  the deviation can be up to 17 %. This is clearly of importance for the local determination of the superconducting order parameter by Josephson STM (JSTM). Additionally, local variations of the current distribution on the available channels can occur, for instance on adatoms or at step edges. If not accounted for this may give a seemingly varying order parameter, when in truth only the tunneling properties change.

With this single channel system at hand, we additionally take a look at the normal conducting state of the junction, by applying a magnetic field of 20 mT. We can now study how the dynamical Coulomb blockade (DCB) of a single transport channel changes with increasing transmission. This is interesting, because we can test the proposed shot noise like vanishing of the DCB at unity transmission. Indeed we find that the characteristic differential conductance dip around zero voltage gets smaller with larger junction conductance and is indistinguishable from its surroundings close to  $G_0$ . This suggests that the transport becomes more and more protected against the environmental back-action as the transmission increases.

## 6 Pair breaking potentials in a superconductor with two coupled bands

Starting with the experimental discovery of Yu-Shiba-Rusinov-peaks due to Mn and Gd adatoms on Nb [Yazdani97] and the simultaneous theoretical advances on modeling local pair breaking potentials in superconductors [Flatté97b, Salkola97] the idea of probing local perturbations in superconductors by STM emerged. Although there were some important publications in the following years demonstrating Josephson measurements in the STM [Naaman01] the most advances were achieved on the development of theoretical models [Šmakov01, Graham17] and improved YSR-resonance resolution [Hudson01, Ji08]. Going beyond a qualitative analysis of the local superconducting order parameter and getting unambiguous results turned out as a rather involved experimental task. The Josephson effect as a probe in the STM could be especially useful to understand the pairing mechanisms in more complex and unconventional superconductors, possibly by a combination of analyzing quasi-particle spectra and Josephson physics. For instance  $\text{MgB}_2$  a superconductor with multiple gaps [Zhao02, Carabello15] could be an interesting sample. The sample used in our following studies is the superconductor 2H-NbSe<sub>2</sub> doped with 0.5 % Fe as scattering centers.<sup>1</sup>

### 6.1 NbSe<sub>2</sub> basics

2H-NbSe<sub>2</sub>, in the following referenced simply as NbSe<sub>2</sub> is a layered transition metal dichalcogenide showing two dimensional superconductivity [Ugeda15]. It shows a clear charge density wave (CDW) pattern on the surface. The CDW is incommensurate to the top Se layer, with the effect that different regions show various surface appearances. In topographic images the CDW appears in at least three different ways. It either highlights three neighboring Se atoms, only one or separates the surface in darker and brighter triangular shapes. Also a quantum transition from triangular phase to a stripe phase are observable, compare [Soumyanarayanan13, Arguello14]. The critical temperature, below which the CDW appears is  $T_{CDW} \approx 33\text{ K}$  [Moncton75].

Furthermore also the interplay of the CDW and superconductivity is not fully understood

---

<sup>1</sup>The influence of Fe doping on vortex pinning has been studied recently [Pervin17].

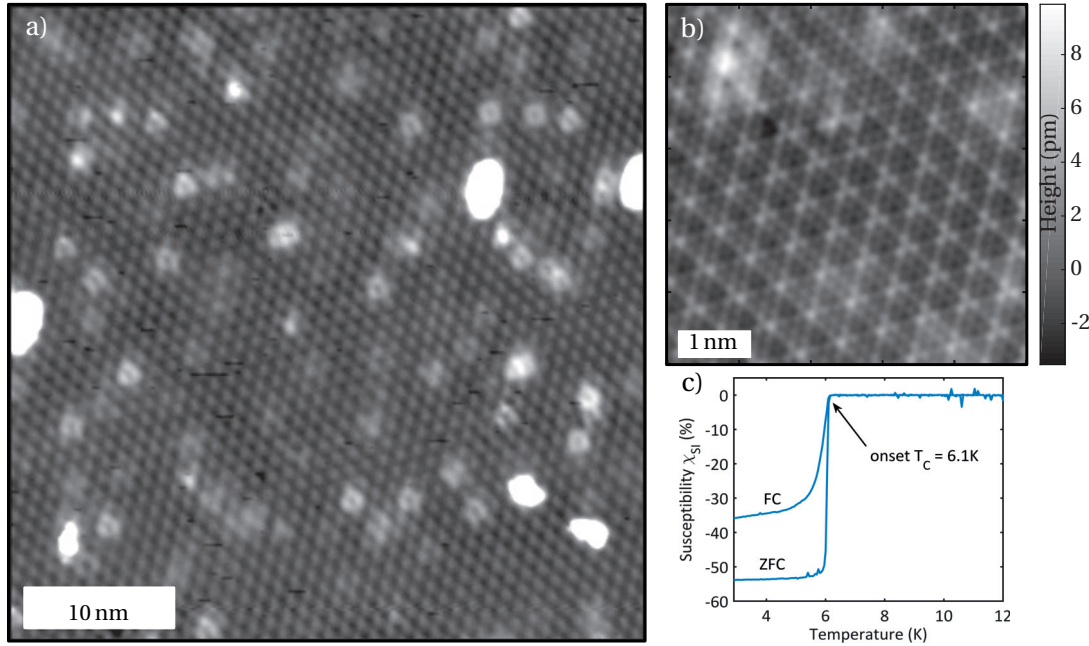


Figure 6.1 – **Topography of Fe doped NbSe<sub>2</sub>**. A large scale image (a) showing the statistical distribution of defects and the charge density wave modulation of the surface, measured at  $V = 100\text{ mV}$ ,  $I = 10\text{ pA}$ . In b) single Se atoms of the top layer are visible as well as the incommensurate CDW altering the appearance. Furthermore, some defects are visible. In c) the temperature dependence of the sample is shown,  $T_c$  is reduced to 6.1 K, compared to the literature value of 7.2 K. Susceptibility measurements with (FC) cooling under magnetic field and without (ZFC) indicate type two superconductivity.

today [Arguello15, Bawden16, Lian17]. The critical temperature of pristine bulk NbSe<sub>2</sub> was reported as  $T_c = 7.2\text{ K}$  [Yokoya01]. Depending on the number of layers this value decreases down to 1.9 K for a monolayer [Staley09, Ugeda15].

NbSe<sub>2</sub> is widely studied for many years already and still regularly under investigation in high impact publications, due to its prototypical behavior and interesting combination of physical effects as well as its relatively easy experimental handling and growth<sup>2</sup> [Xi15, Ugeda15, Arguello15, Silva-Guillén16]. For instance the appearance of vortices under magnetic fields has been studied in STM [Maldonado13]. More directly connected to our work is the observation of long range oscillations of Yu-Shiba-Rusinov resonances [Ménard15] and the coupling of YSR-states [Kezilebieke18] in NbSe<sub>2</sub>. Early Josephson measurements in the STM were already performed on NbSe<sub>2</sub> in 2003 [Naaman03].

In spite of the fact that NbSe<sub>2</sub> is a widely studied superconductor only recently a well working model for the quasi-particle excitation spectrum was reported. After finding that multi-band superconductivity might give a reasonable description of the properties of NbSe<sub>2</sub> by [Yokoya01,

<sup>2</sup>It was recently demonstrated that it can be grown in high quality by chemical vapor deposition [Wang17].



## 6.2. Modeling the quasi-particle spectrum of multi-band superconductors

---

Boaknin03, Rodrigo04b] a very convincing two-gap model was found, moving away from a simple BCS approach. Based on the McMillan equations [McMillan68], Noat et al. modeled the superconducting quasi-particle spectrum of NbSe<sub>2</sub> with two interacting bands, yielding exceptional correspondence to experimental data [Noat10, Noat15].

In figure 6.1 a large scale topography of the sample used in our experiment is shown in a). The CDW is clearly visible, additionally some big clusters are apparent on the surface. A statistical distribution of defects can be seen, which we mainly attribute to the intentional Fe doping. A zoom to some different defects reveals the atomically resolved Se top layer and the incommensurate CDW, highlighting three atoms in the bottom right and only one in the top left. The apparent height of the defects is rather low, barely more than the effect of the CDW. We relate this to the replacement of Nb atom by the Fe, which thereby are subsurface defects covered by a Se layer. We will focus on two kinds of defects on the surface one likely a single Fe defect, with a triangular appearance and another giving a more W-like apparent topography. We surmise that the latter is a double Fe defect. A simple statistics on how often we find both defects supports this assumption. It is reasonable that a random distribution of defects will yield a low number of very close Fe defects, we approximate the ratio of single to double defects with roughly 50:1 in favor of the single defect. To obtain a first impression of the superconducting properties of our sample we analyze its critical temperature  $T_c$ . The temperature dependence of the susceptibility, measured with a MPMS (magnetic properties measurement system) of Quantum Design is shown in panel c). We find that the critical temperature, compared to the literature value of  $T_c = 7.2\text{K}$  is reduced to  $T_c = 6.1\text{K}$ , as a consequence of the doping. From the difference in zero-field cooled to the field cooled curve type-II superconductivity can be inferred.

In the next part we will introduce the theoretical means to model the two band superconductivity of our sample, based on the McMillan model with a Maki-like extension to include the magnetic scattering background.

## 6.2 Modeling the quasi-particle spectrum of multi-band superconductors

As demonstrated by Noat et al. [Noat10, Noat15] the superconducting gap of NbSe<sub>2</sub> can be nicely modeled with the McMillan model, assuming two coupled bands. One superconducting band induces superconductivity in the other via inter-band hopping. This inter-band coupling yields an energy dependence of the superconducting order parameters  $\Delta_{1,2}$  with a non-constant imaginary part. The coupling of the two bands can be understood as a proximity effect in reciprocal space.

In figure 6.2 a) the densities of states of the two bands are plotted separately together with their sum. Here an extension of the McMillan model including a Maki-like magnetic background

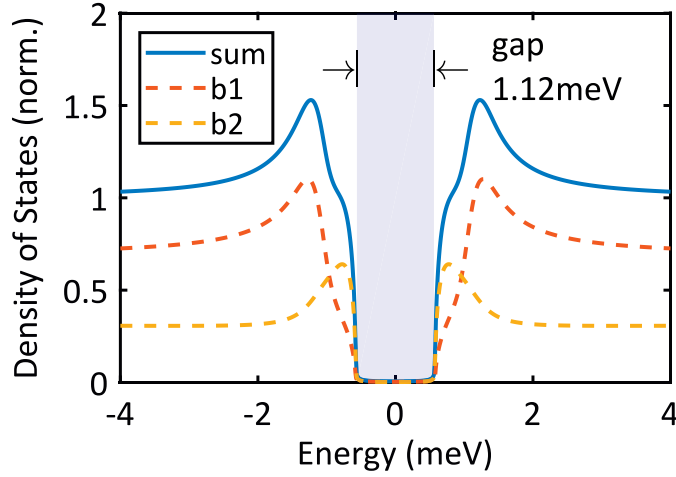


Figure 6.2 – **Quasi-particle spectrum for a multiband-superconductor with magnetic background scattering.** The densities of states of the first and second band are plotted as dashed lines in orange and yellow, respectively. The sum of both is shown as a blue line. A blue shaded area represents the region of the superconducting gap.

scattering is used, we will detail on this later in this chapter. The DOS of the first and second band are displayed in orange and yellow dashed lines, respectively, the blue line represents the total DOS. The gap edge of both bands lies at the same energy, the gap region is highlighted with a blue shaded area. It is apparent that the structure of the total quasi-particle gap is quite different to a single BCS-gap. Its coherence peaks are significantly reduced in height and show a very large width, in the order of 1 mV. In comparison, our experimental data with Al shows a coherence peak width in the order of  $70 \mu\text{V}$ , which includes broadening from the limited energy resolution. Dependent on the value of the tunneling selectivity and the ratio of the densities of states of the two bands the shape of the spectrum changes its appearance.<sup>3</sup>

The energy dependent superconducting order parameters of the two bands given by [McMillan68]:

$$\begin{aligned}\Delta_1(\omega) &= \Delta_1^{\text{BCS}} - \Gamma_{12} \frac{\Delta_1(\omega) - \Delta_2(\omega)}{\sqrt{\Delta_2^2(\omega) - \omega^2}}, \\ \Delta_2(\omega) &= \Delta_2^{\text{BCS}} - \Gamma_{21} \frac{\Delta_1(\omega) - \Delta_2(\omega)}{\sqrt{\Delta_2^2(\omega) - \omega^2}}.\end{aligned}\quad (6.1)$$

$\Gamma_{ij}$  are the hopping parameters between the two bands  $i$  and  $j$ , they obey the relation:

$$\frac{\Gamma_{12}}{\Gamma_{21}} = \frac{\rho_2}{\rho_1} \quad (6.2)$$

<sup>3</sup>An in depth discussion about pristine NbSe<sub>2</sub> and its two-band superconductivity can be found in the publications by Noat et al. [Noat10, Noat15].



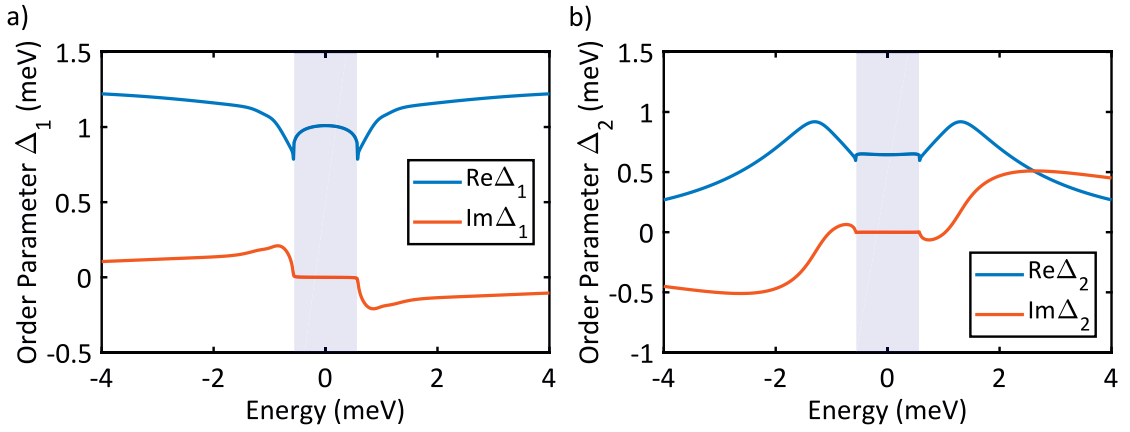


Figure 6.3 – **Order parameters of Fe-doped NbSe<sub>2</sub>** In a) and b) the order parameters of the two bands are plotted separately. The real parts are presented as blue lines and the imaginary part as orange lines. The gap region is highlighted as a blue shaded area.

with the densities of states at the Fermi level  $\rho_i$ .

In figure 6.3 we plot the energy dependence of the superconducting order parameters. The real part of  $\Delta_1$  and  $\Delta_2$  is shown as blue lines in a) and b), respectively. Both show significant variations. Far outside the gap they recover their values they had without inter-band hopping. The gap of band one asymptotically goes to 1.27 meV and the one of band two approaches zero for large energy. The imaginary parts are plotted as orange lines. Inside the gap they are zero, but show strong variations at the energy range of the coherence peaks. One can directly see that the gap-edge size 0.56 meV (compare figure 6.7) is much smaller than the real part of the order parameter. Here we show again results from the extended model including the background scattering resulting in equation 6.3, because it directly relates to the following analysis of our data. The result is quantitatively different from equation 6.1, due to a magnetic scattering background, as demonstrated in figure 2.4, the magnetic background introduces an energy dependence of  $\Delta$  on its own. NbSe<sub>2</sub> is therefore a very interesting material to study.

### 6.3 Fe-doped NbSe<sub>2</sub> probed with a V-tip

Before getting to the actual sample under investigation we want to introduce the probe used to measure the properties of Fe-doped NbSe<sub>2</sub>, the tip. We use superconducting V-wire as tip material, with  $T_c \approx 5.4$  K [Schutter85]. We chose V to determine the junctions  $P(E)$ -function (the inherent broadening) and to be able to perform local Josephson measurement to probe local variations of the superconducting order parameter. The preparation procedure and some basic properties of the used tip are presented in the following. Furthermore, we want to introduce the theoretical model to extend the McMillan approach to include a Maki-like scattering background. We will use this model to account for the Fe-doping, which is strong enough to reduce  $T_c$  by about 1.1 K.

**V-tip preparation:** The vanadium tip used to probe the NbSe<sub>2</sub> sample is prepared on a vanadium crystal. The V(100)-crystal is prepared by standard sputtering and annealing cycles. The annealing temperature starts at 700 °C and is iterated down to 680 °C in the next cycles. For each step the temperature is kept constant for 20 min at the highest point. The sputtering is done with Ar ions accelerated by 1000 V with an emission current of 10 mA, yielding a sputtering current of about 0.9 μA. The time per sputtering cycle is one hour for the first cycle and then reduced to 30 min, 20 min and 10 min, subsequently. The tip material is vanadium wire of 99.98 % purity with 1 mm diameter.<sup>4</sup> It is cut in air and a macroscopic apex is refined with a razor blade. After that it is transferred to the preparation chamber, where it is sputtered with Ar ions accelerated by 1000 V for three times 20 min from three different rotation angles. After this procedure the tip is prepared on the V surface as explained for the Al tip an Al in chapter 4.3. The preparation is continued until the characteristic atomic surface reconstruction of V can be imaged and the superconducting spectrum shows a clear superconducting gap with sufficiently BCS-like appearance and a flat DOS outside of the coherence peaks. A representative spectrum of the prepared tip on the V(100) surface is displayed in figure 6.4 a). The coherence peaks in the differential conductance (orange) are suppressed in comparison to what is expected for a pure BCS-like superconductor. This can be related to the high concentration of impurities in the base material of the wire, resulting in a Maki-broadening, as demonstrated earlier in figure 2.4. On the right side of figure 6.4 the surface reconstruction of V(100) is presented.

For the sample we chose to grow NbSe<sub>2</sub> with a doping of about 0.5 % of Fe to gain local magnetic disturbances in the crystal. One benefit of this approach is having buried defects instead of adatoms deposited on the surface. These subsurface defects introduce only small variations to the apparent topography of the surface. Local changes of the tunneling channels because of the defect are therefore unlikely, in contrast to the scenario of placing adatoms on the surface. As shown in the transport analysis of Al-junctions in the previous chapter, the details of the transmission channels have a significant impact on the detection of physical phenomena, like the Josephson effect. Additionally, the fact that the tunneling to a sample with current contributions from several bands can drastically change the tunneling selectivity to the different bands. The tunneling selectivity to two different superconducting bands has been demonstrated, for instance in the case of Pb adatoms on the surface of Pb(100) [Ruby15a] and also for NbSe<sub>2</sub> [Noat15].

To model the superconducting order parameter of this sample we use the McMillan model for coupled superconducting bands [McMillan68]. Due to the strong effect of the Fe-doping on the critical temperature, the magnetic impurities cannot be neglected. We therefore combine the McMillan model with the Maki model for the macroscopic influence of magnetic disturbances [Maki64, Shiba68].

---

<sup>4</sup>Although being the purest commercially available wire we found, it is significantly less clean than the aluminum wire used in the studies presented in the previous chapter. This has significant broadening effects for the density of states.

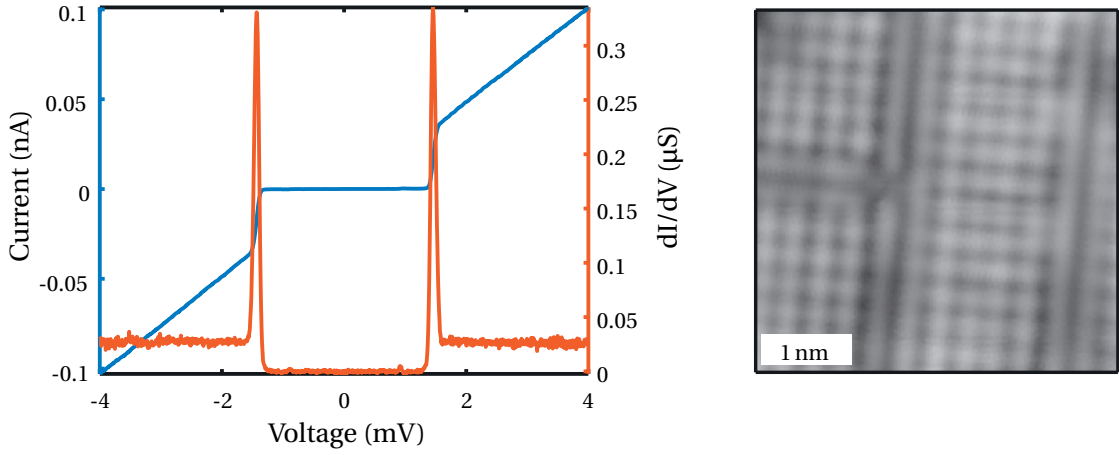


Figure 6.4 –  $dI/dV(V)$ - curve and topography of V(100). On the left side a typical spectrum of the vanadium tip on the V(100) crystal is shown. A topography of the V(100) surface showing the surface reconstruction is given on the right side. Measurement at 1 K,  $T_c \approx 5.4$  K [Schutter85].

We find the two order parameters to be [Zarate85, Golubov97]:

$$\begin{aligned}\Delta_1(\omega) &= \Delta_1^{\text{BCS}} - \Gamma_{12} \frac{\Delta_1(\omega) - \Delta_2(\omega)}{\sqrt{\Delta_2^2(\omega) - \omega^2}} - \zeta_1 \frac{\Delta_1(\omega)}{\sqrt{\Delta_1^2(\omega) - \omega^2}} \\ \Delta_2(\omega) &= \Delta_2^{\text{BCS}} - \Gamma_{21} \frac{\Delta_1(\omega) - \Delta_2(\omega)}{\sqrt{\Delta_2^2(\omega) - \omega^2}} - \zeta_2 \frac{\Delta_2(\omega)}{\sqrt{\Delta_2^2(\omega) - \omega^2}}\end{aligned}\quad (6.3)$$

where  $\zeta_i$  is the coupling of the  $i$ -th band to the magnetic impurity environment. They depend on the ratio of  $\rho_i$  in the same way as the hopping parameters  $\Gamma_{ij}$ :

$$\frac{\zeta_1}{\zeta_2} = \frac{\rho_2}{\rho_1}. \quad (6.4)$$

Equation 6.3 can be solved numerically using the Newton-Raphson method. Causality implies that an energy dependent order parameter is complex-valued [Toll56], which can be seen in figure 6.3.

The normalized densities of states, from our model are:

$$\rho_i(\omega) = \Re \frac{\omega}{\sqrt{\omega^2 - \Delta_i^2(\omega)}}. \quad (6.5)$$

## Chapter 6. Pair breaking potentials in a superconductor with two coupled bands

---

The total normalized DOS can be written in the following form:

$$\rho(\omega) = \frac{1+\eta}{2}\rho_1(\omega) + \frac{1-\eta}{2}\rho_2(\omega). \quad (6.6)$$

The parameter  $\eta$  takes into account the differences of the DOS in the two bands and additionally the selective tunneling to the bands.

In figure 6.5 a) a fit to a differential conductance spectrum measured on the Fe-doped NbSe<sub>2</sub> is shown. The fit is based on the just introduced model. Experimental data is plotted in blue and the fit in orange. We find good agreement between data and model. For the parameters of the McMillan part of the model we find similar values as previously reported [Noat10, Noat15]. The second band is assumed to be normal conducting on its own  $\Delta_2^{\text{BCS}} = 0$  meV and becomes superconducting due to the coupling with the first band with  $\Delta_1^{\text{BCS}} = 1.27$  meV. The difference of the size of  $\Delta_1^{\text{BCS}}$  to the previously reported 1.4 meV is in accordance with the reduction of the critical temperature. For the ratio of the densities of states we find a ratio of  $\frac{\rho_1}{\rho_2} = 5$ . The hopping between the bands is given by the parameter  $\Gamma_{12} = 0.36$  meV and the parameter accounting for DOS differences in the bands and also the tunneling ratio is  $\eta = 0.38$ . We use a coupling to the magnetic environment of  $\zeta_1 = 57$   $\mu$ eV. The resulting energy dependent order parameters  $\Delta_{1,2}(\omega)$  are plotted in figure 6.3.

The parameters used for the extended McMillan model are:

$\Delta_1^{\text{BCS}}$	$\Delta_2^{\text{BCS}}$	$\frac{\rho_1}{\rho_2}$	$\Gamma_{12}$	$\eta$	$\zeta_1$
1.27 meV	0 meV	5	0.36 meV	0.38	57 $\mu$ eV

The parameters that are used to find the junction-characteristic broadening were extracted from the fit to a Josephson measurement, which is shown in figure 6.3 b):

$T_{\text{eff}}$	$C_J$	$\alpha$	$R_{\text{env}}$	$Q$	$\hbar\omega_0$
100 mK	9.5 fF	0.7	377 $\Omega$	2	45 $\mu$ eV

The density of states of the tip is defined with:

$\Delta_{\text{tip}}^{\text{BCS}}$	$\Gamma_{\text{tip}}$	$\zeta_{\text{tip}}$	gap-edge
710 $\mu$ eV	5 $\mu$ eV	33 $\mu$ eV	550 $\mu$ eV

An interesting experiment would be to investigate Andreev reflections on NbSe<sub>2</sub> as done for Al in chapter 4. In principle, it could be possible to extract the precise transport channels and their transmissions between the tip and the two sample baths. By this one would obtain an independent measure of the tunneling ratio.

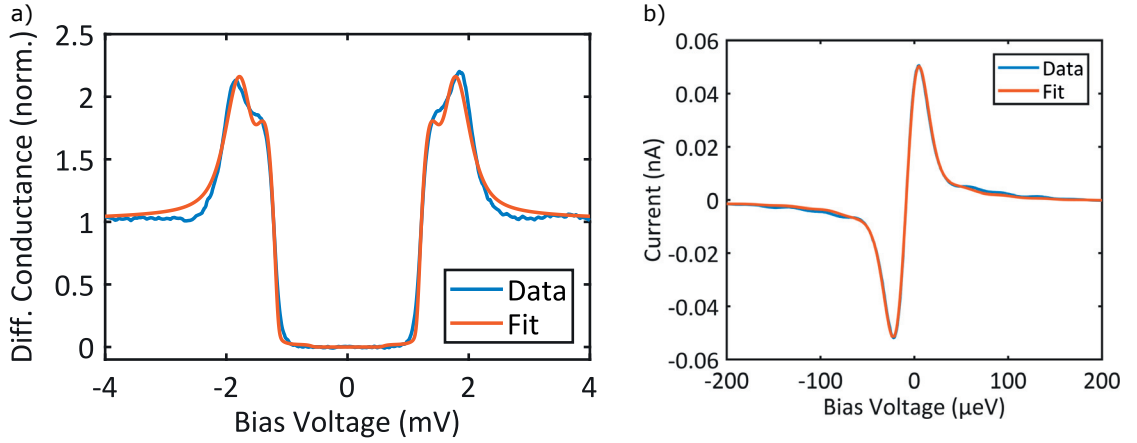


Figure 6.5 – **Fit to the superconducting gap of Fe-doped NbSe<sub>2</sub>** Here we show a quasi-particle  $dI/dV$ -curve without YSR-resonances together with a fit, modeling a background impurity scattering in a). In b) the Josephson  $IV$ -curve from which the  $P(E)$ -parameters of the junction are extracted is plotted together with a fit. The data is plotted as a blue line and the fit as an orange line.

### 6.3.1 Yu-Shiba-Rusinov resonances in a two-band superconductor with complex order parameter

This chapter is based on our manuscript: *Robustness of Yu-Shiba-Rusinov resonances in presence of a complex superconducting order parameter*, with the authors; Jacob Senkpiel<sup>5</sup>, Carmen Rubio Verdú, Markus Etzkorn, Robert Drost, Leslie M. Schoop, Simon Dambach, Björn Kubala, Joachim Ankerhold, Christian R. Ast and Klaus Kern, arXiv:1803.08726.

The interaction of a local pair breaking potential, induced by a defect, with a superconductor can result in a locally reduced superconducting order parameter  $\Delta$  and Yu-Shiba-Rusinov states. We find YSR-resonances that exist not only in the gap but also at the position of the coherence peaks. The YSR-peaks additionally show a strong variation in their width, dependent on their energy position. From a very narrow shape in the gap they significantly increase in width while moving outside of the superconducting gap, on top of the coherence peaks. We can relate this broadening behavior directly to the imaginary part of the superconducting order parameter. Furthermore, we attribute the observed YSR-peak position outside of the gap to the difference between the values of the gap-edge and  $\Delta$ .

To model our experimental data of the YSR-resonances we employ a  $T$ -matrix scattering approach as used by Salkola et al. [Salkola97]. Here the normalized Green's functions  $G_{1,2}(\omega)$

<sup>5</sup>I contributed by handling the experiment, measuring the data, analysing the experimental data, discussing the analysis and the finalization of the manuscript.

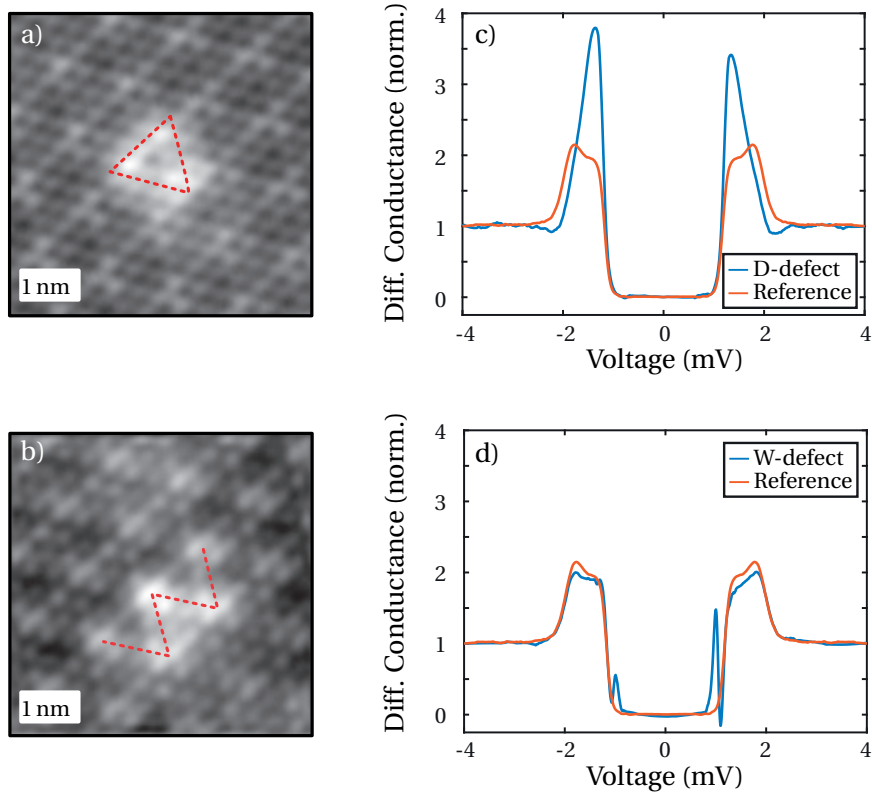


Figure 6.6 – **Typical NbSe<sub>2</sub> defect topography and spectroscopy.** (a) and (b) show topography of the two studied defects,  $\Delta$ -shaped and W-shaped respectively, in our Fe doped NbSe<sub>2</sub> sample. In c) and d) the corresponding  $dI/dV$ -curves are plotted in blue with a reference spectrum of an unperturbed region in orange. The spectroscopy setpoint is: 4 mV and 200 pA. The topography setpoint is: 100 mV and 20 pA.

describe band one:

$$G_1(\omega) = -\pi \frac{1+\eta}{2} \frac{(\omega + i\Gamma)\sigma_0 - \Delta_1(\omega)\sigma_1}{\sqrt{\Delta_1^2(\omega + i\Gamma)^2}} \quad (6.7)$$

and band two:

$$G_2(\omega) = -\pi \frac{1-\eta}{2} \frac{(\omega + i\Gamma)\sigma_0 - \Delta_2(\omega)\sigma_1}{\sqrt{\Delta_2^2(\omega + i\Gamma)^2}} \quad (6.8)$$

of the superconducting substrate.  $\sigma_i$  are the Pauli matrices in Nambu space and  $\sigma_0$  is the identity matrix.  $\Gamma$  is the phenomenological Dynes lifetime broadening parameter.

The T-matrices for implementing the scattering are:

$$T_i(\omega) = V_i(1 - G_i(\omega)V_i)^{-1}, \quad (6.9)$$

with the scattering potential:

$$V_i = J'_i\sigma_0 + U'_i\sigma_3. \quad (6.10)$$

We use an effective, dimensionless exchange coupling:

$$J'_i = \frac{1}{2}JS\rho_i, \quad (6.11)$$

where  $\frac{1}{2}J$  is the classical exchange coupling of one spin and  $\rho_i$  are the densities of states of the respective bands. Furthermore, we use the effective dimensionless Coulomb scattering:

$$U'_i = U\rho_i, \quad (6.12)$$

it is defined over the local Coulomb potential  $U$ . We write the total Green's functions  $G_{1,2}^{YSR}(\omega)$ :

$$G_{1,2}^{YSR}(\omega) = G_{1,2}(\omega) + G_{1,2}(\omega)T_{1,2}(\omega)G_{1,2}(\omega). \quad (6.13)$$

For simplicity, we consider only the total Green's function at the position of the impurity.

Combining the energy dependent order parameters (equation 6.3) with the normalized Green's functions (equations 6.7/6.8) yields the spectral functions:

$$A_{1,2}(\omega) = -\frac{1}{\pi} \text{Tr}(G_{1,2}^{YSR}(\omega)). \quad (6.14)$$

With this the densities of states of the YSR-resonance in a two-band superconductor with a magnetic scattering background can be computed. We use it to find the dependence of the YSR excitation spectra on the exchange coupling.

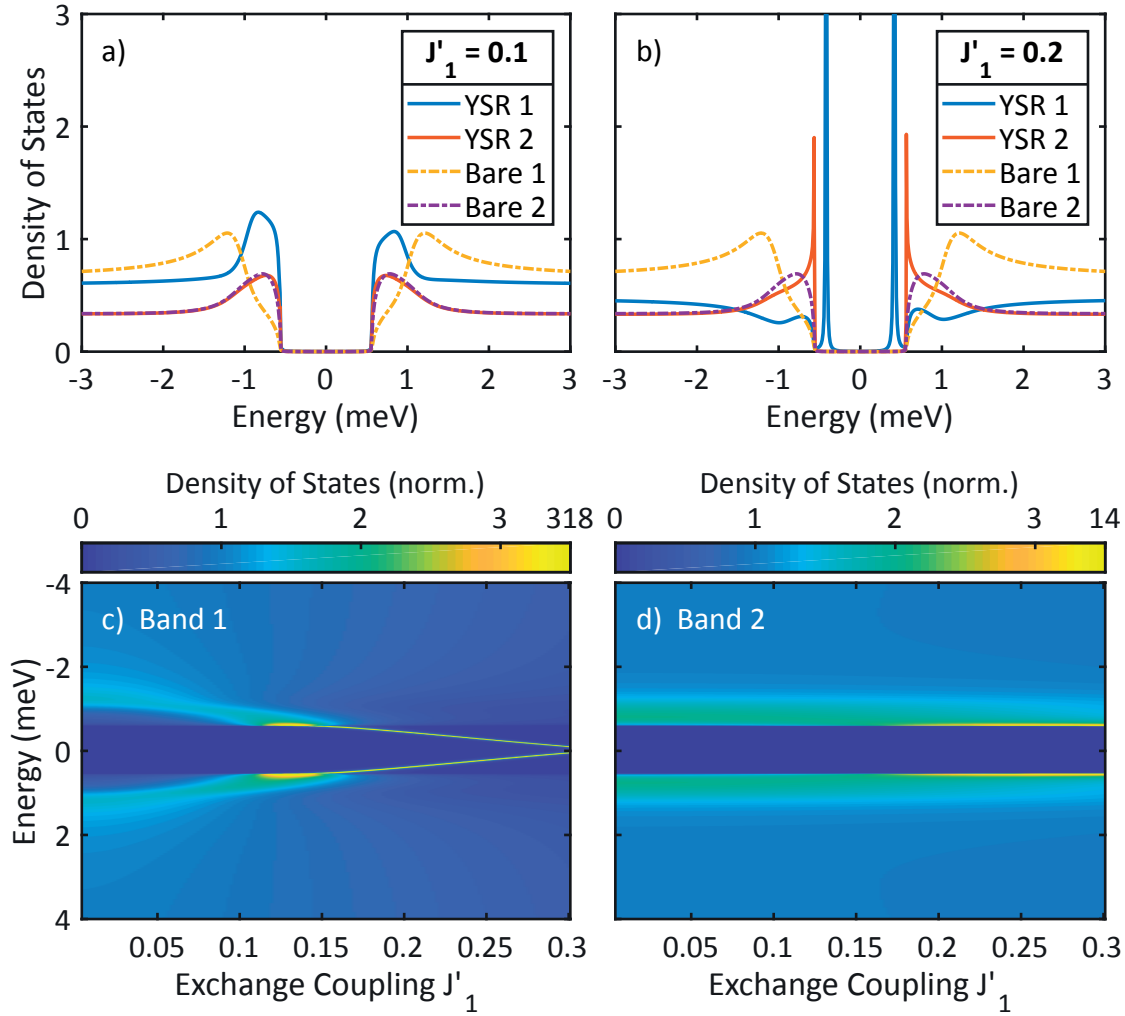


Figure 6.7 – **Calculated YSR-states in NbSe<sub>2</sub>**. Here the YSR density of states are shown for weak (a) and strong (b) exchange coupling  $J$  in comparison to the unperturbed DOS. The dashed lines represent the unperturbed first band in yellow and the second band in violet. The YSR spectra are plotted as solid lines in blue for the first and in orange for the second band. In the weak coupling case the YSR peaks lie in the energy range of the coherence peaks and are comparatively broad (a). For stronger coupling the peaks move inside the gap and get significantly sharper (b). The states in the second band are much weaker than the ones in the first band. The dependence of the spectra on  $J$  is depicted in (c) for the first band and in (d) for the second band. Note the nonlinear color scale above values of 3.5. The asymmetry of the peaks at positive and negative energy is induced by the Coulomb coupling  $U$ .  $J'_1/J'_2 = \rho_1/\rho_2$ ,  $U'_1 = 0.05$  and  $U'_2 = 0.01$



Densities of states generated with this model are shown in figure 6.7 a) and b). YSR-spectra coupled to band 1 are plotted in blue (YSR 1) and those coupling to band 2 are plotted in red (YSR 2). The unperturbed DOS of band 1 (Bare 1) and 2 (Bare 2) are represented by dashed lines in yellow and violet, respectively. Here the ratio  $\eta$  defines the DOS ratio of the two bands in the model. A small Coulomb coupling was included to gain asymmetric YSR-resonances,  $U'_2 = 0.01 = U'_1 n_2 / n_1$ . For small exchange coupling ( $J'_1 = 0.1$ ) the YSR-resonances lie within the coherence peaks, outside of the gap, see a). If the exchange coupling gets stronger ( $J'_1 = 0.2$ ) the resonances move into the gap and get significantly sharper. The ratio of the exchange couplings of the two bands is set to  $J'_1 / J'_2 = \rho_1 / \rho_2$ . A representation of the DOS with continuously changing  $J'_1$  is shown in c) for band 1 and in d) for band 2, note the strongly nonlinear color scale of the DOS above 3.5. In c) the change of the resonance position and peak width with increasing bound state energy is very clear. Outside the gap the resonance yields a rather flat bump in the density of states, upon entering the gap region it becomes extremely narrow and high. The height increases by a factor of approximately 100 in the gap. The peak width inside the gap follows from the Dynes-like parameter  $\Gamma$ . For band two the YSR-resonance shows a qualitatively comparable change, but stays well below the peak heights in a). The YSR-resonances related to the second band apparently are much less pronounced than those from band one. This can be understood from the proportionality of effective exchange coupling between superconductor and impurity and the superconductors DOS,  $J'_1 / J'_2 = \rho_1 / \rho_2 = 5$ . Therefore, we restrict the following analysis to the first band. To compare our experimental data with the results from the model we extract the full width at half maximum (FWHM) and peak position values of the YSR-resonances from both. We choose this simple approach because of the complicated shape of the YSR resonances. Although a full fitting routine would be desirable it would not change the overall outcome of the following analysis.

In figure 6.8 we take a closer look at what we obtain from the calculation. In a) we show the calculated differential conductance spectra from equation 6.14, dependent on  $J'_1$ . Here the junction inherent broadening of spectroscopic features, as detailed in chapter 3.2.2, is included by means of the  $P(E)$ -model. We extracted the parameters for modeling the  $P(E)$ -function from a Josephson  $IV$ -curve, compare figure 6.5. Also the broadening due to measuring with a lock-in technique is considered, a modulation voltage of 20  $\mu\text{V}$  was used with a modulation frequency of 793 Hz. Although the extreme sharpness of the YSR-resonances in the gap is strongly reduced they still appear significantly narrower and higher than the ones outside of the gap. The extracted FWHM-location dependence is plotted as dots in b). The color code of the dots represents the exchange coupling  $J'_1$ . We compare it here with the imaginary part of the superconducting order parameter of the first band, plotting  $|2\Im\Delta_1|$  as a red line, dependent on the peak energy. We find a clear correlation between the two entities.

**Preparation of experimental data:** Because the experimental YSR-spectra usually show a background of coherence peaks, we subtract a reference spectrum from each YSR-spectrum to gain better access to the YSR-peaks. The reference spectrum was measured on a position

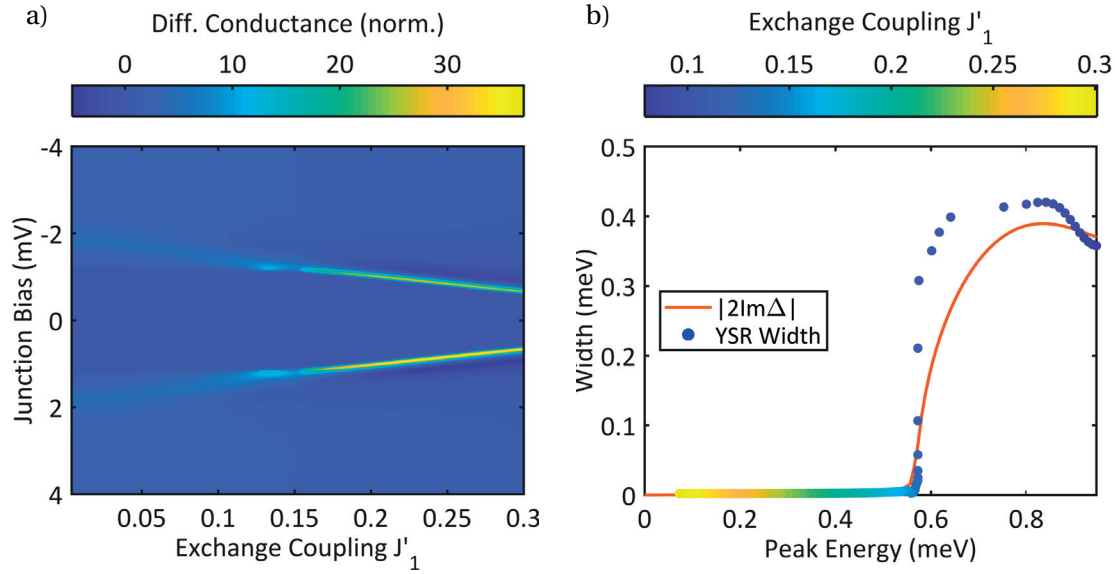


Figure 6.8 – **Theoretical analysis of the relation between peak width and energy position.** In a) we show the simulated  $dI/dV$  signal from the junction, including the tip DOS and the interaction with the environment ( $P(E)$ -model). The width is plotted as dots with the exchange coupling encoded in color, ranging from blue to yellow, in b). For comparison with the energy dependent order parameter of the first band we plot  $|2\text{Im}\Delta|$  additionally as a red line. A clear correlation can be seen.

without topographic disturbances, away from any visible defects, and shows a  $dI/dV$ -curve without signs of YSR-states. Obviously the spectra do not show a pure YSR-resonance spectrum, i.e. without coherence peaks, as expected from theory. The most likely reason for this is that the measurement does not take place at the spatial origin of the scattering process, in contrast to the calculated spectrum. It therefore shows the sum of the unperturbed superconducting gap and the YSR-spectrum. Assuming the Fe dopants replace Nb atoms, they would be covered by the Se top layer. Therefore, a measurement on top of a Fe subsurface defect gives a mixture of a surface gap spectrum and the YSR-spectrum. To minimize the risk of misinterpreting the obtained spectra each are checked for several conditions that have to be fulfilled. These are a minimum in peak height asymmetry, matching peak energy positions and peak FWHM-values of corresponding electron and hole resonances. Furthermore, it is checked if several resonance pairs or other peaks appear in a subtracted spectrum. If so, only the innermost peak pair (at lowest bias voltage) is considered and then checked for an overlap with the next neighboring peaks (at higher bias voltage). If there is an overlap of the peaks, these spectra are only included into the analysis, if the overlap is small enough to have no significant influence on the inner peak. This criterion depends on the ratio of widths, heights and separation of the neighboring peaks. Due to these conditions we can exclude some systematic errors in the analysis.

Two of the resulting spectra included in the analysis, representing the contrasting cases of

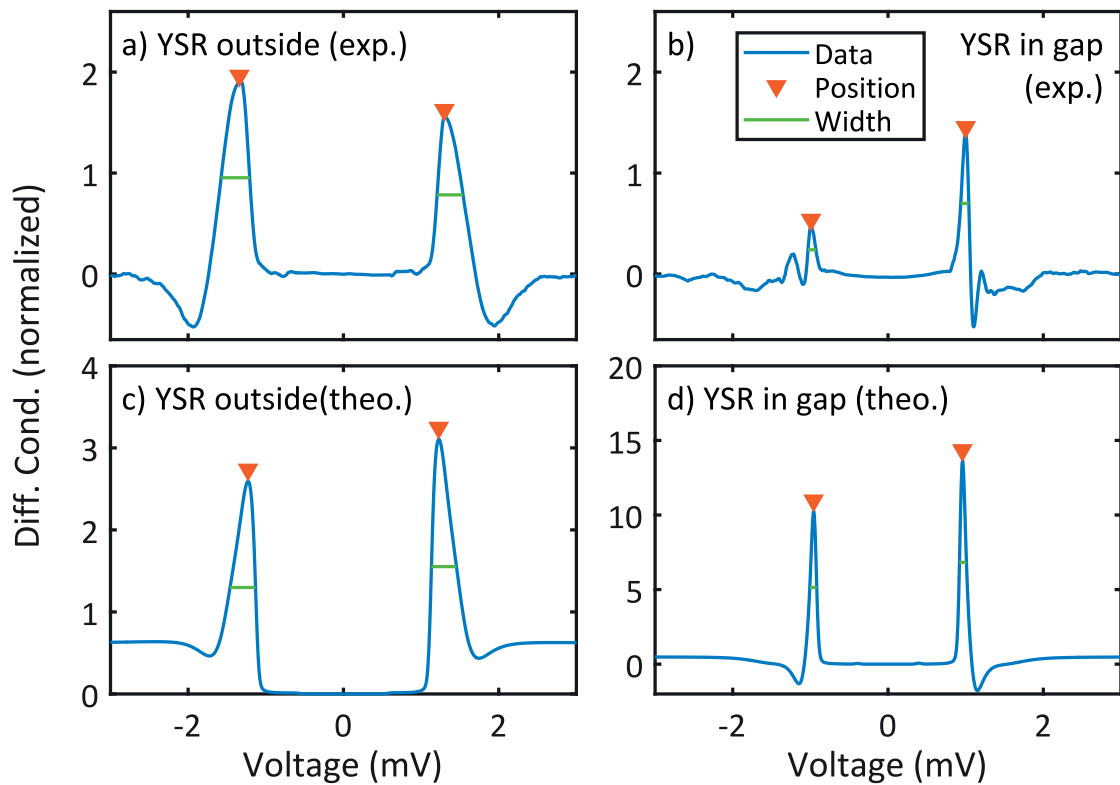


Figure 6.9 – **YSR-peak spectra from experimental data and from the theoretical model.** The experimental spectra are obtained by subtracting an unperturbed spectrum from spectra with YSR-peaks, a) and b). For comparability the data from figure 6.6 is used for this purpose. On the left a) the result for a triangular defect is shown, on the right b) a W-defect is represented. In c) and d) the corresponding modeled spectra are shown. One can clearly see the typical asymmetry of the peaks at positive and negative voltage. Furthermore, the much larger FWHM at smaller binding energy, in the vicinity of the coherence peaks, can be seen.

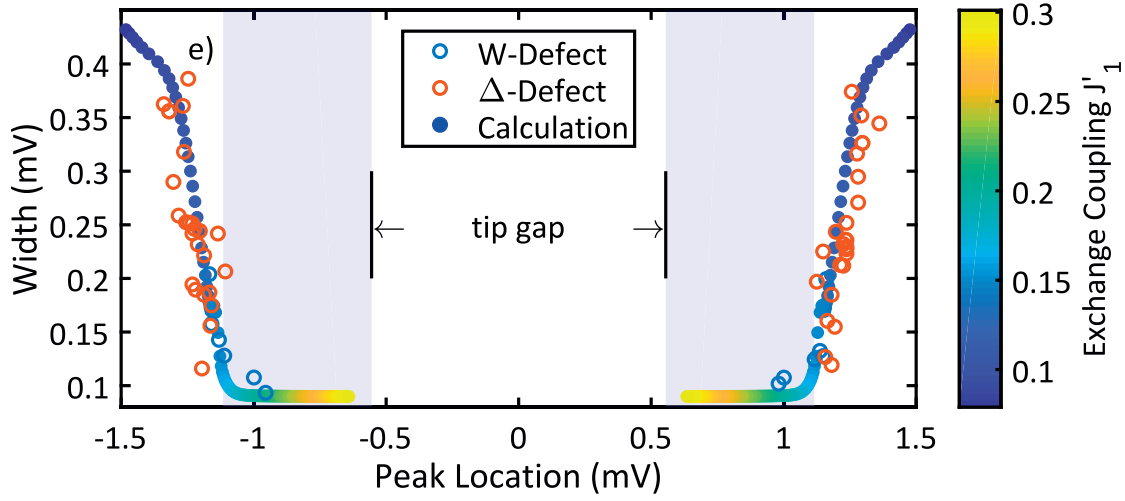


Figure 6.10 – **Comparison of experimental YSR-peak widths with theory.** Experimental peak widths are shown in blue and red for W- and  $\Delta$ -defects, respectively. Widths from the calculated data are dots in a color code representing the exchange coupling  $J'_1$  in band one. The sample gap is shaded in blue. Theoretical and experimental values clearly correlate, confirming the imaginary part of the order parameter as the significant broadening channel.

YSR-states in the gap and of out of the gap, are plotted in figure 6.9 a) and b). In c) and d) representative spectra from the theoretical model are plotted for peak positions corresponding to those in a) and b), respectively. It is obvious that the FWHM of the YSR-resonances are significantly larger if their peak position is at higher energy. This is true for the experimental data, as well as for the theoretical model. A difference in the YSR-spectra extracted from the experimental data and the calculated spectra is that the former goes to zero outside the gap, and the latter does not. This is a result of subtracting a reference spectrum from the measured data. If the YSR-peaks are in the gap, no influence on the analysis is expected, because there are no states in the gap of the reference spectrum. For the other case, with overlapping YSR-resonances and coherence peaks some spectral weight of the YSR-peak is lost, resulting mainly in a reduced peak height. The possible effect on the parameters under investigation is that the width may be underestimated and the position occurs at slightly smaller energy. Additionally, a reduced height of the resonance-peaks in the experiment can be seen. We attribute this to the strong decay of the YSR-wavefunction moving away from the scattering center, compare equation 2.17. Because we are probing subsurface defects, the measurement certainly does not take place at the scattering center. The presented subtracted spectra result from the data shown in figure 6.6. We find that the overall shape and width of the YSR-resonances of our model is in excellent agreement with our experimental observations.

The result of the analysis with all the experimental and calculated differential conductance spectra is presented in figure 6.10. We find excellent agreement between the FWHM-location relation of experiment and theoretical model. This indicates that a strong correlation between

the YSR-resonance width and the order parameter of the superconducting substrate indeed exists. The W-defects appear to have stronger bound states than the  $\Delta$ -defects, this supports the assumption that W-defects are indeed two  $\Delta$ -defects close together, yielding a stronger exchange coupling. Anyway both defects show the same behavior, only for a somewhat different but overlapping range of  $J'_1$ . The relation between imaginary part of the order parameter and YSR-peak width can therefore independently be obtained from studying either defect. Note that the imaginary part should not be confused with the phase of the order parameter. We assume that the distribution of exchange couplings can be traced back to slight variations of the local environment for each defect.

Our analysis establishes that a nontrivial connection between the imaginary part of the order parameters of Fe-doped NbSe<sub>2</sub> and the energy position of YSR-resonances exists. Coinciding YSR-resonances and coherence peaks should not occur as long as the order parameter is energy independent, for example purely BCS-like. If the order parameter  $\Delta$  is energy independent, it defines the position of the gap-edge. Because  $\Delta$  can be larger than the gap-edge already when a magnetic background is disturbing a simple BCS-like superconductor, as shown in figure 2.4, the presented observation of YSR-peaks on top of coherence peaks may actually be a not too exotic case. Possibly, oftentimes observed asymmetries in measurements of superconducting gaps are unresolved YSR-resonances masking the bare shape of the gap. NbSe<sub>2</sub> is an ideal material to demonstrate this effect, because the inter-band coupling of two bands introduces an order parameter with strong energy dependence, resulting in a large difference of gap-edge and  $\Delta$ . This energy-window outside the gap-edge and up to the order parameter is where the imaginary part of  $\Delta$  has its significant variation and YSR-resonances can exist at the same time, yielding a rising broadening of the associated peaks width to higher energy. For other materials where this energy-window is reduced, only YSR-states with very weak binding energy would lie in the area of interest. As shown in figure 6.8 a) the intensity of the resonances becomes hard to distinguish for too low exchange coupling and practically inaccessible by experiment. Depending on the spectral energy resolution of the system they may not be resolvable for different values.

The connection between peak width and order parameter in the theoretical model is that the spectral functions can be understood as single particle excitation spectra, where relaxation into the ground state gives the feature width. The spectral functions are calculated from their respective Green's functions, which are rendered non-Hermetian by their imaginary part, which points towards energy dissipation. In the Fe-NbSe<sub>2</sub> sample, relaxation channels can be related to the inter-band hopping between the two superconducting bands and additionally to the hopping to Fe-impurities. The reducing peak-width from high to low energies indicates that these relaxation channels get less effective, especially after the transition into the gap. In the gap, the YSR-resonances seem to be mostly protected against relaxation [Heinrich13], but not completely. If the order parameter does not get entirely real valued inside the gap, some relaxation channels persist. A possible route to include these in an effective model is an imaginary self-energy, like the phenomenological Dynes broadening parameter. In the presented experiment the intrinsic peak width appears to be masked by the finite spectral energy resolution inherent to tunneling spectroscopy in the STM that follow from capacitive

noise in the junction and was described in chapter 3.2.2.

Another insight from our results is that YSR-resonances can be used to probe the imaginary part of a complex-valued superconducting order parameter. This approach may help to select less or more protective environments for quantum-systems with long lifetimes. The realization of exotic effects, like Majorana bound states [Das12, Nadj-Perge14, Ruby17] in other material systems could benefit from lifetime studies. It can also be useful to better understand the nature of the underlying superconducting materials. The imaginary part of the order parameter, probed on the local scale could give valuable insights to the phenomena driving non-trivial superconductivity, for instance with unconventional pairing, with a topological nature or induced by proximity.

### 6.3.2 Josephson effect in multi-band superconductors

A promising means to evolve the understanding of superconductivity is to map the superconducting order parameter  $\Delta$  on the atomic level. Doing so can help shed light on the details of the interactions between superconductivity and local perturbations, which typically reduce  $\Delta$ . To capture these local variations, the standard STM spectroscopy giving quasi-particle spectra is not sufficient. As demonstrated in chapter 2.2, as soon as superconductivity is perturbed (also for non BCS-like superconductivity) the order parameter cannot be unambiguously extracted from the coherence peak separation, compare figure 2.4. Additionally, YSR-resonances likely stemming from the same local perturbation that affects  $\Delta$  can significantly alter the spectrum. The relation between the gap and order parameter is trivial only in the simplest cases, where no interaction between magnetism and superconductivity occurs. To circumvent this problem the Josephson effect can be used.

Early experimental detection of Josephson tunneling in the STM was achieved by O. Naaman, W. Teizer and R.C. Dynes [Naaman01] in 2001, together with important theoretical work by J. Šmakov, I. Martin and A. V. Balatsky [Šmakov01]. The idea to realize Josephson experiments in the STM (JSTM) manifested already some years earlier [Franz96, Pan98].<sup>6</sup> In most STM experiments the thermal energy  $E_{\text{th}}$  is larger than Josephson coupling energy  $E_J$  resulting in thermally induced phase fluctuations and thereby a reduced supported supercurrent  $I_s < I_c$ . For this high temperature limit of Josephson physics the Ivanchenko-Zil'berman model [Ivanchenko69] was employed. Measurements at milli-Kelvin (mK) temperatures have been realized in 2004 by J.G. Rodrigo, H. Suderow and S. Vieira demonstrating a significant reduction of phase fluctuations [Rodrigo04b]. They additionally point out the importance of exactly determining the spectroscopic energy resolution of the system to extract physical properties on a relevant quality in mK-STM experiments.

In the mK-regime the charging energy dominates the Josephson effect and it can be analyzed based on the  $P(E)$ -approach, as established for the STM by B. Jäck et al. [Jäck15a, Jäck15b].<sup>7</sup>

---

<sup>6</sup>Other reported observations of the Josephson effect in the STM: [Naaman03, Naaman04, Proslie06, Rodrigo04b, Rodrigo06, Kimura08, Kimura09]. Microwave assisted tunneling in the STM: [Roychowdhury15].

<sup>7</sup>Employing the  $P(E)$ -model for STM-experiments was followed up by [Randeria16].



At least in the simplest case the Josephson critical current is directly dependent on only the superconducting order parameter and the normal state conductance  $G_N(E_F)$  of the junction, see equation 2.22. This equation obviously holds only for a symmetric junction, where  $\Delta$  of the tip and  $\Delta$  of the sample are the same. Therefore a different relation is needed to probe variations in the sample.

The form of the Ambegaokar-Baratoff relation for an asymmetric junction, derived for zero temperature has to be used [Ambegaokar63]:

$$I_c = 2 \frac{G_N}{e} \frac{|\Delta_s \Delta_t|}{|\Delta_s| + |\Delta_t|} \cdot K\left(\frac{|\Delta_s - \Delta_t|}{|\Delta_s| + |\Delta_t|}\right), \quad (6.15)$$

$G_N$  is the normal state conductance at Fermi energy.

$K(m)$  is the complete elliptic integral of the first kind<sup>8</sup> [Ambegaokar63].

The idea of JSTM is to use this relation to locally measure the Josephson effect with a superconducting tip of known order parameter  $\Delta_t$ . Then, based on an applicable theory (here the  $P(E)$ -model) for the modeling of the Josephson  $IV$ -curve the critical current  $I_c$  can be extracted. Once  $I_c$  is obtained the superconducting order parameter of a sample  $\Delta_s$  is given by the AB-relation, equation 6.15. The experimental realization of this, however, is not straightforward. There are several important questions to answer before quantitative and unambiguous results can be obtained. For instance, the normal state conductivity  $G_N(E_F)$  at Fermi energy is not directly accessible in the superconducting state. Although it may be extrapolated from the conductance in the superconducting phase, from far outside of the gap, it will be an approximation and prone to errors. Therefore, great care has to be taken to determine the value of  $G_N(E_F)$ . Note also that in the superconducting state the differential conductance is needed. The conductance  $G = I/V$  would include the excess current  $I_{exc}$ , as demonstrated in chapter 4.

To get a first impression on the connection between the observation of YSR-resonances and the reduction of the superconducting order parameter  $\Delta$  we plot YSR-spectra and corresponding Josephson measurements in figure 6.11. In a) we show some  $dI/dV$ -curves around a Fe-defect in our NbSe<sub>2</sub> sample. The dependence of the YSR-resonance intensity on the lateral distance from the impurity position is plotted, it clearly reduces while moving away from the center. Corresponding  $IV$ -curves of the Josephson effect are plotted in b). Here an inverse correlation of peak to distance can be seen, at the defect the effect is reduced and recovers while moving away from it. The current next to the Josephson peak at zero voltage shows a small peak from the antenna resonance at about 70  $\mu$ V, compare chapter 3. All three curves go to a very small and nearly identical value at 100  $\mu$ V, this clearly excludes a changing quasi-particle-background as the source for the different peak heights. The Josephson measurements and

<sup>8</sup>Here used with the argument  $m = k^2$ , which is the standard in both Mathematica and Matlab today as compared to the usage by Ambegaokar and Baratoff

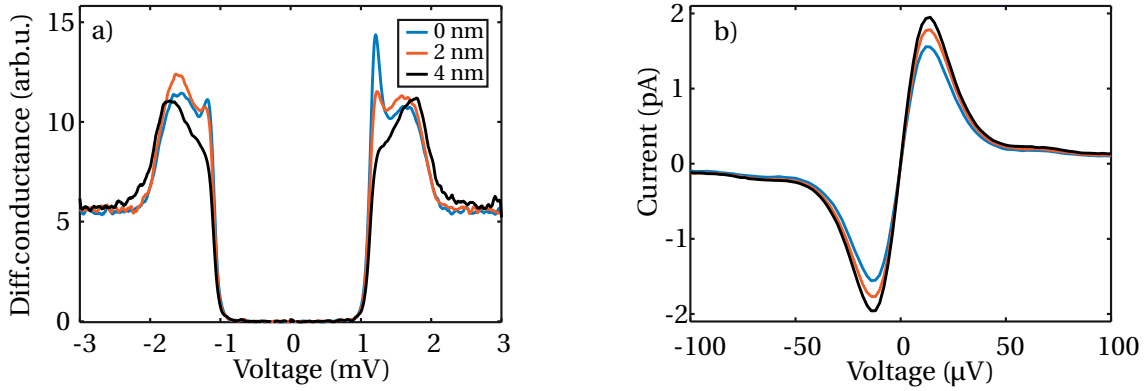


Figure 6.11 – **Correlation of YSR quasi-particle and Josephson spectroscopy.** a) presents how the YSR-peak intensity depends on the lateral distance to a defect (distance increasing with number by 2 nm). In b) the corresponding Josephson spectra are plotted, demonstrating a correlation of YSR-resonance and suppression of the Josephson effect.

the reduction in the switching current  $I_S$  are therefore a direct measure of the Cooper pair condensates of the sample. To get information about an absolute scale of the Josephson coupling between tip and sample we can use the  $P(E)$ -model.

An important point is that in case of a sample with two order parameters  $\Delta_{1,2}$  (like NbSe<sub>2</sub>) the previous relation 6.15 is not applicable anymore. In the simplest case we can assume a model where the total  $I_c$  is the sum of two critical Josephson currents, for  $s^{++}$  pairing.

The Ambegaokar-Baratoff relation of  $I_c$  and  $\Delta$  for multiple bands with  $s^{++}$  pairing follows [Ambegaokar63, Ota09, Ota10, Lin12]:

$$I_c = \sum_{i=1}^2 2 \cdot \frac{G_i}{e} \frac{|\Delta_i \Delta_t|}{|\Delta_i| + |\Delta_t|} \cdot K \left( \frac{|\Delta_i - \Delta_t|}{|\Delta_i| + |\Delta_t|} \right), \quad (6.16)$$

where  $G_i$  and  $\Delta_i$  are the normal state conductance at the Fermi energy and the order parameter of the sample's band  $i$ .

To make the analysis of local variations in  $\Delta$  possible in this case the correct way of extracting the ratio of  $dG_{1/2}$  from their measured sum giving the junction conductance  $dG$  has to be found. This can be achieved by fitting quasi-particle spectra based on the McMillan model as described in chapter 6.2. Here the tunneling selectivities between the tip and the two bands and their density of states are fitting parameters.

To collect more details about this correlation we measured grid spectroscopies on several defects, one of these grids is presented in figure 6.12. A topography acquired simultaneously with the grid is shown in a), no disturbance of the structure due to the defect can be seen, setpoint:  $V = 4\text{mV}$  and  $I = 2.5\text{nA}$ . For comparison another topography at a setpoint of



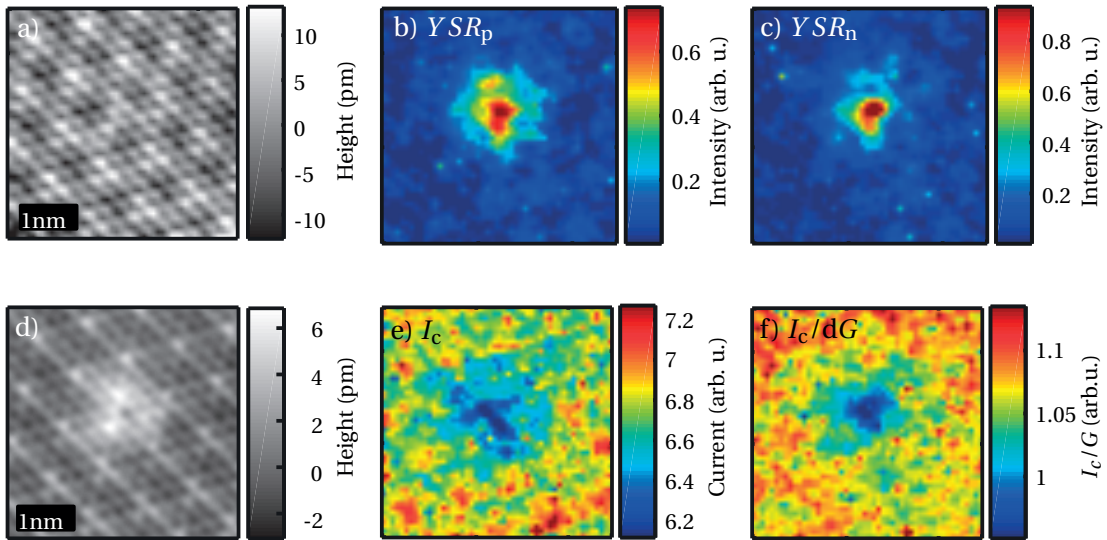


Figure 6.12 – **Plot of key maps of one Fe-defect grid spectroscopy.** The topography is shown in a), the setpoint is:  $V = 4$  mV and  $I = 2.5$  nA. b) and c) show the spatial dependence of the YSR-peak intensities at positive ( $YSR_p$ ) and negative ( $YSR_n$ ) energy, respectively. In d) a topography at a setpoint of  $V = 100$  mV and  $I = 20$  pA is displayed, where the defect is visible in the center of the image. e) gives a map of the local variations of the critical current  $I_c$ , as obtained from the  $P(E)$ -analysis for each point of the grid. In f) the critical Josephson current is plotted normalized by the local differential conductance:  $I_c/dG$ . We find an overall variation of about 20 %.

$V = 100$  mV and  $I = 20$  pA is displayed in d), where the defect's location is apparent. In b) and c) the local variation of the YSR-peak intensities were fitted for positive and negative energies. The intensity distributions clearly differ from each other. Figure 6.12 e) presents the critical current  $I_c$  determined by the  $P(E)$ -analysis for each point of the grid individually. To get a map that is approximately proportional to the order parameter we normalize  $I_c$  to the conductance  $dG$  determined outside the superconducting gap. The results are plotted in f). Comparing the normalized  $I_c$  in f) and the YSR intensity in b) and c) their correlation is evident. Based on this analysis we find the order parameter of NbSe<sub>2</sub> to be reduced at the site of Fe defects by about roughly 20 %. The analysis strongly indicates a significant reduction of the superconducting order parameter around the Fe impurity in NbSe<sub>2</sub>.

## 6.4 Conclusions

In this chapter we analyzed the effects of local pair breaking potentials in the two gap superconductor NbSe<sub>2</sub>. To induce these potentials we doped the NbSe<sub>2</sub> with 0.5 % of Fe impurities, which has a macroscopic effect on the superconductivity, resulting in a reduced critical temperature of 6.1 K. We studied the interaction of the magnetic moments of the defects with the superconducting host by analyzing Yu-Shiba-Rusinov states and also the Josephson coupling

of tip and sample.

We take quasi-particle spectra on two kinds of defects, which we attribute to isolated single substitutions of Nb lattice atoms with Fe and two of these so close together that they interact. On these defects we find YSR-resonance peaks mostly at energy positions coinciding with the coherence peaks and only for the double defect YSR-peaks clearly in the superconducting gap. To analyze this interesting observation we compared it to a theoretical model. This model is based on McMillan's theory for coupled superconducting bands and includes a Maki-like term to account for the magnetic scattering background, which reduces the critical temperature. For the local YSR-resonances we employed T-matrix scattering calculations. With this model we connected the appearance of YSR-peaks on top of coherence peaks to the energy dependent superconducting order parameter of NbSe<sub>2</sub>. The result of this energy dependence is that the gap-edge and the superconducting order parameter  $\Delta$  do not have the same value anymore, in contrast to the case of an unperturbed BCS-like gap. Because already a simple Maki-like depairing term gives a difference between gap-edge and  $\Delta$ , coinciding YSR-resonances and coherence peaks may not be too exotic. They could account for observation of asymmetric coherence peaks also in other studies.

Another important conclusion can be drawn from the good agreement of the theoretical model and the experimental data, compare figure 6.10. The width of the YSR-peaks (which is related to the YSR-states lifetime) is strongly increased if they are outside of the superconducting gap. We demonstrated, that this broadening (reduced lifetime) depends on the imaginary part of  $\Delta$  (not its phase). By this we established YSR-resonances as a probe for the imaginary part of the superconducting order parameter and surmised that even inside the gap non-thermal decay channels can exist.

Additionally, we looked at the suppression of the local Josephson coupling between tip and sample, which indicates a reduction of the  $\Delta$ s of the sample. We showed in a preliminary analysis, that on top of the Fe-impurities the sum of the superconducting order parameters is significantly reduced by about 20 %.

## 7 Conclusions and Outlook

We presented several experimental results based on ultra-low temperature scanning tunneling microscopy at a temperature of 15 mK and introduced significant improvements to its experimental performance. The mK-STM was moved from its old lab to a new Precision Laboratory building that was designed to provide the best possible lab conditions for the most sensitive experiments. Doing so reduced the fluctuations of the tip-sample distance, now at a FWHM-level of about 250 fm at a sampling period of 20 ms by a factor of about 15. In addition, the spectral energy resolution was significantly improved, by carefully accounting for sources of radio-frequency noise in the grounding and improved filtering of the wires going into the cryostat. These improvements helped significantly to realize the experiments in this thesis.

**Quantum back-action and spectral energy resolution in the STM:** The first chapter (3) of this thesis focused on the physical phenomena becoming apparent by combining milli-Kelvin temperatures with an STM-junction. Central considerations include the relative scales of thermal energy  $E_{\text{th}}$ , capacitive energy of the tip-sample junction  $E_C$  and the Josephson coupling energy  $E_J$ . By a combined modeling of three different phenomena measured in an all-Al-junction we demonstrated that STM at milli-Kelvin temperatures is influenced by quantum back-action of the immediate electromagnetic environment of the junction. The investigated phenomena were the quasi-particle gap of the superconductor, the Josephson current and the dynamical Coulomb blockade. One single  $P(E)$ -function which characterizes the junction and is valid for all three measurements we described was found. We used it to fit the quasi-particle excitation spectrum of the superconducting gap, the  $IV$ -curve of the Josephson effect and the dip in the differential conductance of the dynamical Coulomb blockade and found excellent agreement with the data. This combined analysis strongly supports the applicability of the  $P(E)$ -model for ultra-low temperature STM. Quantum effects resulting from the interaction of tunneling particles with the electromagnetic environment become non-negligible. This analysis of the quantum-back action hinted at the possibility of influencing the junction capacitance by increasing the diameter of the wire used to prepare the tip, with the aim to reduce spectroscopic broadening. We found a clear inverse correlation between the tip radius

and the sharpness of features in spectroscopic measurements. The observed increase of spectroscopic energy resolution was connected to an increase of  $C_J$ . Interestingly the broadening depends on the charge number of the particles populating the junction capacitor. If they are electrons and holes with charge  $e$  instead of Cooper pairs with  $2e$ , the broadening reduces by a factor of two. This finding suggests that the  $P(E)$ -function can be understood as the energy resolution function of the STM. We inferred that the junction capacitance will become relevant for other STM-experiments at temperatures around 1 K, where broadening of spectral features induced by capacitive noise is on the order of what is expected from temperature alone, following  $3.5 k_B T$ . Of course, the size of the broadening depends on the precise value of the capacitance and its impact on the width of the investigated features. Some possible examples are the Kondo-effect, Yu-Shiba-Rusinov-resonances or Majorana-states, which can all show extremely narrow peaks. Overall, this means that the spectroscopic resolution of an STM operated at 1 K or below can profit from a large junction capacitance. The simplest way to achieve this is increasing the macroscopic diameter of the tip.

**Single channel transport:** After we further established the importance of the  $P(E)$ -analysis for mK-STM we took a more detailed look at electronic transport in Al Josephson junctions in the STM, in chapter 4. To better understand the consequences of restricting the transport to just a few channels, typically given by the valence of the tip material, we analyzed our junction based on a well-established Andreev reflection model. With this model, it is possible to determine the number of transport channels, as well as the transmission of each of them, yielding a precise description of the junction's transport properties. To study the limiting case of a single channel, we position, by means of STM manipulation, a single Al adatom on the Al(100) surface. On this adatom the transport appears to be restricted to one of the three possible channels expected for the valence of Al, presumably due to the junction geometry. We provide proof that this construction is indeed strongly dominated by a single channel in two ways.

First we acquire the current and differential conductance dependence on the tip-sample distance. We do this in form of simultaneously measured  $I(z)$ - and  $dG(z) = dI/dV(z)$ -curves, at the central position on the adatom, at a bias voltage outside the superconducting gap. We find  $dG(z)$  to have a maximum at the quantum of conductance  $G_0$ , a clear indication for a single-channel junction approaching a transmission of one. In a junction with superconducting electrodes, Andreev reflections inside the gap induce an additional voltage independent current outside of the superconducting gap, the excess current  $I_{\text{exc}}$ . By comparing  $dG(z)$  with the conductance  $G(z) = I(z)/V(z)$ , we demonstrate that the additional transport of Bogoliubov quasi-particles is accounted for by  $I_{\text{exc}}$ . Clearly, this additional current is not bound to the quantum of conductance limit  $G_0$ .

Second, we measured  $IV$ -curves at several tip-sample distances ranging from the tunneling limit up to a conductance around  $G_0$ . We clearly resolve the first and second Andreev reflection as peaks in the spectra and observe the filling of the superconducting gap. At a

---

conductance close to  $G_0$  the spectral weight in the  $dI/dV(z)$ -spectra is concentrated in one single peak around zero bias, also including the Josephson peak. Analyzing these  $IV$ -curves for their Andreev reflections showed that the junction is strongly dominated by one single channel of conductance. Possible other channels stay well below a transmission of  $\tau = 0.01$  for all tip-sample distances, except those close to a junction conductance of  $G_0$ . We therefore demonstrated a single-channel superconducting junction made from an elemental BCS-like material.

In chapter 5 we used this single-channel system to study the transmission dependence of the Josephson effect and how it differs from the many channel and low transmission picture used in the Ambegaokar-Baratoff relation. In this way, we can model the transmission dependence without free parameters for the individual junction conductance values. Compared with the data, the many channel model shows significant deviations with rising transmission. We therefore introduce a new model, based on the full Andreev bound state relation that is valid for single-channel Josephson junctions in the dynamical Coulomb blockade regime. It has a non-linear transmission dependence and includes multiple Cooper pair tunneling. Applying this new model to our measurements, we find that it reproduces the experimental data with high accuracy. To see how large possible variations of the Josephson effect are due to locally varying transport channels, for instance due to adatoms, vacancies, step-edges or even changes of the orbital structure of the crystal surface, we compare the two models in depth. For a single channel at a conductance of  $0.5 G_0$  the difference to the many channel model is about 15 %. We find that even for a junction with five equally contributing channels and a total conductance of  $0.1 G_0$ , at least 0.6 % difference to the many channel picture can be expected. In a real junction the difference is likely higher because the transport is not equally distributed over all available channels. It is rather carried mostly by orbitals pointing towards the sample and less by those parallel to the surface. Concerning multiple Cooper pair transport, Josephson coupling due to two pairs tunneling together can reach 25 % of the coupling from the many channel model at  $G_0$ . These results can also be understood as an extrapolation for other STM experiments, such as the determination of local variations of the superconducting order parameter  $\Delta$  in Josephson-STM (JSTM). To unambiguously and quantitatively determine changes of the sample's  $\Delta$ , the possible local changes of the tunneling conditions have to be regarded. This is especially the case for multi-gap superconductors, where transport to each superconducting band may change independently.

Another quantum effect, which was proposed to have a significant transmission dependence, is the dynamical Coulomb blockade. Similar to the behavior of shot-noise, the dip associated with the DCB is expected to get smaller with rising transmission, until it vanishes at  $\tau = 1$ . Again we used the single-channel Al-junction to study this theoretical proposal. To observe the DCB we quenched superconductivity in tip and sample with a magnetic field of 20 mT. Starting at a low tunneling conductance we saw, in an early and simple analysis, a reduction of the conductance by about 8 %. Going to a higher conductance the dip becomes less pronounced. At the highest conductance, corresponding to a single-channel transmission of  $\tau \approx 1$ , the dip is indistinguishable from its surroundings. Again this observation is in accordance with the

## Chapter 7. Conclusions and Outlook

---

expectations for a single-channel system. A better understanding of the environmental back action on the transport properties of nm scale systems may be critical for future developments in quantum-computation and also for further downsizing of semi-conductor based technology in general. Even if not used directly for a new kind of technology it becomes more and more important to account for quantum effects in the design and operation of nano-patterned devices.

After recalling what we learned about the transport of scanning tunneling microscopes operated at milli-Kelvin temperatures and the single channel behavior of the Josephson effect and the dynamical Coulomb blockade let us now switch to the insight we gathered on a different sample system.

**Local pair breaking potentials in multi-band superconductors:** With the focus on the interaction of local pair breaking potentials, i.e. magnetic defects on superconductors, we studied Fe-doped NbSe<sub>2</sub> samples with a tip of vanadium wire, in chapter 6. Our samples were grown with 0.5 % of Fe, which reduces the critical temperature to 6.1 K. The sample surface shows a statistical distribution of defects with a very low corrugation, about the size of the charge density wave pattern. We studied Yu-Shiba-Rusinov resonance peaks on two kinds of defects with different appearances in topography. The likely difference between them is that one is a single Fe atom replacing a Nb lattice atom and that the other consists of two such defects close together. Interestingly we find YSR-resonances inside the superconducting gap only for the supposed double defect, indicative of a stronger local magnetic moment. At the single defect the YSR-resonances appear at an unreported energy position, outside of the gap and on top of the coherence peaks. Additionally, we observe a strong increase of the FWHM values of the resonance peaks, ranging from narrow peak-widths inside the gap (basically given by the finite energy resolution of our system) to very broad peak-widths of about 400  $\mu\text{V}$  at the highest peak position energies. To describe the sample system we use McMillan's theory for multi-band superconductors with inter-band coupling and a Maki-like extension to account for the scattering background due to the Fe-doping. For modeling the YSR-resonances we use a T-matrix scattering formalism. We extract the peak width to energy position dependence from the modeled and measured data and find excellent agreement between them.

The appearance of YSR-resonances on top of coherence peaks can be understood by considering that the superconducting order parameter  $\Delta$  does not define the edge of the superconducting gap if the system is perturbed, and that the highest energy at which YSR-resonances occur is given by the value of  $\Delta$ . Given the large difference of  $\Delta$  and the gap-edge in NbSe<sub>2</sub>, because of its two-band nature, it is an ideal system to study this effect. The rise of the peak width outside of the gap indicates a reduced lifetime due to the increased coupling to a dissipative channel. The theoretical model shows the same broadening behavior, where it can be connected to the imaginary part of the superconducting order parameters and is not to be mistaken for the order parameter's phase. By comparing experiment and theory, we demonstrated that the



---

imaginary part of  $\Delta$  is well suited to model the peak broadening and that non-thermal decay channels can exist even in the protective superconducting gap. The large broadening here is a result of the inter-band hopping and background scattering. In addition, a small depairing (described by the Dynes parameter) imparts a finite imaginary part to the order parameter. That alone can already lead to dissipation inside the gap. On the other hand, this dependence could be used to probe the imaginary part of the order parameters of superconductors, especially unconventional and non-trivial ones. A better understanding of the imaginary part of the superconducting order parameter may help one to gain a more conclusive picture of these highly interesting materials. Additionally, it can support the search for systems with very little dissipation in which well protected states can be realized, for instance in the context of quantum-computation and simulation.

After that we presented the spatial extent of the Fe-defect induced YSR-resonances and showed some early results of the spatial variations of the amplitude of the superconducting order parameter of NbSe<sub>2</sub>. In a simple comparison of YSR-resonance intensity and Josephson peak height suppression, we found that they both extend over a scale of some nm. Concerning the local order parameter variations, we presented some early results demonstrating clear local changes of the Josephson critical current. These are, normalized by the tunneling conductance  $I_c/dG$  a first approximation of the changes of  $\Delta$ . We find a reduction of about 20 % at the central region of the studied defects, with respect to unperturbed regions. This analysis already is a strong indication of a local suppression of  $\Delta$ .





## Bibliography

- [Allwörden18] Henning von Allwörden, Andreas Eich, Elze J. Knol, Jan Hermenau, Andreas Sonntag, Jan W. Gerritsen, Daniel Wegner and Alexander A. Khajetoorians. *Design and performance of an ultra-high vacuum spin-polarized scanning tunneling microscope operating at 30 mK and in a vector magnetic field*. Review of Scientific Instruments 89(3), p. 033902, 2018. <https://dx.doi.org/10.1063/1.5020045>.
- [Ambegaokar63] Vinay Ambegaokar and Alexis Baratoff. *Tunneling between superconductors*. Phys. Rev. Lett. 10(11), pp. 486, 1963. <https://dx.doi.org/10.1103/PhysRevLett.10.486>.
- [Anderson63] P. W. Anderson and J. M. Rowell. *Probable observation of the Josephson superconducting tunneling effect*. Physical Review Letters 10(6), pp. 230, 1963. <https://dx.doi.org/10.1103/physrevlett.10.230>.
- [Arguello14] C. J. Arguello, S. P. Chockalingam, E. P. Rosenthal, L. Zhao, C. Gutiérrez, J. H. Kang, W. C. Chung, R. M. Fernandes, S. Jia, A. J. Millis, R. J. Cava and A. N. Pasupathy. *Visualizing the charge density wave transition in 2h-NbSe<sub>2</sub> in real space*. Physical Review B 89(23), 2014. <https://dx.doi.org/10.1103/physrevb.89.235115>.
- [Arguello15] C. J. Arguello, E. P. Rosenthal, E. F. Andrade, W. Jin, P. C. Yeh, N. Zaki, S. Jia, R. J. Cava, R. M. Fernandes, A. J. Millis, T. Valla, R. M. Osgood and A. N. Pasupathy. *Quasiparticle interference, quasiparticle interactions, and the origin of the charge density wave in 2h-NbSe<sub>2</sub>*. Physical Review Letters 114(3), 2015. <https://dx.doi.org/10.1103/physrevlett.114.037001>.
- [Assig11] Maximilian Assig. *Development of a millikelvin scanning tunneling microscope for applications in ultra high vacuum and high magnetic fields*. Ph.D. thesis, École Polytechnique Fédérale de Lausanne, 2011. <https://dx.doi.org/10.5075/epfl-thesis-5204>.
- [Assig13] Maximilian Assig, Markus Etzkorn, Axel Enders, Wolfgang Stiepany, Christian R. Ast and Klaus Kern. *A 10 mK scanning tunneling micro-*

## Bibliography

---

- scope operating in ultra high vacuum and high magnetic fields.* Rev. Sci. Instrum. 84(033903), 2013. <https://dx.doi.org/10.1063/1.4793793>.
- [Ast16] Christian R. Ast, Berthold Jäck, Jacob Senkpiel, Matthias Eltschka, Markus Etzkorn, Joachim Ankerhold and Klaus Kern. *Sensing the quantum limit in scanning tunneling spectroscopy.* Nat. Commun. 7(13009), p. 13009, 2016. <https://dx.doi.org/10.1038/ncomms13009>.
- [Averin95] D. Averin and A. Bardas. *ac Josephson effect in a single quantum channel.* Physical Review Letters 75(9), pp. 1831, 1995. <https://dx.doi.org/10.1103/physrevlett.75.1831>.
- [Balatsky06] A. V. Balatsky, I. Vekhter and Jian-Xin Zhu. *Impurity-induced states in conventional and unconventional superconductors.* Rev. Mod. Phys. 78(2), pp. 373, 2006. <https://dx.doi.org/10.1103/revmodphys.78.373>.
- [Bardeen57] J. Bardeen, L. N. Cooper and J. R. Schrieffer. *Theory of superconductivity.* Physical Review 108(5), pp. 1175, 1957. <https://dx.doi.org/10.1103/physrev.108.1175>.
- [Bardeen61] J. Bardeen. *Tunnelling from a many-particle point of view.* Physical Review Letters 6(2), pp. 57, 1961. <https://dx.doi.org/10.1103/physrevlett.6.57>.
- [Barth90] J. V. Barth, H. Brune, G. Ertl and R. J. Behm. *Scanning tunneling microscopy observations on the reconstructed Au(111) surface: Atomic structure, long-range superstructure, rotational domains, and surface defects.* Physical Review B 42(15), pp. 9307, 1990. <https://dx.doi.org/10.1103/physrevb.42.9307>.
- [Bawden16] L. Bawden, S. P. Cooil, F. Mazzola, J. M. Riley, L. J. Collins-McIntyre, V. Sunko, K. W. B. Hunvik, M. Leandersson, C. M. Polley, T. Balasubramanian, T. K. Kim, M. Hoesch, J. W. Wells, G. Balakrishnan, M. S. Bahramy and P. D. C. King. *Spin-valley locking in the normal state of a transition-metal dichalcogenide superconductor.* Nature Communications 7, p. 11711, 2016. <https://dx.doi.org/10.1038/ncomms11711>.
- [Binnig82] G. Binnig, H. Rohrer, Ch. Gerber and E. Weibel. *Tunneling through a controllable vacuum gap.* Applied Physics Letters 40(2), pp. 178, 1982. <https://dx.doi.org/10.1063/1.92999>.
- [Blonder82] G. E. Blonder, M. Tinkham and T. M. Klapwijk. *Transition from metallic to tunneling regimes in superconducting microconstrictions: Excess current, charge imbalance, and supercurrent conversion.* Physical Review B 25(7), pp. 4515, 1982. <https://dx.doi.org/10.1103/physrevb.25.4515>.

- [Boaknin03] Etienne Boaknin, M. A. Tanatar, Johnpierre Paglione, D. Hawthorn, F. Ronning, R. W. Hill, M. Sutherland, Louis Taillefer, Jeff Sonier, S. M. Hayden and J. W. Brill. *Heat conduction in the vortex state of NbSe<sub>2</sub>: Evidence for multiband superconductivity*. Physical Review Letters 90(11), 2003. <https://dx.doi.org/10.1103/physrevlett.90.117003>.
- [Broglie23] Louis de Broglie. *Waves and quanta*. Nature 112(2815), pp. 540, 1923. <https://dx.doi.org/10.1038/112540a0>.
- [Brune92] H. Brune, J. Wintterlin, R. J. Behm and G. Ertl. *Surface migration of "hot" adatoms in the course of dissociative chemisorption of oxygen on Al(111)*. Phys. Rev. Lett. 68(5), pp. 624, 1992. <https://dx.doi.org/10.1103/physrevlett.68.624>.
- [Brune93] H. Brune, J. Wintterlin, J. Trost, G. Ertl, J. Wiechers and R. J. Behm. *Interaction of oxygen with Al(111) studied by scanning tunneling microscopy*. The Journal of Chemical Physics 99(3), pp. 2128, 1993. <https://dx.doi.org/10.1063/1.465278>.
- [Burtzloff15] Andreas Burtzloff, Alexander Weismann, Mads Brandbyge and Richard Berndt. *Shot noise as a probe of spin-polarized transport through single atoms*. Phys. Rev. Lett. 114(1), 2015. <https://dx.doi.org/10.1103/physrevlett.114.016602>.
- [Caldeira83] A. O. Caldeira and A. J. Leggett. *Quantum tunnelling in a dissipative system*. Annals of Physics 149(1), p. 235, 1983. [https://dx.doi.org/10.1016/0003-4916\(83\)90202-6](https://dx.doi.org/10.1016/0003-4916(83)90202-6).
- [Cao18] Yuan Cao, Valla Fatemi, Shiang Fang, Kenji Watanabe, Takashi Taniguchi, Efthimios Kaxiras and Pablo Jarillo-Herrero. *Unconventional superconductivity in magic-angle graphene superlattices*. Nature 2018. <https://dx.doi.org/10.1038/nature26160>.
- [Carabello15] Steven Carabello, Joseph G Lambert, Jerome Mlack, Wenqing Dai, Qi Li, Ke Chen, Daniel Cunnane, C G Zhuang, X X Xi and Roberto C Ramos. *Energy gap substructures in conductance measurements of MgB<sub>2</sub>-based Josephson junctions: beyond the two-gap model*. Superconductor Science and Technology 28(5), p. 055015, 2015. <https://dx.doi.org/10.1088/0953-2048/28/5/055015>.
- [Chaika14] A. N. Chaika, N. N. Orlova, V. N. Semenov, E. Yu. Postnova, S. A. Krasnikov, M. G. Lazarev, S. V. Chekmazov, V. Yu. Aristov, V. G. Glebovsky, S. I. Bozhko and I. V. Shvets. *Fabrication of [001]-oriented tungsten tips for high resolution scanning tunneling microscopy*. Scientific Reports 4(1), 2014. <https://dx.doi.org/10.1038/srep03742>.

## Bibliography

---

- [Chauvin07] M. Chauvin, P. vom Stein, D. Esteve, C. Urbina, J. C. Cuevas and A. Levy Yeyati. *Crossover from Josephson to multiple Andreev reflection currents in atomic contacts*. Physical Review Letters 99(6), 2007. <https://dx.doi.org/10.1103/physrevlett.99.067008>.
- [Chen07] C. Julian Chen. *Introduction to Scanning Tunneling Microscopy*. Oxford University Press, 2007. <https://dx.doi.org/10.1093/acprof:oso/9780199211500.001.0001>.
- [Choi] Deung-Jang Choi, Carlos García Fernández, Edwin Herrera, Carmen Rubio-Verdú, Miguel M. Ugeda, Isabel Guillamón, Hermann Suderow, Jose Ignacio Pascual and Nicolás Lorente. *Probing magnetic interactions between Cr adatoms on the  $\beta$ -Bi<sub>2</sub>Pd superconductor* <https://arxiv.org/1709.09224>. 1709.09224v1.
- [Choi17] Deung-Jang Choi, Carmen Rubio-Verdú, Joeri de Bruijckere, Miguel M. Ugeda, Nicolás Lorente and Jose Ignacio Pascual. *Mapping the orbital structure of impurity bound states in a superconductor*. Nature Communications 8, p. 15175, 2017. <https://dx.doi.org/10.1038/ncomms15175>.
- [Cornils17] L. Cornils, A. Kamlapure, L. Zhou, S. Pradhan, A.A. Khajetoorians, J. Fransson, J. Wiebe and R. Wiesendanger. *Spin-resolved spectroscopy of the Yu-Shiba-Rusinov states of individual atoms*. Physical Review Letters 119(19), 2017. <https://dx.doi.org/10.1103/physrevlett.119.197002>.
- [Cron01] Ronald Cron. *Les contacts atomiques : un banc d'essai pour la physique mésoscopique*. Theses, Université Pierre et Marie Curie - Paris VI, 2001. <https://tel.archives-ouvertes.fr/tel-00001329>.
- [Cuevas96] J. C. Cuevas, A. Martín-Rodero and A. Levy Yeyati. *Hamiltonian approach to the transport properties of superconducting quantum point contacts*. Physical Review B 54(10), pp. 7366, 1996. <https://dx.doi.org/10.1103/physrevb.54.7366>.
- [Cuevas98a] J. C. Cuevas, A. Levy Yeyati and A. Martín-Rodero. *Microscopic origin of conducting channels in metallic atomic-size contacts*. Phys. Rev. Lett. 80(5), pp. 1066, 1998. <https://dx.doi.org/10.1103/physrevlett.80.1066>.
- [Cuevas98b] J. C. Cuevas, A. Levy Yeyati, A. Martín-Rodero, G. Rubio Bollinger, C. Untiedt and N. Agraït. *Evolution of conducting channels in metallic atomic contacts under elastic deformation*. Phys. Rev. Lett. 81(14), pp. 2990, 1998. <https://dx.doi.org/10.1103/physrevlett.81.2990>.
- [Cuevas99] Juan Carlos Cuevas. *Electronic transport in normal and superconducting nanostructures*. Ph.D. thesis, Universidad Autónoma de Madrid, 1999. [http://www.uam.es/personal\\_pdi/ciencias/jcuevas/Publications/thesis.pdf](http://www.uam.es/personal_pdi/ciencias/jcuevas/Publications/thesis.pdf).

- [Cui17] Longji Cui, Wonho Jeong, Sunghoon Hur, Manuel Matt, Jan C. Klöckner, Fabian Pauly, Peter Nielaba, Juan Carlos Cuevas, Edgar Meyhofer and Pramod Reddy. *Quantized thermal transport in single-atom junctions*. Science 355(6330), pp. 1192, 2017. <https://dx.doi.org/10.1126/science.aam6622>.
- [Das12] Anindya Das, Yuval Ronen, Yonatan Most, Yuval Oreg, Moty Heiblum and Hadas Shtrikman. *Zero-bias peaks and splitting in an Al-InAs nanowire topological superconductor as a signature of Majorana fermions*. Nature Physics 8(12), pp. 887, 2012. <https://dx.doi.org/10.1038/nphys2479>.
- [Devoret90] M. H. Devoret, D. Esteve, H. Grabert, G.-L. Ingold, H. Pothier and C. Urbina. *Effect of the electromagnetic environment on the Coulomb blockade in ultrasmall tunnel junctions*. Phys. Rev. Lett. 64(15), pp. 1824, 1990. <https://dx.doi.org/10.1103/physrevlett.64.1824>.
- [Dynes78] R. C. Dynes. *Superconducting tunneling*. In *Springer Series in Solid-State Sciences*, pp. 228–228. Springer Berlin Heidelberg, 1978. [https://dx.doi.org/10.1007/978-3-642-81228-6\\_24](https://dx.doi.org/10.1007/978-3-642-81228-6_24).
- [Einstein05] A. Einstein. *Über einen die Erzeugung und Verwandlung des Lichtes betreffenden heuristischen Gesichtspunkt*. Annalen der Physik 322(6), pp. 132, 1905. <https://dx.doi.org/10.1002/andp.19053220607>.
- [Eltschka14] Matthias Eltschka, Berthold Jäck, Maximilian Assig, Oleg V. Kondrashov, Mikhail A. Skvortsov, Markus Etzkorn, Christian R. Ast and Klaus Kern. *Probing absolute spin polarization at the nanoscale*. Nano Letters 14(12), pp. 7171, 2014. <https://dx.doi.org/10.1021/nl5037947>.
- [Eltschka15] Matthias Alexander Eltschka. *Scanning tunneling microscopy using superconducting tips to probe absolute spin polarization*. Ph.D. thesis, École Polytechnique Fédérale de Lausanne, 2015. <https://dx.doi.org/10.5075/epfl-thesis-6772>.
- [Esaki65] L. Esaki and P. J. Stiles. *Study of electronic band structures by tunneling spectroscopy: Bismuth*. Physical Review Letters 14(22), pp. 902, 1965. <https://dx.doi.org/10.1103/physrevlett.14.902>.
- [Feldman16] Benjamin E. Feldman, Mallika T. Randeria, Jian Li, Sangjun Jeon, Yonglong Xie, Zhijun Wang, Ilya K. Drozdov, B. Andrei Bernevig and Ali Yazdani. *High-resolution studies of the Majorana atomic chain platform*. Nature Physics 13(3), pp. 286, 2016. <https://dx.doi.org/10.1038/nphys3947>.
- [Flatté97a] Michael E. Flatté and Jeff M. Byers. *Local electronic structure of a single magnetic impurity in a superconductor*. Phys. Rev. Lett. 78(19), pp. 3761, 1997. <https://dx.doi.org/10.1103/physrevlett.78.3761>.

## Bibliography

---

- [Flatté97b] Michael E. Flatté and Jeff M. Byers. *Local electronic structure of defects in superconductors*. Phys. Rev. B 56(17), pp. 11213, 1997. <https://dx.doi.org/10.1103/physrevb.56.11213>.
- [Franke11] K. J. Franke, G. Schulze and J. I. Pascual. *Competition of superconducting phenomena and Kondo screening at the nanoscale*. Science 332(6032), pp. 940, 2011. <https://dx.doi.org/10.1126/science.1202204>.
- [Franz96] M. Franz, C. Kallin, P. I. Soininen, A. J. Berlinsky and A. L. Fetter. *Vortex state in ad-wave superconductor*. Physical Review B 53(9), pp. 5795, 1996. <https://dx.doi.org/10.1103/physrevb.53.5795>.
- [Giaever61] Ivar Giaever and Karl Megerle. *Study of superconductors by electron tunneling*. Physical Review 122(4), pp. 1101, 1961. <https://dx.doi.org/10.1103/physrev.122.1101>.
- [Giaever62] I. Giaever, H. R. Hart and K. Megerle. *Tunneling into superconductors at temperatures below 1 K*. Physical Review 126(3), pp. 941, 1962. <https://dx.doi.org/10.1103/physrev.126.941>.
- [Golubev01] Dmitrii S. Golubev and Andrei D. Zaikin. *Coulomb interaction and quantum transport through a coherent scatterer*. Physical Review Letters 86(21), pp. 4887, 2001. <https://dx.doi.org/10.1103/physrevlett.86.4887>.
- [Golubov97] A. A. Golubov and I. I. Mazin. *Effect of magnetic and nonmagnetic impurities on highly anisotropic superconductivity*. Physical Review B 55(22), pp. 15146, 1997. <https://dx.doi.org/10.1103/physrevb.55.15146>.
- [Golubov04] A. A. Golubov, M. Yu. Kupriyanov and E. Il'ichev. *The current-phase relation in Josephson junctions*. Rev. Mod. Phys. 76(2), pp. 411, 2004. <https://dx.doi.org/10.1103/revmodphys.76.411>.
- [Gottlieb06] Alex D Gottlieb and Lisa Wesoloski. *Bardeen's tunnelling theory as applied to scanning tunnelling microscopy: a technical guide to the traditional interpretation*. Nanotechnology 17(8), pp. R57, 2006. <https://dx.doi.org/10.1088/0957-4484/17/8/r01>.
- [Graham17] Martin Graham and Dirk K. Morr. *Imaging the spatial form of a superconducting order parameter via Josephson scanning tunneling spectroscopy*. Physical Review B 96(18), 2017. <https://dx.doi.org/10.1103/physrevb.96.184501>.
- [Gross12] Rudolf Gross and Achim Marx. *Festkörperphysik*. Oldenbourg Wissenschaft.Vlg, 2012. ISBN 978-3-486-71294-0.



- [Guillamon08] I. Guillamon, H. Suderow, S. Vieira and P. Rodiere. *Scanning tunneling spectroscopy with superconducting tips of Al*. Physica C: Superconductivity and its Applications 468(7-10), pp. 537, 2008. <https://dx.doi.org/10.1016/j.physc.2007.11.066>.
- [Haan14] A. M. J. den Haan, G. H. C. J. Wijts, F. Galli, O. Usenko, G. J. C. van Baarle, D. J. van der Zalm and T. H. Oosterkamp. *Atomic resolution scanning tunneling microscopy in a cryogen free dilution refrigerator at 15 mK*. Review of Scientific Instruments 85(3), p. 035112, 2014. <https://dx.doi.org/10.1063/1.4868684>.
- [Hatter15] Nino Hatter, Benjamin W. Heinrich, Michael Ruby, Jose I. Pascual and Katharina J. Franke. *Magnetic anisotropy in Shiba bound states across a quantum phase transition*. Nat. Commun. 6, p. 8988, 2015. <https://dx.doi.org/10.1038/ncomms9988>.
- [Heinrich13] B. W. Heinrich, L. Braun, J. I. Pascual and K. J. Franke. *Protection of excited spin states by a superconducting energy gap*. Nat. Phys. 9(12), pp. 765, 2013. <https://dx.doi.org/10.1038/nphys2794>.
- [Heinrich18] Benjamin W. Heinrich, Jose I. Pascual and Katharina J. Franke. *Single magnetic adsorbates on s-wave superconductors*. Progress in Surface Science 93(1), pp. 1, 2018. <https://dx.doi.org/10.1016/j.progsurf.2018.01.001>.
- [Hudson01] E. W. Hudson, K. M. Lang, V. Madhavan, S. H. Pan, H. Eisaki, S. Uchida and J. C. Davis. *Interplay of magnetism and high- $T_c$  superconductivity at individual Ni impurity atoms in  $\text{Bi}_2\text{Sr}_2\text{CaCu}_2\text{O}_{8+\delta}$* . Nature 411(6840), pp. 920, 2001. <https://dx.doi.org/10.1038/35082019>.
- [Iansiti87] M. Iansiti, A. T. Johnson, Walter F. Smith, H. Rogalla, C. J. Lobb and M. Tinkham. *Charging energy and phase delocalization in single very small Josephson tunnel junctions*. Phys. Rev. Lett. 59(4), pp. 489, 1987. <https://dx.doi.org/10.1103/physrevlett.59.489>.
- [Ingold91] G.-L. Ingold and H. Grabert. *Finite-temperature current-voltage characteristics of ultrasmall tunnel junctions*. Europhysics Letters (EPL) 14(4), pp. 371, 1991. <https://dx.doi.org/10.1209/0295-5075/14/4/015>.
- [Ingold92] Gert-Ludwig Ingold and Yu. V. Nazarov. *Charge tunneling rates in ultrasmall junctions*. In *NATO ASI Series*, pp. 21–107. Springer US, 1992. [https://dx.doi.org/10.1007/978-1-4757-2166-9\\_2](https://dx.doi.org/10.1007/978-1-4757-2166-9_2).
- [Ingold94] Gert-Ludwig Ingold, Hermann Grabert and Udo Eberhardt. *Cooper-pair current through ultrasmall Josephson junctions*. Phys. Rev. B 50(1), pp. 395, 1994. <https://dx.doi.org/10.1103/physrevb.50.395>.

## Bibliography

---

- [Ivanchenko69] Yu. M. Ivanchenko and L. A. Zil'berman. *The Josephson effect in small tunnel contacts*. SOVIET PHYSICS JETP (6), 1969. [http://jetp.ac.ru/cgi-bin/dn/e\\_028\\_06\\_1272.pdf](http://jetp.ac.ru/cgi-bin/dn/e_028_06_1272.pdf).
- [Jäck15a] Berthold Jäck, Matthias Eltschka, Maximilian Assig, Markus Etzkorn, Christian R. Ast and Klaus Kern. *Critical Josephson current in the dynamical Coulomb blockade regime*. Phys. Rev. B 93(2), 2015. <https://dx.doi.org/10.1103/PhysRevB.93.020504>.
- [Jäck15b] Berthold Jäck, Matthias Eltschka, Maximilian Assig, Andreas Hardock, Markus Etzkorn, Christian R. Ast and Klaus Kern. *A nanoscale gigahertz source realized with Josephson scanning tunneling microscopy*. Appl. Phys. Lett. 106(1), p. 013109, 2015. <https://dx.doi.org/10.1063/1.4905322>.
- [Jäck17] Berthold Jäck, Jacob Senkpiel, Markus Etzkorn, Joachim Ankerhold, Christian R. Ast and Klaus Kern. *Quantum Brownian motion at strong dissipation probed by superconducting tunnel junctions*. Physical Review Letters 119(14), 2017. <https://dx.doi.org/10.1103/physrevlett.119.147702>.
- [Jäck18] Berthold Jäck, Jacob Senkpiel, Markus Etzkorn, Joachim Ankerhold, Christian R. Ast and Klaus Kern. *Signatures of phase-coherent transport and the role of quantum fluctuations in the dynamical Coulomb blockade regime*. ArXiv 2018. <https://arxiv.org/abs/1712.07172>.
- [Jäck15] Berthold Jäck. *Josephson tunneling at the atomic scale: The Josephson effect as a local probe*. Ph.D. thesis, École Polytechnique Fédérale de Lausanne, 2015. <https://dx.doi.org/10.5075/epfl-thesis-6750>.
- [Jeon17] Sangjun Jeon, Yonglong Xie, Jian Li, Zhijun Wang, B. Andrei Bernevig and Ali Yazdani. *Distinguishing a Majorana zero mode using spin-resolved measurements*. Science 358(6364), pp. 772, 2017. <https://dx.doi.org/10.1126/science.aan3670>.
- [Ji08] Shuai-Hua Ji, Tong Zhang, Ying-Shuang Fu, Xi Chen, Xu-Cun Ma, Jia Li, Wen-Hui Duan, Jin-Feng Jia and Qi-Kun Xue. *High-resolution scanning tunneling spectroscopy of magnetic impurity induced bound states in the superconducting gap of Pb thin films*. Phys. Rev. Lett. 100(22), 2008. <https://dx.doi.org/10.1103/physrevlett.100.226801>.
- [Jona67] F. Jona. *Preparation and properties of clean surfaces of aluminum*. J. Phys. Chem. Solids 7(3), p. 280, 1967. [https://dx.doi.org/10.1016/0022-3697\(67\)90239-9](https://dx.doi.org/10.1016/0022-3697(67)90239-9).
- [Josephson62] B.D. Josephson. *Possible new effects in superconductive tunnelling*. Physics Letters 1(7), pp. 251, 1962. [https://dx.doi.org/10.1016/0031-9163\(62\)91369-0](https://dx.doi.org/10.1016/0031-9163(62)91369-0).



- [Josephson64] B. D. Josephson. *Coupled superconductors*. Rev. Mod. Phys. 36(1), pp. 216, 1964. <https://dx.doi.org/10.1103/revmodphys.36.216>.
- [Josephson65] B.D. Josephson. *Supercurrents through barriers*. Adv. Phys. 14(56), pp. 419, 1965. <https://dx.doi.org/10.1080/00018736500101091>.
- [Kambara07] H. Kambara, T. Matsui, Y. Niimi and Hiroshi Fukuyama. *Construction of a versatile ultralow temperature scanning tunneling microscope*. Review of Scientific Instruments 78(7), p. 073703, 2007. <https://dx.doi.org/10.1063/1.2751095>.
- [Kezilebieke18] Shawulienu Kezilebieke, Marc Dvorak, Teemu Ojanen and Peter Liljeroth. *Coupled Yu–Shiba–Rusinov states in molecular dimers on NbSe<sub>2</sub>*. Nano Letters 18(4), pp. 2311, 2018. <https://dx.doi.org/10.1021/acs.nanolett.7b05050>.
- [Kim15] Howon Kim and Yukio Hasegawa. *Site-dependent evolution of electrical conductance from tunneling to atomic point contact*. Phys. Rev. Lett. 114(20), 2015. <https://dx.doi.org/10.1103/physrevlett.114.206801>.
- [Kimura08] Hikari Kimura, R. P. Barber, S. Ono, Yoichi Ando and R. C. Dynes. *Scanning Josephson tunneling microscopy of single-crystal Bi<sub>2</sub>Sr<sub>2</sub>CaCu<sub>2</sub>O<sub>8+δ</sub> with a conventional superconducting tip*. Phys. Rev. Lett. 101(3), 2008. <https://dx.doi.org/10.1103/physrevlett.101.037002>.
- [Kimura09] Hikari Kimura, R. P. Barber, S. Ono, Yoichi Ando and R. C. Dynes. *Josephson scanning tunneling microscopy: A local and direct probe of the superconducting order parameter*. Phys. Rev. B 80(14), 2009. <https://dx.doi.org/10.1103/physrevb.80.144506>.
- [Klitzing80] K. v. Klitzing, G. Dorda and M. Pepper. *New method for high-accuracy determination of the fine-structure constant based on quantized hall resistance*. Physical Review Letters 45(6), pp. 494, 1980. <https://dx.doi.org/10.1103/physrevlett.45.494>.
- [Kondo64] J. Kondo. *Resistance minimum in dilute magnetic alloys*. Progress of Theoretical Physics 32(1), pp. 37, 1964. <https://dx.doi.org/10.1143/ptp.32.37>.
- [Kulik00] Igor O. Kulik and Recai Ellialtioglu. *Quantum Mesoscopic Phenomena and Mesoscopic Devices in Microelectronics*. Springer, 2000. ISBN 978-0-7923-6626-3. <https://dx.doi.org/10.1007/978-94-011-4327-1>.
- [Landauer87] R. Landauer. *Electrical transport in open and closed systems*. Zeitschrift für Physik B Condensed Matter 68(2-3), pp. 217, 1987. <https://dx.doi.org/10.1007/bf01304229>.

## Bibliography

---

- [Levy Yeyati97] A. Levy Yeyati, A. Martín-Rodero and F. Flores. *Conductance quantization and electron resonances in sharp tips and atomic-size contacts*. Physical Review B 56(16), pp. 10369, 1997. <https://dx.doi.org/10.1103/physrevb.56.10369>.
- [Levy Yeyati01] A. Levy Yeyati, A. Martin-Rodero, D. Esteve and C. Urbina. *Direct link between Coulomb blockade and shot noise in a quantum-coherent structure*. Physical Review Letters 87(4), 2001. <https://dx.doi.org/10.1103/physrevlett.87.046802>.
- [Levy Yeyati05] A. Levy Yeyati and J.M. van Ruitenbeek. *Course 8 transport at the atomic scale: Atomic and molecular contacts*. In *Nanophysics: Coherence and Transport, École d'été de Physique des Houches Session LXXXI*, pp. 495–535. Elsevier, 2005. [https://dx.doi.org/10.1016/s0924-8099\(05\)80052-6](https://dx.doi.org/10.1016/s0924-8099(05)80052-6).
- [Lian17] Chao-Sheng Lian, Chen Si, Jian Wu and Wenhui Duan. *First-principles study of Na-intercalated bilayer NbSe<sub>2</sub> : Suppressed charge-density wave and strain-enhanced superconductivity*. Physical Review B 96(23), 2017. <https://dx.doi.org/10.1103/physrevb.96.235426>.
- [Lin12] Shi-Zeng Lin. *Josephson effect between a two-band superconductor with  $s++$  or  $s\pm$  pairing symmetry and a conventional  $s$ -wave superconductor*. Phys. Rev. B 86(1), 2012. <https://dx.doi.org/10.1103/physrevb.86.014510>.
- [Lv17] Yan-Feng Lv, Wen-Lin Wang, Yi-Min Zhang, Hao Ding, Wei Li, Lili Wang, Ke He, Can-Li Song, Xu-Cun Ma and Qi-Kun Xue. *Experimental signature of topological superconductivity and Majorana zero modes on  $\beta$ -Bi<sub>2</sub>Pd thin films*. Science Bulletin 62(12), pp. 852, 2017. <https://dx.doi.org/10.1016/j.scib.2017.05.008>.
- [Maki64] K. Maki. *Pauli paramagnetism and superconducting state. II*. Progress of Theoretical Physics 32(1), pp. 29, 1964. <https://dx.doi.org/10.1143/ptp.32.29>.
- [Maldonado13] A. Maldonado, S. Vieira and H. Suderow. *Supercurrent on a vortex core in 2h-NbSe<sub>2</sub>: Current-driven scanning tunneling spectroscopy measurements*. Phys. Rev. B 88(6), 2013. <https://dx.doi.org/10.1103/physrevb.88.064518>.
- [Martin14] Ivar Martin and Dmitry Mozyrsky. *Nonequilibrium theory of tunneling into a localized state in a superconductor*. Physical Review B 90(10), 2014. <https://dx.doi.org/10.1103/physrevb.90.100508>.
- [Marz10] M. Marz, G. Goll and H. v. Löhneysen. *A scanning tunneling microscope for a dilution refrigerator*. Review of Scientific Instruments 81(4), p. 045102, 2010. <https://dx.doi.org/10.1063/1.3328059>.

- [Massarotti15] D. Massarotti, A. Pal, G. Rotoli, L. Longobardi, M. G. Blamire and F. Tafuri. *Macroscopic quantum tunnelling in spin filter ferromagnetic josephson junctions*. Nature Communications 6(1), 2015. <https://dx.doi.org/10.1038/ncomms8376>.
- [Maxwell50] Emanuel Maxwell. *Isotope effect in the superconductivity of mercury*. Physical Review 78(4), pp. 477, 1950. <https://dx.doi.org/10.1103/physrev.78.477>.
- [McMillan68] W. L. McMillan. *Tunneling model of the superconducting proximity effect*. Physical Review 175(2), pp. 537, 1968. <https://dx.doi.org/10.1103/physrev.175.537>.
- [Meissner33] W. Meissner and R. Ochsenfeld. *Ein neuer Effekt bei Eintritt der Supraleitfähigkeit*. Die Naturwissenschaften 21(44), pp. 787, 1933. <https://dx.doi.org/10.1007/bf01504252>.
- [Ménard15] Gerbold C. Ménard, Sébastien Guissart, Christophe Brun, Stéphane Pons, Vasily S. Stolyarov, François Debontridder, Matthieu V. Leclerc, Etienne Janod, Laurent Cario, Dimitri Roditchev, Pascal Simon and Tristan Cren. *Coherent long-range magnetic bound states in a superconductor*. Nat. Phys. 11(12), pp. 1013, 2015. <https://dx.doi.org/10.1038/nphys3508>.
- [Meservey70] R. Meservey, P. M. Tedrow and Peter Fulde. *Magnetic field splitting of the quasiparticle states in superconducting aluminum films*. Phys. Rev. Lett. 25(18), pp. 1270, 1970. <https://dx.doi.org/10.1103/physrevlett.25.1270>.
- [Meservey94] R. Meservey and P.M. Tedrow. *Spin-polarized electron tunneling*. Phys. Rep. 238(4), pp. 173, 1994. [https://dx.doi.org/10.1016/0370-1573\(94\)90105-8](https://dx.doi.org/10.1016/0370-1573(94)90105-8).
- [Misra13] S. Misra, B. B. Zhou, I. K. Drozdov, J. Seo, L. Urban, A. Gyenis, S. C. J. Kingsley, H. Jones and A. Yazdani. *Design and performance of an ultra-high vacuum scanning tunneling microscope operating at dilution refrigerator temperatures and high magnetic fields*. Review of Scientific Instruments 84(10), p. 103903, 2013. <https://dx.doi.org/10.1063/1.4822271>.
- [Moncton75] D. E. Moncton, J. D. Axe and F. J. DiSalvo. *Study of superlattice formation in 2H-NbSe<sub>2</sub> and 2H-TaSe<sub>2</sub> by neutron scattering*. Physical Review Letters 34(12), pp. 734, 1975. <https://dx.doi.org/10.1103/physrevlett.34.734>.
- [Moussy01] N. Moussy, H. Courtois and B. Pannetier. *A very low temperature scanning tunneling microscope for the local spectroscopy of mesoscopic structures*. Review of Scientific Instruments 72(1), pp. 128, 2001. <https://dx.doi.org/10.1063/1.1331328>.

## Bibliography

---

- [Naaman01] O. Naaman, W. Teizer and R. C. Dynes. *Fluctuation dominated Josephson tunneling with a scanning tunneling microscope*. Phys. Rev. Lett. 87(9), 2001. <https://dx.doi.org/10.1103/physrevlett.87.097004>.
- [Naaman03] O. Naaman, R. C. Dynes and E. Bucher. *Josephson effect in Pb/I/NbSe<sub>2</sub> scanning tunneling microscope junctions*. International Journal of Modern Physics B 17(18n20), pp. 3569, 2003. <https://dx.doi.org/10.1142/s0217979203021423>.
- [Naaman04] O. Naaman and R.C. Dynes. *Subharmonic gap structure in superconducting scanning tunneling microscope junctions*. Solid State Commun. 129(5), pp. 299, 2004. <https://dx.doi.org/10.1016/j.ssc.2003.10.022>.
- [Nadj-Perge14] S. Nadj-Perge, I. K. Drozdov, J. Li, H. Chen, S. Jeon, J. Seo, A. H. MacDonald, B. A. Bernevig and A. Yazdani. *Observation of Majorana fermions in ferromagnetic atomic chains on a superconductor*. Science 346(6209), pp. 602, 2014. <https://dx.doi.org/10.1126/science.1259327>.
- [Noat10] Y. Noat, T. Cren, F. Debontridder, D. Roditchev, W. Sacks, P. Toulemonde and A. San Miguel. *Signatures of multigap superconductivity in tunneling spectroscopy*. Phys. Rev. B 82(1), 2010. <https://dx.doi.org/10.1103/physrevb.82.014531>.
- [Noat15] Y. Noat, J. A. Silva-Guillén, T. Cren, V. Cherkez, C. Brun, S. Pons, F. Debontridder, D. Roditchev, W. Sacks, L. Cario, P. Ordejón, A. García and E. Canadell. *Quasiparticle spectra of 2H-NbSe<sub>2</sub>: Two-band superconductivity and the role of tunneling selectivity*. Phys. Rev. B 92(13), 2015. <https://dx.doi.org/10.1103/physrevb.92.134510>.
- [Nobel Media AB18] Nobel Media AB. *Nobelprize.org*, 2018. <https://www.nobelprize.org/nomination/>.
- [Octavio83] M. Octavio, M. Tinkham, G. E. Blonder and T. M. Klapwijk. *Subharmonic energy-gap structure in superconducting constrictions*. Physical Review B 27(11), pp. 6739, 1983. <https://dx.doi.org/10.1103/physrevb.27.6739>.
- [Odintsov88] A. A. Odintsov. *Effect of dissipation on the characteristics of small-area tunnel junctions: Application of the polaron model*. JETP 67(6), p. 1265, 1988. [http://www.jetp.ac.ru/cgi-bin/dn/e\\_067\\_06\\_1265.pdf](http://www.jetp.ac.ru/cgi-bin/dn/e_067_06_1265.pdf). Russian original - ZhETF, Vol. 94, No. 6, p. 312, June 1988.
- [Ota09] Yukihiro Ota, Masahiko Machida, Tomio Koyama and Hideki Matsumoto. *Theory of heterotic superconductor-insulator-superconductor Josephson junctions between single- and multiple-gap superconductors*. Physical Review Letters 102(23), 2009. <https://dx.doi.org/10.1103/physrevlett.102.237003>.

- [Ota10] Yukihiro Ota, Noriyuki Nakai, Hiroki Nakamura, Masahiko Machida, Daisuke Inotani, Yoji Ohashi, Tomio Koyama and Hideki Matsumoto. *Ambegaokar-Baratoff relations for Josephson critical current in heterojunctions with multigap superconductors*. Phys. Rev. B 81, p. 214511, 2010. <https://dx.doi.org/10.1103/PhysRevB.81.214511>.
- [Pan98] S. H. Pan, E. W. Hudson and J. C. Davis. *Vacuum tunneling of superconducting quasiparticles from atomically sharp scanning tunneling microscope tips*. Applied Physics Letters 73(20), pp. 2992, 1998. <https://dx.doi.org/10.1063/1.122654>.
- [Parmentier11] F. D. Parmentier, A. Anthore, S. Jezouin, H. le Sueur, U. Gennser, A. Cavanna, D. Mailly and F. Pierre. *Strong back-action of a linear circuit on a single electronic quantum channel*. Nature Physics 7(12), pp. 935, 2011. <https://dx.doi.org/10.1038/nphys2092>.
- [Pervin17] Rukshana Pervin, Manikanadan Krishnan, Amit Kumar Rana, M. Kannan, S. Arumugam and Parasharam M. Shirage. *Enhancement of superconducting critical current density by Fe impurity substitution in NbSe<sub>2</sub> single crystals and the vortex pinning mechanism*. Physical Chemistry Chemical Physics 19(18), pp. 11230, 2017. <https://dx.doi.org/10.1039/c7cp00784a>.
- [Planck00] Max Planck. *Über irreversible Strahlungsvorgänge*. Annalen der Physik 306(1), pp. 69, 1900. <https://dx.doi.org/10.1002/andp.19003060105>.
- [Potter12] Andrew C. Potter and Patrick A. Lee. *Topological superconductivity and Majorana fermions in metallic surface states*. Physical Review B 85(9), 2012. <https://dx.doi.org/10.1103/physrevb.85.094516>.
- [Proslie06] Th Proslie, A Kohen, Y Noat, T Cren, D Roditchev and W Sacks. *Probing the superconducting condensate on a nanometer scale*. Europhysics Letters (EPL) 73(6), pp. 962, 2006. <https://dx.doi.org/10.1209/epl/i2005-10488-0>.
- [Randeria16] Mallika T. Randeria, Benjamin E. Feldman, Ilya K. Drozdov and Ali Yazdani. *Scanning Josephson spectroscopy on the atomic scale*. Physical Review B 93(16), 2016. <https://dx.doi.org/10.1103/physrevb.93.161115>.
- [Reynolds50] C. A. Reynolds, B. Serin, W. H. Wright and L. B. Nesbitt. *Superconductivity of isotopes of mercury*. Physical Review 78(4), pp. 487, 1950. <https://dx.doi.org/10.1103/physrev.78.487>.
- [Rodrigo04a] J G Rodrigo, H Suderow, S Vieira, E Bascones and F Guinea. *Superconducting nanostructures fabricated with the scanning tunnelling microscope*. J. Phys.: Condens. Matter 16(34), pp. R1151, 2004. <https://dx.doi.org/10.1088/0953-8984/16/34/r01>.

## Bibliography

---

- [Rodrigo04b] J.G. Rodrigo and S. Vieira. *STM study of multiband superconductivity in NbSe<sub>2</sub> using a superconducting tip*. Physica C 404(1-4), pp. 306, 2004. <https://dx.doi.org/10.1016/j.physc.2003.10.030>.
- [Rodrigo06] J.G. Rodrigo, V. Crespo and S. Vieira. *Josephson current at atomic scale: Tunneling and nanocontacts using a STM*. Physica C: Superconductivity and its Applications 437-438, pp. 270, 2006. <https://dx.doi.org/10.1016/j.physc.2005.12.040>.
- [Ronen16] Yuval Ronen, Yonatan Cohen, Jung-Hyun Kang, Arbel Haim, Maria-Theresa Rieder, Moty Heiblum, Diana Mahalu and Hadas Shtrikman. *Charge of a quasiparticle in a superconductor*. Proceedings of the National Academy of Sciences 113(7), pp. 1743, 2016. <https://dx.doi.org/10.1073/pnas.1515173113>.
- [Roychowdhury14] Anita Roychowdhury, M. A. Gubrud, R. Dana, J. R. Anderson, C. J. Lobb, F. C. Wellstood and M. Dreyer. *A 30 mK, 13.5 T scanning tunneling microscope with two independent tips*. Review of Scientific Instruments 85(4), p. 043706, 2014. <https://dx.doi.org/10.1063/1.4871056>.
- [Roychowdhury15] A. Roychowdhury, M. Dreyer, J. R. Anderson, C. J. Lobb and F. C. Wellstood. *Microwave photon-assisted incoherent Cooper-pair tunneling in a Josephson STM*. Phys. Rev. Appl 4(3), 2015. <https://dx.doi.org/10.1103/physrevapplied.4.034011>.
- [Ruby15a] Michael Ruby, Benjamin W. Heinrich, Jose I. Pascual and Katharina J. Franke. *Experimental demonstration of a two-band superconducting state for lead using scanning tunneling spectroscopy*. Phys. Rev. Lett. 114(15), 2015. <https://dx.doi.org/10.1103/physrevlett.114.157001>.
- [Ruby15b] Michael Ruby, Falko Pientka, Yang Peng, Felix von Oppen, Benjamin W. Heinrich and Katharina J. Franke. *Tunneling processes into localized subgap states in superconductors*. Phys. Rev. Lett. 115(8), 2015. <https://dx.doi.org/10.1103/physrevlett.115.087001>.
- [Ruby16] Michael Ruby, Yang Peng, Felix von Oppen, Benjamin W. Heinrich and Katharina J. Franke. *Orbital picture of Yu-Shiba-Rusinov multiplets*. Physical Review Letters 117(18), 2016. <https://dx.doi.org/10.1103/physrevlett.117.186801>.
- [Ruby17] Michael Ruby, Benjamin W. Heinrich, Yang Peng, Felix von Oppen and Katharina J. Franke. *Exploring a proximity-coupled Co chain on Pb(110) as a possible Majorana platform*. Nano Letters 17(7), pp. 4473, 2017. <https://dx.doi.org/10.1021/acs.nanolett.7b01728>.



- [Rusinov69a] A. I. Rusinov. *On the theory of gapless superconductivity in alloys containing paramagnetic impurities*. Soviet Journal of Experimental and Theoretical Physics 29, p. 1101, 1969. Zh. Eksp. Teor. Fiz. 56, 2047.
- [Rusinov69b] A. I. Rusinov. *Superconductivity near a paramagnetic impurity*. Soviet Journal of Experimental and Theoretical Physics Letters 9, p. 85, 1969. [http://www.jetpletters.ac.ru/ps/1658/article\\_25295.pdf](http://www.jetpletters.ac.ru/ps/1658/article_25295.pdf). Zh. Eksp. Teor. Fiz. Pis'ma Red. 9, 146.
- [Salkola97] M. I. Salkola, A. V. Balatsky and J. R. Schrieffer. *Spectral properties of quasiparticle excitations induced by magnetic moments in superconductors*. Phys. Rev. B 55(18), pp. 12648, 1997. <https://dx.doi.org/10.1103/physrevb.55.12648>.
- [Scheer97] E. Scheer, P. Joyez, D. Esteve, C. Urbina and M. H. Devoret. *Conduction channel transmissions of atomic-size aluminum contacts*. Physical Review Letters 78(18), pp. 3535, 1997. <https://dx.doi.org/10.1103/physrevlett.78.3535>.
- [Scheer98] Elke Scheer, Nicolás Agrait, Juan Carlos Cuevas, Alfredo Levy Yeyati, Bas Ludoph, Alvaro Martín-Rodero, Gabino Rubio Bollinger, Jan M. van Ruitenbeek and Cristián Urbina. *The signature of chemical valence in the electrical conduction through a single-atom contact*. Nature 394(6689), pp. 154, 1998. <https://dx.doi.org/10.1038/28112>.
- [Scheer00] E Scheer, J.C Cuevas, A. Levy Yeyati, A Martín-Rodero P Joyez, M.H Devoret, D Esteve and C Urbina. *Conduction channels of superconducting quantum point contacts*. Physica B: Condensed Matter 280(1-4), pp. 425, 2000. [https://dx.doi.org/10.1016/s0921-4526\(99\)01812-8](https://dx.doi.org/10.1016/s0921-4526(99)01812-8).
- [Schlottmann76] P. Schlottmann. *Spatial variations of the order parameter in superconductors containing a magnetic impurity*. Physical Review B 13(1), pp. 1, 1976. <https://dx.doi.org/10.1103/physrevb.13.1>.
- [Schrödinger26] E. Schrödinger. *Quantisierung als Eigenwertproblem*. Annalen der Physik 385(13), pp. 437, 1926. <https://dx.doi.org/10.1002/andp.19263851302>.
- [Schutter85] F. De Schutter, Y. Bruynseraede and A. Gilibert. *Magnetic properties of pure superconducting vanadium foils*. Journal of Low Temperature Physics 58(1-2), pp. 27, 1985. <https://dx.doi.org/10.1007/bf00682564>.
- [Seidel11] Paul Seidel. *Josephson effects in iron based superconductors*. Supercond. Sci. Technol. 24(4), p. 043001, 2011. <https://dx.doi.org/10.1088/0953-2048/24/4/043001>.
- [Shiba68] Hiroyuki Shiba. *Classical spins in superconductors*. Progress of Theoretical Physics 40(3), pp. 435, 1968. <https://dx.doi.org/10.1143/ptp.40.435>.

## Bibliography

---

- [Silva-Guillén16] José Ángel Silva-Guillén, Pablo Ordejón, Francisco Guinea and Enric Canadell. *Electronic structure of 2h-NbSe<sub>2</sub> single-layers in the CDW state*. 2D Materials 3(3), p. 035028, 2016. <https://dx.doi.org/10.1088/2053-1583/3/3/035028>.
- [Šmakov01] Jurij Šmakov, Ivar Martin and Alexander V. Balatsky. *Josephson scanning tunneling microscopy*. Physical Review B 64(21), 2001. <https://dx.doi.org/10.1103/physrevb.64.212506>.
- [Song10] Young Jae Song, Alexander F. Otte, Vladimir Shvarts, Zuyu Zhao, Young Kuk, Steven R. Blankenship, Alan Band, Frank M. Hess and Joseph A. Stroscio. *Invited review article: A 10 mK scanning probe microscopy facility*. Review of Scientific Instruments 81(12), p. 121101, 2010. <https://dx.doi.org/10.1063/1.3520482>.
- [Soumyanarayanan13] A. Soumyanarayanan, M. M. Yee, Y. He, J. van Wezel, D. J. Rahn, K. Rossnagel, E. W. Hudson, M. R. Norman and J. E. Hoffman. *Quantum phase transition from triangular to stripe charge order in NbSe<sub>2</sub>*. Proceedings of the National Academy of Sciences 110(5), pp. 1623, 2013. <https://dx.doi.org/10.1073/pnas.1211387110>.
- [Staley09] Neal E. Staley, Jian Wu, Peter Eklund, Ying Liu, Linjun Li and Zhuan Xu. *Electric field effect on superconductivity in atomically thin flakes of NbSe<sub>2</sub>*. Physical Review B 80(18), 2009. <https://dx.doi.org/10.1103/physrevb.80.184505>.
- [Suderow02] H Suderow, M Crespo, P Martinez-Samper, J.G Rodrigo, G Rubio-Bollinger, S Vieira, N Luchier, J.P Brison and P.C Canfield. *Scanning tunneling microscopy and spectroscopy at very low temperatures*. Physica C: Superconductivity 369(1-4), pp. 106, 2002. [https://dx.doi.org/10.1016/s0921-4534\(01\)01228-x](https://dx.doi.org/10.1016/s0921-4534(01)01228-x).
- [Suter16] Dieter Suter and Gonzalo A. Álvarez. *Colloquium: Protecting quantum information against environmental noise*. Reviews of Modern Physics 88(4), 2016. <https://dx.doi.org/10.1103/revmodphys.88.041001>.
- [Taylor63] B. N. Taylor and E. Burstein. *Excess currents in electron tunneling between superconductors*. Physical Review Letters 10(1), pp. 14, 1963. <https://dx.doi.org/10.1103/physrevlett.10.14>.
- [Tedrow71] P. M. Tedrow and R. Meservey. *Spin-dependent tunneling into ferromagnetic nickel*. Physical Review Letters 26(4), pp. 192, 1971. <https://dx.doi.org/10.1103/physrevlett.26.192>.
- [Ternes06] Markus Ternes, Wolf-Dieter Schneider, Juan-Carlos Cuevas, Christopher P. Lutz, Cyrus F. Hirjibehedin and Andreas J. Heinrich. *Subgap*



- structure in asymmetric superconducting tunnel junctions*. Phys. Rev. B 74(13), 2006. <https://dx.doi.org/10.1103/physrevb.74.132501>.
- [Tersoff83] J. Tersoff and D. R. Hamann. *Theory and application for the scanning tunneling microscope*. Physical Review Letters 50(25), pp. 1998, 1983. <https://dx.doi.org/10.1103/physrevlett.50.1998>.
- [Tersoff85] J. Tersoff and D. R. Hamann. *Theory of the scanning tunneling microscope*. Physical Review B 31(2), pp. 805, 1985. <https://dx.doi.org/10.1103/physrevb.31.805>.
- [Tinkham04] Michael Tinkham. *Introduction to Superconductivity: Second Edition (Dover Books on Physics) (Vol i)*. Dover Publications, 2004. ISBN 978-0-486-43503-9.
- [Toll56] John S. Toll. *Causality and the dispersion relation: Logical foundations*. Physical Review 104(6), pp. 1760, 1956. <https://dx.doi.org/10.1103/physrev.104.1760>.
- [Ugeda15] Miguel M. Ugeda, Aaron J. Bradley, Yi Zhang, Seita Onishi, Yi Chen, Wei Ruan, Claudia Ojeda-Aristizabal, Hyejin Ryu, Mark T. Edmonds, Hsin-Zon Tsai, Alexander Riss, Sung-Kwan Mo, Dunghai Lee, Alex Zettl, Zahid Hussain, Zhi-Xun Shen and Michael F. Crommie. *Characterization of collective ground states in single-layer NbSe<sub>2</sub>*. Nature Physics 12(1), pp. 92, 2015. <https://dx.doi.org/10.1038/nphys3527>.
- [van Wees88] B. J. van Wees, H. van Houten, C. W. J. Beenakker, J. G. Williamson, L. P. Kouwenhoven, D. van der Marel and C. T. Foxon. *Quantized conductance of point contacts in a two-dimensional electron gas*. Physical Review Letters 60(9), pp. 848, 1988. <https://dx.doi.org/10.1103/physrevlett.60.848>.
- [Vardimon13] Ran Vardimon, Marina Klionsky and Oren Tal. *Experimental determination of conduction channels in atomic-scale conductors based on shot noise measurements*. Phys. Rev. B 88(16), 2013. <https://dx.doi.org/10.1103/physrevb.88.161404>.
- [Wang17] Hong Wang, Xiangwei Huang, Junhao Lin, Jian Cui, Yu Chen, Chao Zhu, Fucai Liu, Qingsheng Zeng, Jiadong Zhou, Peng Yu, Xuewen Wang, Haiyong He, Siu Hon Tsang, Weibo Gao, Kazu Suenaga, Fengcai Ma, Changli Yang, Li Lu, Ting Yu, Edwin Hang Tong Teo, Guangtong Liu and Zheng Liu. *High-quality monolayer superconductor NbSe<sub>2</sub> grown by chemical vapour deposition*. Nature Communications 8(1), 2017. <https://dx.doi.org/10.1038/s41467-017-00427-5>.

## Bibliography

---

- [Wharam88] D A Wharam, T J Thornton, R Newbury, M Pepper, H Ahmed, J E F Frost, D G Hasko, D C Peacock, D A Ritchie and G A C Jones. *One-dimensional transport and the quantisation of the ballistic resistance*. Journal of Physics C: Solid State Physics 21(8), pp. L209, 1988. <https://dx.doi.org/10.1088/0022-3719/21/8/002>.
- [Worledge00] D. C. Worledge and T. H. Geballe. *Maki analysis of spin-polarized tunneling in an oxide ferromagnet*. Physical Review B 62(1), pp. 447, 2000. <https://dx.doi.org/10.1103/physrevb.62.447>.
- [Xi15] Xiaoxiang Xi, Zefang Wang, Weiwei Zhao, Ju-Hyun Park, Kam Tuen Law, Helmuth Berger, László Forró, Jie Shan and Kin Fai Mak. *Ising pairing in superconducting NbSe<sub>2</sub> atomic layers*. Nature Physics 12(2), pp. 139, 2015. <https://dx.doi.org/10.1038/nphys3538>.
- [Yazdani97] A. Yazdani. *Probing the local effects of magnetic impurities on superconductivity*. Science 275(5307), pp. 1767, 1997. <https://dx.doi.org/10.1126/science.275.5307.1767>.
- [Yokoya01] T. Yokoya, T. Kiss, A. Chainani, S. Shin, M. Nohara and H. Takagi. *Fermi surface sheet-dependent superconductivity in 2H-NbSe<sub>2</sub>*. Science 294(5551), pp. 2518, 2001. <https://dx.doi.org/10.1126/science.1065068>.
- [Yu65] Luh Yu. *Bound state in superconductors with paramagnetic impurities*. Acta Physica Sinica 21(1), 75, 1965. <https://dx.doi.org/10.7498/aps.21.75>.
- [Zarate85] H. G. Zarate and J. P. Carbotte. *On phonon structure in proximity tunnel junctions*. Journal of Low Temperature Physics 59(1-2), pp. 19, 1985. <https://dx.doi.org/10.1007/bf00681502>.
- [Zhao02] Guo meng Zhao. *Unconventional phonon-mediated superconductivity in MgB<sub>2</sub>*. New Journal of Physics 4, pp. 3, 2002. <https://dx.doi.org/10.1088/1367-2630/4/1/303>.

## Photographic credits

Figure 2.2 is taken from [Chaika14], where it was published under the Creative Commons license: CC BY-NC-SA 3.0, <https://creativecommons.org/licenses/by-nc-sa/3.0/>.

Figures 3.7, 3.8, 3.9, 3.10, 3.11 and 3.12 a) are from [Ast16]. Where they are published under the Creative Commons license: CC BY 4.0, <https://creativecommons.org/licenses/by/4.0/>. I am a coauthor of this publication.

Figures 4.1, 4.3 and 4.4 are from the PhD thesis of Juan Carlos Cuevas [Cuevas99] and were reproduced with slight modifications with personal permission.



# Curriculum Vitae

## Personal Information

Name	Jacob Senkpiel
Date of Birth	December 12, 1986
Place of Birth	Jever, Germany
Nationality	German

## Current Position

Since September 2014 working as a PhD student at the Nanoscale Science Department of the Max-Planck-Institute for Solid State Research in Stuttgart, enrolled in the doctoral program in physics at the École Polytechnique Fédérale de Lausanne (EPFL).

## Education

- 2014: Master of Science degree (**M. Sc.**) in Nanostructure Technology at the University of Würzburg.
  - Thesis about the Kondo effect and chirality of CuPc and MnPc on Ag(100) and Cu(100).
- 2012: Bachelor of Science degree (**B. Sc.**) in Nanostructure Technology at the University of Würzburg.
  - Thesis in the area of electrically driven polariton lasing in GaAs quantum film diodes.

## Scientific Work Experience

- 2 years accompanying my Master studies, as a research assistant at the Fraunhofer Institute for Silicate Research (ISC), in the field of electrochemistry.

## **Bibliography**

---

- 6 weeks during my Bachelor studies, as an intern in the department of Analytics and Metrology at OSRAM Opto Semiconductors GmbH, Regensburg.

# Publications

- *Single Channel Josephson Effect in an Ultrasmall High Transmission Atomic Contact*, Jacob Senkpiel, Simon Dambach, Markus Etzkorn, Robert Drost, Björn Kubala, Wolfgang Belzig, Alfredo Levy Yeyati, Juan Carlos Cuevas, Joachim Ankerhold, Christian R. Ast and Klaus Kern, in preparation.
- *Jahn-Teller Splitting in Single Adsorbed Molecules Revealed by Isospin-Flip Excitations*, Jens Kügel, Pin-Jui Hsu, Markus Böhme, Kathrin Schneider, Jacob Senkpiel, David Serrate, Matthias Bode and Nicolás Lorente, submitted.
- *Robustness of Yu-Shiba-Rusinov resonances in presence of a complex superconducting order parameter*, Jacob Senkpiel, Carmen Rubio-Verdú, Markus Etzkorn, Robert Drost, Leslie M. Schoop, Simon Dambach, Ciprian Padurariu, Björn Kubala, Joachim Ankerhold, Christian R. Ast and Klaus Kern, arXiv:1803.08726 [cond-mat.supr-con].
- *Signatures of phase-coherent transport and the role of quantum fluctuations in the dynamical Coulomb blockade regime*, Berthold Jäck, Jacob Senkpiel, Markus Etzkorn, Joachim Ankerhold, Christian R. Ast and Klaus Kern, arXiv:1712.07172 [cond-mat.mes-hall].
- *Quantum Brownian Motion at Strong Dissipation Probed by Superconducting Tunnel Junctions*, Berthold Jäck, Jacob Senkpiel, Markus Etzkorn, Joachim Ankerhold, Christian R. Ast and Klaus Kern, Phys. Rev. Lett. **119**, 147702, 2017.
- *Sensing the quantum limit in scanning tunnelling spectroscopy*, Christian R. Ast, Berthold Jäck, Jacob Senkpiel, Matthias Eltschka, Markus Etzkorn, Joachim Ankerhold and Klaus Kern, Nat. Commun. **7**, 13009, 2016.
- *State identification and tunable Kondo effect of MnPc on Ag(001)*, Jens Kügel, Michael Karolak, Andreas Krönlein, Jacob Senkpiel, Pin-Jui Hsu, Giorgio Sangiovanni and Matthias Bode, Phys. Rev. B **91**, 235130, 2015.
- *Relevance of Hybridization and Filling of 3d Orbitals for the Kondo Effect in Transition Metal Phthalocyanines*, Jens Kügel, Michael Karolak, Jacob Senkpiel, Pin-Jui Hsu, Giorgio Sangiovanni and Matthias Bode, Nano Lett., **14** (7), 3895–3902, 2014.